MANTLE PLUME-MIDOCEAN RIDGE INTERACTION: GEOPHYSICAL OBSERVATIONS AND MANTLE DYNAMICS

by

GARRETT TETSUO ITO

SUBMITTED IN PARTIAL FULFILLMENT OF THE REQUIREMENTS FOR THE DEGREE OF
DOCTOR OF PHILOSOPHY
at the
WOODS HOLE OCEANOGRAPHIC INSTITUTION
and the
THE MASSACHUSETTS INSTITUTION OF TECHNOLOGY
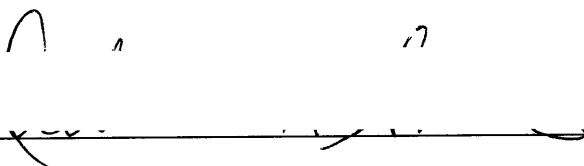
September 1996

Signature of Author _____

Joint Program in Oceanography,
Massachusetts Institute of Technology and
Woods Hole Oceanographic Institution

Certified by _____

Jian Lin, Thesis Supervisor

Accepted by _____

Deborah K. Smith, Chair
Joint Committee for Marine Geology and Geophysics,
Massachusetts Institute of Technology/Woods Hole Oceanographic Institution

MANTLE PLUME-MID-OCEAN RIDGE INTERACTION: GEOPHYSICAL OBSERVATIONS AND MANTLE DYNAMICS

by

Garrett Tetsuo Ito

Submitted to the Department of Earth, Atmospheric, and Planetary Sciences
Massachusetts Institute of Technology
and
the Department of Geology and Geophysics
Woods Hole Oceanographic Institution
on August 9, 1996
in partial fulfillment of the requirements for the degree Doctor of Philosophy

ABSTRACT

We analyze bathymetric and gravity anomalies at five plume-ridge systems to constrain crustal and mantle density structure at these prominent oceanic features. Numerical models are then used to explore the physical mechanisms controlling plume-ridge interaction and to place theoretical constraints on the temperature anomalies, dimensions, and fluxes of the Icelandic and Galápagos plumes.

In Chapter 1 we analyze bathymetric and gravity anomalies along the hotspot-influenced Galápagos Spreading Center. We find that the Galápagos plume generates along-axis bathymetric and mantle-Bouguer gravity anomalies (MBA) that extend >500 km east and west of the Galápagos Islands. The along-axis MBA becomes increasingly negative towards the plume center, reaching a minimum of ~-90 mGal near 91°W, and axial topography shallows by ~1.1 km toward the plume. These variations in MBA and bathymetry are attributed to the combined effects of crustal thickening and anomalously low mantle densities, both of which are due to a mantle temperature anomaly imposed beneath the ridge by the Galápagos plume. Passive mantle flow models predict a temperature anomaly of 50±25°C is sufficient to produce the 2-4 km excess crust required to explain the along-axis anomalies. 70-75% of the along-axis bathymetric and MBA variations are estimated to arise from the crust with the remaining 25-30% generated by the anomalously hot, thus low-density mantle. Along Cocos-plate isochrons, bathymetric and MBA variations increase with increasing isochron age, suggesting the subaxial mantle temperature anomaly was greater in the past when the plume was closer to the ridge axis.

In addition to the Galápagos plume-ridge system, in Chapter 2 we examine along-isochron bathymetric and MBA variations at four other plume-ridge systems associated with the Iceland, Azores, Easter and Tristan hotspots. We show that residual bathymetry (up to 4.7 km) and mantle-Bouguer gravity anomalies (up to -340 mGal) are greatest at on-axis plumes and decreases with increasing ridge-hotspot separation distance, until becoming insignificant at a plume-ridge separation of ~500 km. Along-isochron widths of bathymetric anomalies (up to 2700 km) decrease with increasing paleo-spreading rate, reflecting the extent to which plume material flows along-axis before being swept away by the spreading lithosphere. Scaling arguments suggest an average ridgeward plume flux of ~2.2x10^6 km/my. Assuming that the amplitudes of the MBA and bathymetric anomalies reflect crustal thickness and mantle density variations, passive mantle flow models predict

maximum subaxial mantle temperature anomalies to be 150-225°C for ridge-center plumes, which decrease as the ridges migrate away from the plumes.

The dynamics of mantle flow and melting at ridge-centered plumes are investigated in Chapters 3 using three-dimensional, variable-viscosity, numerical models. Three buoyancy sources are examined: temperature, melt depletion, and melt retention. The width W to which a plume spreads along a ridge axis depends on plume volume flux Q, full spreading rate U, buoyancy number $B = (Q\Delta\rho g)/(48\eta_o U^2)$, and ambient/plume viscosity contrast γ according to $W=2.37(Q/U)^{1/2}(B\gamma)^{0.04}$. Thermal buoyancy is first order in controlling along-axis plume spreading while latent heat loss due to melting, and depletion and retention buoyancy forces contribute second order effects. Two end-member models of the Iceland-Mid-Atlantic Ridge (MAR) system are examined. The first end-member model has a broad plume source of radius 300 km, temperature anomaly of 75°C, and volume flux of 1.2×10^7 km^3/my. The second model has a narrower plume source of radius 60 km, temperature anomaly of 170°C, and flux of 2.1×10^6 km^3/my. The first model predicts successfully the observed crustal thickness, topographic, and MBA variations along the MAR, but the second model requires substantial along-axis melt transport in order to explain the observed along-axis variations in crustal thickness, bathymetry, and gravity. We favor this second model because it predicts a mantle P-wave velocity reduction in the plume of ~2% as consistent with recent seismic observations beneath Iceland.

Finally in Chapter 4 we use three-dimensional numerical models to investigate the interaction of plumes and migrating midocean ridges. Scaling laws of axial plume spreading width W are derived first for stationary ridges and off-axis plumes, which yield results consistent with those obtained from independent studies of *Ribe* [1996]. W and the maximum plume-ridge interaction distance x_{max} again scale with $(Q/U)^{1/2}$ as in the case of ridge-centered plumes and increase with γ and buoyancy number. In the case of a migrating ridge, x_{max} is reduced when a ridge migrates toward the plume due to excess drag of the faster-moving leading plate, and enhanced when a ridge migrates away from the plume due to reduced drag of the slower-moving trailing plate. Thermal erosion of the lithospheric boundary layer by the previously ridge-centered plume further enhances W and x_{max} but to a degree that is secondary to the differential migration rates of the two plates. Model predictions are compared with observed along-isochron bathymetric and MBA variations at the Galápagos plume-ridge system. The anomaly amplitudes and widths, as well as the increase in anomaly amplitude with age are predicted with a plume source temperature anomaly of 80-120°C, radius of 80-100 km, and volume flux of 4.5×10^6 km^3/m.y. Our numerical models also predict crustal production rates of the Galápagos Islands consistent with those estimated independently using the observed island topography. Predictions of the geochemical signature of the plume along the present-day ridge suggest that mixing between the plume and ambient mantle sources is unlikely to occur in the asthenosphere or shallow crust, but most likely deeper in the mantle possibly by entrainment of ambient mantle as the plume ascends through the depleted portion of the mantle from its deep source reservoir.

Thesis Supervisor: Dr. Jian Lin
Department of Geology and Geophysics
Wood Hole Oceanographic Institution

4

With love to my parents,
Janice and Floyd Ito
for giving so much

TABLE OF CONTENTS

INTRODUCTION

Hotspots and midocean ridges are the sources of the ocean's igneous crust and are thus the primary mechanisms by which heat and mass are transported from the mantle to the Earth's surface. The present-day global oceanic crustal production rate of 2 x 10^7 km^3/my, of which ~10% is due to hotspot volcanism [*Larson* , 1991] is sufficient to resurface the planet with a 7 km-thick crust every 175 m.y. years. Moreover, crustal production rates may have been greater by a factor of 2 in the geologically recent past [*Larson*, 1991]. Thus, studies of igneous and mantle dynamic processes at hotspots and midocean ridges are crucial to our understanding of Earth structure at present-day and in the past.

Over the past three decades much has been learned about the dynamics of mantle flow and melt generation at hotspots and midocean ridges. Since *Hess*'s [1962] hypothesis that midocean ridges are the ascending limbs of mantle convection cells, a number of observational and theoretical studies have shaped our present conceptions of midocean ridge dynamics. For example, *Hess*'s [1962] convection hypothesis was examined quantitatively by means of a boundary layer treatment of cell convection in two-dimensions (2-D) [*Oxburgh and Turcotte*, 1967; *Turcotte and Oxburgh*, 1967]. The study by *Oxburgh and Turcotte* [1967] was among the first to establish the concept of a lithospheric thermal boundary layer, to explain the decrease in seafloor heat flow with age, and to discuss decompression melting processes at midocean ridges. A parallel study by *McKenzie* [1967] was among the first to explain seafloor heat flow variations by a conductively cooling plate model overlying an asthenosphere of uniform temperature.

Furthermore, the finding that normal oceanic crust was ~6 km in thickness, globally [*Raitt*, 1963] , provides a powerful constraint on mantle flow and thermal structure beneath midocean ridges. *Reid and Jackson* [1981] demonstrated that simple 2-D corner flow models could produce the mantle temperatures and upwelling rates necessary to generate a 6-km thick crust at intermediate and fast spreading rates. Thermal and compositional buoyancy, however, seemed to be required to generate 6 km of crust at slow spreading rates [e.g. *Buck and Su*, 1989; *Rabinowicz*, 1987; *Scott and Stevenson*, 1989; *Sotin and Parmentier*, 1989]. Further work such as that of *Bottinga and Allégre* [1978], *Klein and Langmuir* [1987], *McKenzie* [1984], and *McKenzie and Bickle*, [1988] were groundwork studies of the thermal dynamics of mantle melting at ridges and on the composition of ocean ridge basalts.

During the time that seafloor spreading was being recognized as the surface expression of a convecting Earth, hotspots were also being attributed to mantle processes, separate from, but consistent with, the plate tectonic paradigm. *Wilson* [1963] introduced the concept that the age progression along the Hawaiian Island chain reflects migration of the lithospheric plate over a magma source which is fixed in the mantle. Such findings led to Morgan's hypothesis that hotspots are the result of mantle convection plumes which ascend from the deep mantle to the base of the lithosphere [*Morgan*, 1971; *Morgan*, 1972]. Follow-up theoretical studies by *Parmentier et al.* [1975] and laboratory experiments of *Whitehead and Luther* [1975] demonstrated that Rayleigh-Taylor instabilities from a basally heated mantle could generate localized upwelling in the form of plumes. Along with the plume hypothesis came studies by *Crough* [1978, 1983], who attributed the broad (1000-2000 km) hotspot swells to anomalously hot, low-density lithosphere, and work by *Detrick and Crough* [1978], which introduced the concept of plume-induced lithospheric thinning. Later work by Olson and colleagues showed that hotspot swells could be explained by the dynamic uplift of a plume as it spreads gravitationally beneath the lithosphere [*Olson* 1990; *Olson and Nam*, 1986; *Olson et al.*, 1988]. Finally, *Watson and McKenzie* [1991] combined the physics of a buoyantly upwelling plume with melting models of *McKenzie and Bickle* [1988] to examine melting processes beneath the Hawaiian hotspot.

A landmark discovery by Schilling and co-workers demonstrated that igneous products at hotspots such as Hawaii, Iceland, Galápagos, and the Azores have rare-earth element compositions distinct from typical midocean ridge basalts (MORB) [*Schilling,* 1971, 1973, 1975, *Schilling et al.,* 1976; *Schilling and Winchester*, 1967]. Moreover, their findings of hotspot-type chemical signatures in basalts at hotspot-like swells along midocean ridges, such as Iceland on the Mid-Atlantic Ridge, led to the concept that rising mantle plumes interact with and feed oceanic spreading centers [*Hart et al.*, 1973; *Schilling*, 1971, 1973, 1975; *Schilling and Winchester*, 1967; *Sun et al.*, 1975]. Independent studies of plate kinematics led to *Morgan* [1978]'s idea of a "second type of hotspot island" which also suggested that plumes spread horizontally to nearby oceanic spreading centers; while *Vogt* [1971, 1972, 1976] showed evidence that plumes inject material also along the axes of midocean ridges. These original studies stimulated numerous geophysical and geochemical surveys of plume-ridge systems leading to papers by Schilling and co-workers which have shaped concepts today of how mantle plumes may interact with midocean ridges [e.g. *Schilling,* 1985, 1991; *Schilling et al.*, 1985] .

With the conceptual frameworks of midocean ridges, plumes, and the interaction of plumes and ridges established, the purpose of this thesis is to examine quantitatively the mantle and crustal structure of plume-ridge systems and the causal mantle dynamic and igneous processes. The first two chapters focus on using bathymetric and gravity observations to infer crustal and mantle density structure at the Galápagos (Chapter 1), Iceland, Azores, Tristan, and Easter (Chapter 2) plume-ridge systems. The last two chapters focus on the dynamics of mantle flow and melting at plume-ridge systems, which are investigated with numerical models as constrained by the geophysical observations.

In Chapter 1, we investigate the crustal thickness and mantle temperature variations along the Galápagos Spreading Center imposed by the Galápagos plume. The mantle-Bouguer gravity anomaly (MBA)—which is the free-airy gravity anomaly corrected for the attraction of seafloor topography and the crust-mantle interface assuming a reference crust of uniform density and thickness—has been particularly useful in understanding subsurface density structure at midocean ridges. For example, bulls-eye shaped MBA lows centered on individual ridge segments as documented by *Kuo and Forsyth* [1988] and *Lin et al.* [1990] are strong evidence that crustal accretion at slow-spreading ridges varies significantly along-axis and that this accretion may occur due to convective upwelling as hypothesized by *Whitehead et al.* [1984]. In Chapter 1 we produce maps of MBA anomaly and bathymetry, both of which reflect variations in crustal thickness and mantle density at the Galápagos ridge due to the excess temperature imposed by the Galápagos hotspot.

Temperature anomalies and the structure of mantle plumes at intraplate hotspots are reflected directly in the shape and amplitude of hotspot swells [e.g. *McNutt*, 1987; *Sleep* 1987, 1990]. At near-ridge hotspots such as the Galápagos, however, the mantle temperature anomaly at the ridge-axis is likely to enhance crustal production; consequently, investigations of mantle temperature anomalies at near-ridge hotspots requires the consideration of melting. We therefore use 3-D passive flow models—analogous to the corner flow description of *Reid and Jackson* [1981]—of the Galápagos Spreading Center to predict thickness variations along the ridge axis due to a range of axial temperature anomalies. The combined contributions of crustal thickness and mantle density variations to bathymetry and MBA are then compared with observations to constrain mantle temperature. Similar analyses are done for anomalies along Cocos-Plate isochrons to infer crustal thickness variations and associated mantle temperature anomalies in the past when the Galápagos Spreading Center was closer to the Galápagos plume.

Analyses of bathymetric and MBA variations along isochrons is a unique method of investigating the evolution of individual plume-ridge systems. In Chapter 2 we investigate along-axis and along-isochron anomalies at five prominent systems associated with the Galápagos, Azores, Iceland, Tristan, and Easter hotspots. In addition we use independent constraints on past plate motions to estimate plume-ridge separation distances and spreading rates at times corresponding to the isochron ages. We investigate relationships between bathymetric and MBA amplitudes and paleo-plume-ridge distance, as well as between widths of along-isochron bathymetric anomalies and paleo-spreading rate. Scaling laws are then derived for the dependence of anomaly amplitudes and mantle temperature anomalies to examine how axial temperature anomalies of the five systems may have changed with plume-ridge distance.

While the passive flow models used in Chapters 1 and 2 are reasonable approximations of the flow beneath oceanic spreading centers, they are poor representations of the flow structure at buoyantly upwelling plumes. To investigate the dynamics of mantle flow and melting at plume-ridge systems it is therefore necessary to incorporate both the flow beneath a spreading center system as first investigated by Turcotte and Oxburgh, as well as the pertinent physics of plume convection as originally identified by *Parmentier et al.*, [1975] and *Whitehead and Luther*, [1975] . Thus, in Chapter 3 we used numerical models to simulate the 3-D interaction between ridge-centered buoyant plumes and oceanic spreading centers. We consider fully pressure- and temperature-dependent rheology and investigate buoyancy due to thermal expansion, melt depletion, and melt retention. First, scaling laws are derived for the dependence of along-axis plume width on plume flux, ridge spreading rate, and ambient/plume viscosity contrast in the absence of melting. We then investigate the melting effects of latent heat loss, and depletion and retention buoyancy on flow structure and on the scaling laws. Finally, we apply our models to the Iceland-Mid-Atlantic Ridge system. Model predictions and observations of along-axis crustal thickness, bathymetry, MBA, and geochemical variations are compared for two plume source radii and temperature anomalies which represent end-member properties of the Icelandic plume source.

The purpose of the last chapter is to investigate the fluid dynamics of plume-migrating ridge interaction. An important aspect is to test quantitatively the "mantle plume source/migrating ridge sink" hypothesis originally proposed by Schilling and co-workers as based on their geochemical findings as well as the work of Morgan and Vogt. Scaling laws are first derived for off-axis plumes in steady state with stationary midocean ridges

and are compared with independent but parallel studies of Ribe [1996]. For migrating ridge cases, we then investigate how along-axis plume width and maximum plume-ridge interaction distance scale with ridge migration rate, spreading rate, plume flux, and ambient/plume viscosity. The model is then tested by comparing model predictions with bathymetric and MBA observations of the Galápagos plume-migrating ridge system. Anomalies are compared at the present-day ridge axis as well as at the Cocos Plate isochrons examined in Chapter 1. We also compare predictions and observations of the geochemical signature of the Galápagos plume along the Galápagos Spreading Center in order to investigate the processes of mixing between the plume and ambient mantle sources.

Finally I include in the Appendix, laboratory tank experiments done with C. Kincaid and C. Gable on off-axis plume-ridge interaction. A plume and ridge upper mantle system is simulated with a tank of concentrated sucrose solution in order to investigate the primary mechanisms that allow an off-axis plume to overcome the viscous drag of a spreading plate to feed the nearby ridge.

References

Bottinga, Y., and C. J. Allégre, Partial melting under spreading ridges, *Phil. Trans. R. Soc. Lond. A.*, *288*, 501-525, 1978.

Buck, W. R., and W. Su, Focused mantle upwelling below mid-ocean ridges due to feedback between viscosity and melting, *Geophys. Res. Lett.*, *16*, 641-644, 1989.

Crough, S. T., Thermal origin of mid-plate hot-spot swells, *Geophys. J. R. astr. Soc.*, *55*, 451-469, 1978.

Crough, S. T., Hotspot swells, *Annual Reviews of Earth and Planetary Science*, *11*, 165-193, 1983.

Detrick, R. S., and S. T. Crough, Island subsidence, hot spots, and lithospheric thinning, *J. Geophys. Res.*, *83*, 1236-1244, 1978.

Hart, S. R., J.-G. Schilling, and J. L. Powell, Basalts from Iceland and along the Reykjanes Ridge: Sr isotope geochemistry, *Nature Physical Science*, *246*, 104-107, 1973.

Hess, H. H., History of ocean basins, *Petrologic Studies*, vol. ed. pp. 599, Geological Society of America, New York, 1962.

Hess, H. H., Mid-oceanic ridges and tectonics of the sea floor, *Submarine Geology and Geophysics, Colston Papers 17*, vol. ed. pp. 317, Butterworths, London, 1965.

Klein, E. M., and C. H. Langmuir, Global correlations of ocean ridge basalt chemistry with axial depth and crustal thickness, *J. Geophys. Res.*, *92*, 8089-8115, 1987.

Kuo, B.-Y., and D. W. Forsyth, Gravity anomalies of the ridge-transform system in the South Atlantic between 31° and 34.5°S: Upwelling centers and variations in crustal thickness, *Mar. Geophys. Res.*, *10*, 205-232, 1988.

Larson, R. L., Latest pulse of Earth: Evidence for a mid-Cretaceous superplume, *Geology*, *19*, 547-550, 1991.

Lin, J., G. M. Purdy, H. Schouten, J.-C. Sempéré, and C. Zervas, Evidence from gravity data for focused magmatic accretion along the Mid-Atlantic Ridge, *Nature*, *344*, 627-632, 1990.

McKenzie, D., Some remarks on heat flow and gravity anomalies, *J. Geophys. Res.*, *72*, 6261-6263, 1967.

McKenzie, D., The generation and compaction of partially molten rock, *J. Petrol.*, *25*, 713-765, 1984.

McKenzie, D., and M. J. Bickle, The volume and composition of melt generated by extension of the lithosphere, *J. Petrol.*, *29*, 625-679, 1988.

McNutt, M., Temperature beneath midplate swells: The inverse problem, *Seamounts, Islands, and Atolls*, *Geophysical Monograph Series*, vol. 43, ed. B. Keating, P. Fryer, R. Batiza and G. W. Boehlert, pp. AGU, Washington, D. C., 1987.

Morgan, W. J., Convection plumes in the lower mantle, *Nature*, *230*, 42-43, 1971.

Morgan, W. J., Plate motions and deep mantle convection, *The geological society of America memoir*, *132*, 7-22, 1972.

Morgan, W. J., Rodriguez, Darwin, Amsterdam,..., A second type of hotspot island, *J. Geophys. Res.*, *83*, 5355-5360, 1978.

Olson, P., Hot spots, swells and mantle plumes, *Magma transport and storage*, vol. ed. M. P. Ryan, pp. 33-51, John Wiley and Sons Ltd, 1990.

Olson, P., and I. S. Nam, Formation of seafloor swells by mantle plumes, *J. Geophys. Res.*, *91*, 7181-7191, 1986.

Olson, P., G. Schubert, C. Anderson, and P. Goldman, Plume formation and lithosphere erosion: A comparison of laboratory and numerical experiments, *J. Geophys. Res.*, *93*, 15,065-15,084, 1988.

Oxburgh, E. R., and D. L. Turcotte, Mid-ocean ridges and geotherm distribution during mantle convection, *J. Geophys. Res.*, *73*, 2643-2661, 1967.

Parmentier, E. M., D. L. Turcotte, and K. E. Torrance, Numerical experiments on the structure of mantle plumes, *J. Geophys. Res.*, *80*, 4417-4424, 1975.

Rabinowicz, M., Melt segregation and flow in mantle diapirs below spreading centers: Evidence from the Oman ophiolite, *J. Geophys. Res.*, *92*, 3475-3486, 1987.

Raitt, R. W., The crustal rocks, *The Sea*, vol. 3, ed. M.N. Hill, pp. 85-102, Interscience Publishers, New York, 1963.

Reid, I., and H. R. Jackson, Oceanic spreading rate and crustal thickness, *Mar. Geophys. Res.*, *5*, 165-172, 1981.

Ribe, N., The dynamics of plume-ridge interaction 2. Off-ridge plumes, *J. Geophys. Res.*, *101*, 16,195-16,204, 1996.

Schilling, J.-G., Sea floor evolution: rare earth evidence, *Phil. Trans. Roy. Soc. London*, *268A*, 663-706, 1971.

Schilling, J.-G., Iceland mantle plume: Geochemical study of Reykjanes Ridge, *Nature*, *242*, 565-571, 1973.

Schilling, J.-G., Azores mantle blob: Rare-earth evidence, *Earth Planet. Sci. Lett.*, *25*, 103-115, 1975.

Schilling, J.-G., Upper mantle heterogeneities and dynamics, *Nature*, *314*, 62-67, 1985.

Schilling, J.-G., Fluxes and excess temperatures of mantle plumes inferred from their interaction with migrating mid-ocean ridges, *Nature*, *352*, 397-403, 1991.

Schilling, J.-G., R. N. Anderson, and P. Vogt, Rare earth, Fe and Ti variations along the Galapagos spreading centre, and their relationship to the Galapagos mantle plume, *Nature*, *261*, 108-113, 1976.

Schilling, J.-G., G. Thompson, R. Kingsley, and S. Humphris, Hotspot-migrating ridge interaction in the South Atlantic, *Nature*, *313*, 187-191, 1985.

Schilling, J.-G., and J. W. Winchester, Rare Earth fractionation and magmatic processes, *Mantles of the Earth and terrestrial planets*, vol. ed. S. K. Runcorn, pp. Interscience Publishers, London, 1967.

Scott, D. R., and D. J. Stevenson, A self-consistent model for melting, magma migration and buoyancy-driven circulation beneath mid-ocean ridges, *J. Geophys. Res.*, *94*, 2973-2988, 1989.

Sleep, N. H., An analytic model for a mantle plume fed by a boundary layer, *Geophys. J. R. astr. Soc.*, *90*, 119-128, 1987.

Sleep, N. H., Hotspots and mantle plumes: Some phenomenology, *J. Geophys. Res.*, *95*, 6715-6736, 1990.

Sotin, C., and E. M. Parmentier, Dynamical consequences of compositional and thermal density stratification beneath spreading centers, *Geophys. Res. Lett.*, *16*, 835-838, 1989.

Sun, S.-S., M. Tatsumoto, and J.-G. Schilling, Mantle plume mixing along the Reykjanes Ridge axis: Lead isotopic evidence, *Science*, *190*, 143-147, 1975.

Turcotte, D. L., and E. R. Oxburgh, Finite amplitude convective cells and continental drift, *J. Fluid Mech.*, *28*, 29, 1967.

Vogt, P. R., Asthenosphere motion recorded by the by the ocean floor south of Iceland, *Earth Planet. Sci. Lett.*, *13*, 153-160, 1971.

Vogt, P. R., Evidence for global synchronism in mantle plume convection, and possible significance for geology, *Nature*, *240*, 338-342, 1972.

Vogt, P. R., Plumes, subaxial pipe flow, and topography along the mid-ocean ridge, *Earth Planet. Sci. Lett.*, *29*, 309-325, 1976.

Watson, S., and D. McKenzie, Melt generation by plumes: A study of Hawaiian volcanism, *J. Petrol.*, *32*, 501-537, 1991.

Whitehead, J. A., H. J. B. Dick, and H. Schouten, A mechanism for magmatic accretion under spreading centers, *Nature*, *312*, 146-148, 1984.

Whitehead, J. A., and D. S. Luther, Dynamics of laboratory diapir and plume models, *J. Geophys. Res.*, *80*, 705-717, 1975.

Wilson, J. T., A possible origin of the Hawaiin Islands, *Canadian Journal of Physics*, *41*, 863, 1963.

CHAPTER 1

MANTLE TEMPERATURE ANOMALIES ALONG THE PRESENT AND
PALEOAXES OF THE GALAPAGOS SPREADING CENTER AS INFERRED FROM
GRAVITY ANALYSES

Mantle temperature anomalies along the present and paleoaxes of the Galápagos spreading center as inferred from gravity analyses

Garrett T. Ito[1] and Jian Lin

Department of Geology and Geophysics, Woods Hole Oceanographic Institution, Woods Hole, Massachusetts

Abstract. To better understand the effects of hot spots on mid-ocean ridge thermal structure, we investigate the subsurface density structure of the Galápagos spreading center and nearby lithosphere. Using shipboard gravity and bathymetry data, we obtain maps of mantle Bouguer anomalies (MBA) by removing from the free-air gravity the attractions of seafloor topography and a 6-km-thick model crust. Comparison of observed and theoretical MBA profiles along isochrons for ages 0.0-7.7 Ma suggests that seafloor topography is isostatically compensated by mass anomalies primarily in the upper 100 km of the mantle. This result is consistent with the notion that seafloor topography along the Galápagos spreading center is supported by lateral changes of crustal thickness and upper mantle density, both of which are controlled by temperatures in the upper mantle where decompression melting occurs. Along the ridge axis, the MBA decreases from the east and west toward the Galápagos hot spot by ~90 mGal, reaching a minimum nearest the hot spot at 91°W. Seafloor topography mirrors the MBA along axis, increasing by ~1.1 km toward the hot spot. These variations in MBA and bathymetry can be explained by crustal thickening and mantle density variations resulting from a gradual axial temperature increase of 50±25°C toward the hot spot. The predicted crustal thickening of 2-4 km nearest the hot spot accounts for 70-75% of the along-axis MBA and bathymetry anomalies; mantle density variations account for the rest of the anomalies. From the crustal isochron of age 7.7 Ma to the present-day axis, the along-isochron amplitudes of MBA decrease from ~150 to ~90 mGal. The corresponding along-isochron bathymetry anomalies decrease from ~1.7 to ~1.1 km. These observations along the paleoaxes of the Galápagos spreading center indicate that the axial temperature anomaly was 70% hotter in the past (86±25°C) and has steadily decreased to 50±25°C as the ridge axis migrated away from the Galápagos hot spot. These along-isochron temperature anomalies, however, have remained well below that estimated for the hot spot itself (200°C), indicating that the lateral temperature gradient between the hot spot and the ridge axis has remained 10-20 times greater than that along the ridge axis over the past 7.7 m.y.

Introduction

Three-dimensional gravity studies of mid-ocean spreading centers have proven crucial to understanding the processes controlling oceanic lithosphere accretion. For example, it has been shown that gravity and seafloor depth vary systematically along individual spreading segments [e.g., *Kuo and Forsyth*, 1988; *Prince and Forsyth*, 1988; *Lin et al.*, 1990; *Detrick et al.*, 1995] and appear to be spreading-rate-dependent [*Parmentier and Phipps Morgan*, 1990; *Lin and Phipps Morgan*, 1992; *Sparks et al.*, 1993]. Such variations in gravity and bathymetry indicate segment-scale changes in crustal thickness and/or mantle density and thus may reflect anomalies in along-axis mantle temperatures. Near hot spots, however, the extent of along-axis variation in density structure is broader than individual ridge segments, indicating a larger scale influence by mantle plumes

[*Anderson et al.*, 1973; *Cochran and Talwani*, 1977; *Bell and Buck*, 1992]. The influence of mantle plumes on crustal composition is also evident by enrichments of trace elements and isotopes along the Reykjanes Ridge near the Iceland hot spot [*Hart et al.*, 1973; *Schilling*, 1973, 1975a; *Vink*, 1984], along the Mid-Atlantic Ridge near the Azores hot spot [*White et al.*, 1975, 1976; *Schilling*, 1975b], and along the Galápagos spreading center near the Galápagos hot spot [*Schilling et al.*, 1976, 1982; *Verma and Schilling*, 1982; *Verma et al.*, 1983].

The Galápagos spreading center is an excellent example of an oceanic ridge influenced by a nearby hot spot. At present-day, the spreading center lies ~170 km north of the Galápagos hot spot and separates the Cocos Plate to the north and the Nazca Plate to the south with a full spreading rate of 4.5-6.8 cm/yr [*DeMets et al.*, 1990] (Plate 1a). Spreading segments of the Galápagos spreading center trend east-west and are adjoined by north-south trending transform faults. *Hey* [1977] proposed that the Galápagos hot spot began forming the Cocos and Carnegie Ridges ~20 Ma and then migrated southwest with respect to the Cocos Plate as it continued accreting the Cocos Ridge. The spreading center crossed over the hot spot 5-10 Ma as the Galápagos Archipelago began its formation on the Nazca Plate.

As for the present-day interaction between the hot spot plume and spreading center, it was first suggested by *Morgan* [1978]

---

[1] Also at MIT/WHOI Joint Program in Oceanography, Woods Hole Oceanographic Institution, Woods Hole.

a)

b)

c)
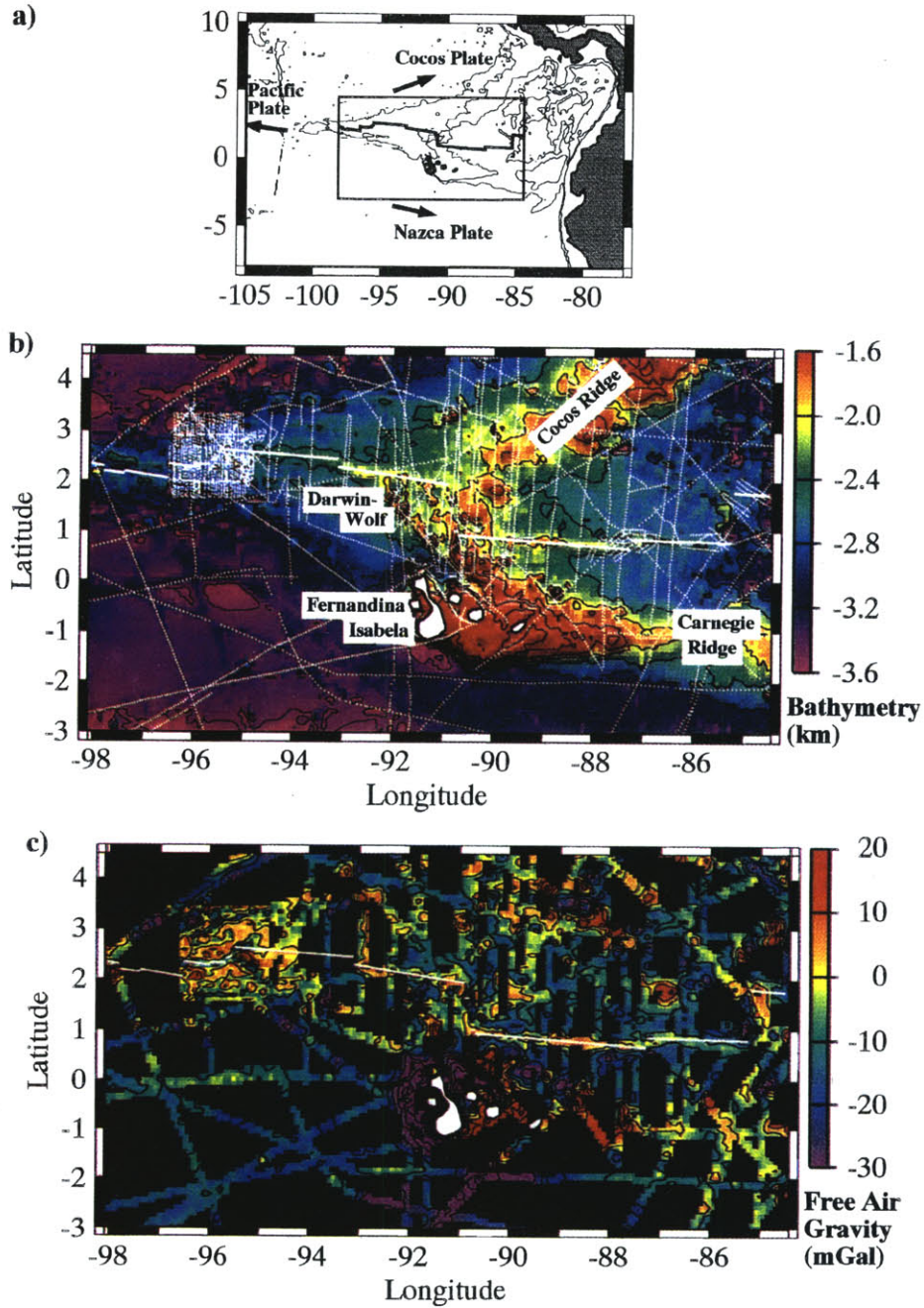
Plate 1. (a) Tectonic map of the Galápagos spreading system encompassing the study region (rectangular box). The solid dark lines mark the ridge axis, and the arrows show the estimated absolute plate motion relative to the hot spot reference frame. (b) Color-shaded map of shipboard and DBDB5 bathymetry illuminated from the north and contoured at 500-m intervals. Depths shallower than 1.6 km are colored red, while those deeper than 3.6 km are colored violet. Grid spacing is 5-min. The spreading center is marked by solid white lines and the gravity ship tracks are marked by white dotted lines. (c) Color map of free-air gravity along ship tracks with contour interval of 10 mGal and gridded with 5-min spacing. Gravity values >20 mGal are colored red, while those <-30 mGal are colored violet. The contours are drawn from interpolated values between ship tracks and are masked in regions with no data.

that Galápagos plume material feeds through a mantle conduit into the Galápagos spreading center giving rise to the Wolf-Darwin seamount chain (Plate 1b). Plume-fed mantle flow along axis was suggested by *Vogt* [1976] to explain the uniform increase in along-axis topography toward the hot spot. Further evidence for plume flow toward and along the spreading center is rare earth enrichments along the ridge, first documented by *Schilling et al.* [1976]. Subsequent studies of along-axis variation in rare earth element and isotopic ratios support ideas of plume entrainment to the ridge axis and along-axis dispersion of plume material [*Verma and Schilling*, 1982; *Verma et al.*, 1983; *Schilling*, 1985].

In this paper we present evidence for a regional mantle temperature anomaly and an associated crustal thickness variation beneath the Galápagos spreading center imposed by the Galápagos hot spot. We first isolate the subsurface component of the gravity field by making topographic and crust-mantle interface corrections (the mantle Bouguer corrections). We next examine topographic compensation mechanisms both on- and off-axis by comparing theoretical and observed mantle Bouguer gravity anomalies along isochrons for models of compensation from crustal thickness variations (Airy compensation) and compensation from laterally varying mantle densities (Pratt compensation). Given the constraints on the depth of compensation, we then examine models of crustal and mantle density structure to constrain mantle temperatures along the present-day Galápagos spreading center. Finally, we discuss the temporal evolution of axial mantle temperatures in the past 7.7 m.y. and its implications for the evolution of this hot spot-ridge system.

Data

Our approach for investigating mantle temperature anomalies requires accurate constraints on subsurface density structure which is reflected directly by gravity and seafloor topography. The gravity and bathymetry data we use are shipboard data obtained from the National Geophysical Data Center and the Lamont-Doherty Earth Observatory. The data set covers a region within 84.4°-98.1°W and 3.0°S-4.5°N, encompassing the Galápagos spreading center and the Galápagos hot spot (Plate 1b). We also use high-resolution gravity and bathymetry data from a dense survey around the 95.5°W propagating rift tip [*Phipps Morgan and Kleinrock*, 1991]. The bathymetry data are shipboard depth soundings supplemented with digital bathymetry (DBDB5) between ship tracks. DBDB5 data points within 5 min of a ship data point are eliminated and the combined data set is regridded with 5-min grid spacing to produce the bathymetry map shown in Plate 1b. A regional bathymetric swell encompassing the Galápagos Archipelago spans ~1300 km along the ridge axis. The swell shallows along the ridge axis toward 91°W by 1.1 km and peaks near the Galápagos hot spot which is centered beneath the island Fernandina [*White et al.*, 1993] (see Figure 1b for along-axis profile).

In order to improve the internal consistency of the gravity data we use the method of *Prince and Forsyth* [1984] to minimize discrepancies in gravity measurements at ship track crossings. Applying the appropriate DC shifts to straight-line track segments reduces the total rms crossover error from 11.2 to 5.5 mGal. The value of 5.5 mGal is therefore our estimate for data uncertainty. After applying these corrections we produce the 5-min grid of free-air gravity shown in Plate 1c. In this map we observe short-wavelength (<100 km) peaks coinciding with topographic highs; the lowest free-air gravity (-90 mGal) occurs over the flexural

moat of the Galápagos Archipelago and the highest (+60 mGal) occurs over the southeastern flank of the island of Isabela (see Plate 1b for location of Isabela). The total variation in free-air gravity along the ridge axis is ~40 mGal.

We use only shipboard gravity rather than satellite-altimetry-derived gravity because the released satellite data coverage in this region is still sparse and the shipboard gravity is more accurate. The other reason for using only shipboard gravity concerns the accuracy of topographic corrections which rely on accurate bathymetric measurements. Since shipboard gravity and bathymetric measurements are taken at the same points, topographic corrections to the free-air gravity are the most accurate possible.

Gravity Data Reduction

A significant portion of the free-air gravity is caused by seafloor topography. Therefore, to investigate subsurface density structure, to which we will relate mantle temperature anomalies, we apply a mantle Bouguer correction. Using Parker's [1973] spectral method, we subtract from the free-air gravity the theoretical gravity signal of the seafloor-water interface and crust-mantle (Moho) interface assuming a crustal layer of constant thickness (6 km) and density (2800 kg/m^3). We take the density of the mantle to be 3300 kg/m^3.

The resulting mantle Bouguer anomaly (MBA) shows that most of the short-wavelength (<100 km) variations caused by local topography are removed, leaving a broad oval-shaped negative anomaly aligned along the spreading axis between ~97°W and ~85°W (outlined by yellow shading, Plate 2a). Superimposed on this oval-shaped anomaly are high-amplitude negative branches over the Cocos Ridge (<-100 mGal) and Galápagos Archipelago (<-300 mGal) reflecting the thickened crust of these edifices. Along the ridge axis, 10-20 mGal variations in MBA occur at segmentation length scales (100-200 km), but the most prominent feature is the long-wavelength decrease by ~90 mGal along axis toward 91°W (Plate 2b). For comparison with other oceanic spreading centers, this 90-mGal anomaly is approximately twice the segmentation-scale MBA variation along the Mid-Atlantic Ridge [e.g., *Lin et al.*, 1990; *Detrick et al.*, 1995] and about 10 times the MBA variation along the East Pacific Rise (8.8°-13.5°N) [*Madsen et al.*, 1990].

The minimum in MBA occurs near 91°W on the southern segment of the 91°W-transform offset, which is also the point of the ridge axis closest to the Galápagos hot spot (point P, Plate 2a). The decrease in MBA is nearly symmetric about point P and uniform along the 650-km ridge length to each side of point P. This wavelength is comparable in extent to topographic swells of other hot spots such as Hawaii (~1500 km across the island chain), Cape Verde (~1500 km in diameter) [*Crough*, 1983], and Iceland (~2000 km in diameter) [*White*, 1988].

Comparison of this along-axis MBA with along-axis variations in bathymetry and basalt chemistry reveals a close correlation between the four anomalies (Figure 1). All anomalies peak at or near point P, all extend over comparable length scales, and all decrease in amplitude nearly symmetrically eastward and westward away from point P. The peak in the La/Sm anomaly coincides with that of K$_2$O, MgO, and a minimum in FeO [*Schilling et al.*, 1982], while the peak in $^{87}Sr/^{86}Sr$ coincides with a minimum in $^{143}Nd/^{144}Nd$ [*Verma et al.*, 1983]. Both geochemical signatures are attributed to a source heterogeneity associated with the Galápagos hot spot [*Verma et al.*, 1983]. Although the peak in $^{87}Sr/^{86}Sr$ occurs ~100 km west of point P, this offset is small relative to the total wavelength of the above

24
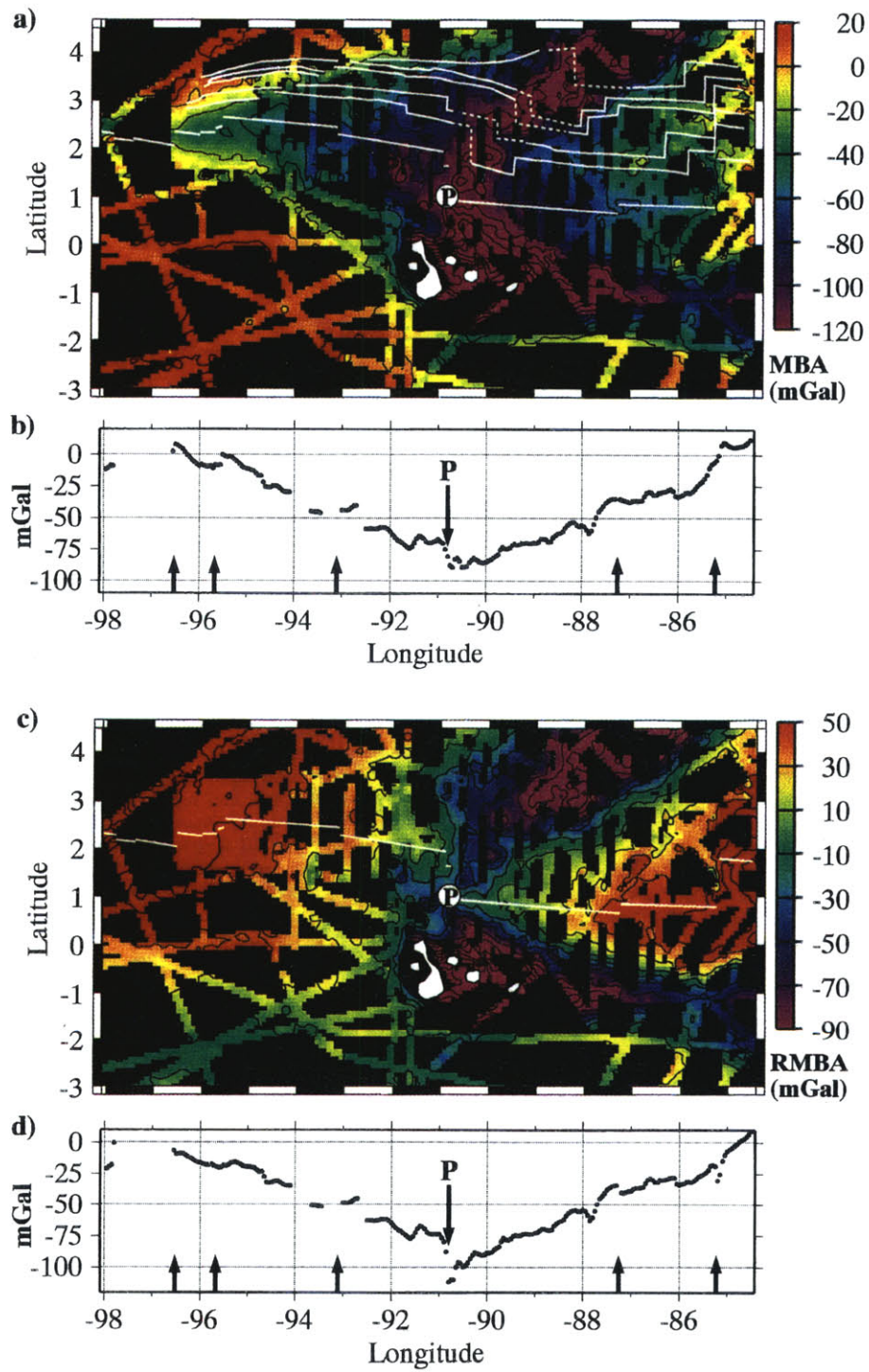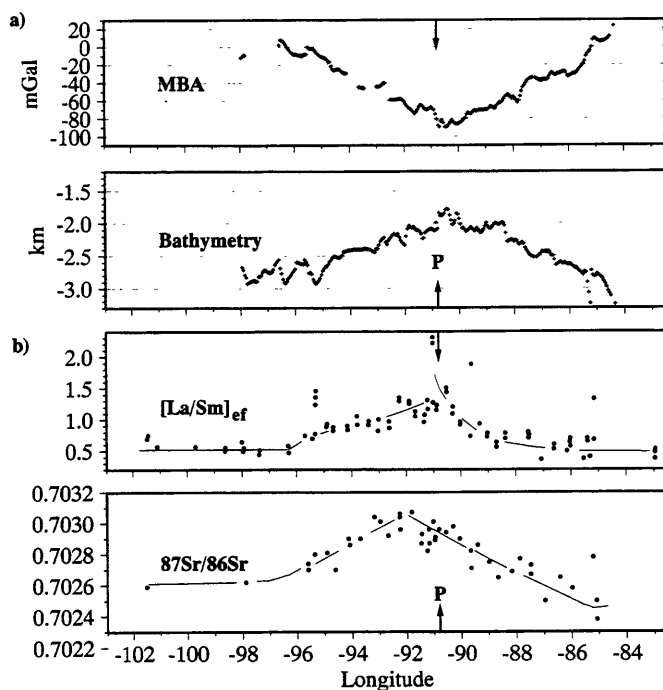
Figure 1. (a) Along-axis mantle Bouguer (MBA) and bathymetry profiles are compared with along-axis variations (b) in [La/Sm]$_{ef}$ and ^{87}Sr/^{86}Sr [*Verma et al.*, 1983]. Note that the peaks for all anomalies except for ^{87}Sr/^{86}Sr coincide at point P.

anomalies and within the 150 to 300-km diameter suggested for intraplate hot spots [*Epp*, 1984; *McNutt*, 1989]. The correlation of MBA and bathymetry with basalt chemistry suggests that the along-axis density structure is closely related to the enriched material introduced by Galápagos plume beneath the ridge axis.

The final step in our gravity analysis is to remove the predictable effects due to lithospheric cooling. Calculation of the three-dimensional (3-D) distribution of temperature-dependent mantle densities for passive mantle upwelling is relatively simple using a standard method first presented by *Phipps Morgan and Forsyth* [1988]. We use a spectral method to solve for flow of a constant-viscosity mantle, driven by two spreading plates with the geometry of the Galápagos spreading center. Using finite difference approximations for the conductive-advective heat

balance equation, we solve for steady state mantle temperatures, from which we derive mantle densities assuming a thermal expansion coefficient of 3.4×10^{-5} °C^{-1}. The integrated gravity fields from each density layer down to a 100-km depth represent the lithospheric cooling contribution to the gravity field [*Kuo and Forsyth*, 1988].

We subtract the lithospheric cooling effects from the MBA to produce the residual mantle Bouguer gravity anomaly (RMBA), shown in Plate 2c. The oval-shaped MBA low, observed between ~97°W and ~85°W, is removed by the lithospheric cooling correction; what remain are high-amplitude negative anomalies branching from the ridge axis, over the Galápagos Archipelago and the Cocos and Carnegie Ridges. These negative RMBA branches reflect the anomalous volcanic and mantle density

Plate 2. (a) Contour and color-shaded map of the mantle Bouguer anomaly. Anomaly values >20 mGal are colored red, while those <-120 mGal are colored violet. Interpolated values between ship tracks are masked, and the spreading center and islands are marked in white. Note the oval-shaped negative anomaly aligned along the spreading center between ~97°W and ~85°W (outlined by the yellow shading) and the negative anomaly branches of the Cocos Ridge and Galápagos Archipelago. The five white profiles north of the spreading center mark isochrons from *Wilson and Hey* [1995] used for the off-axis analysis. Profiles are dashed in regions where magnetic lineations are extrapolated. (b) Mantle Bouguer gravity values extracted along the spreading center. Note that the anomalies reach a minimum at point P, where the ridge axis is closest to the hot spot. The arrows mark locations of transform offsets. (c) Map of residual mantle Bouguer anomaly with contour interval of 20 mGal and a color range of -90 to +50 mGal. Note high-amplitude negative anomalies along the Cocos Ridge, the Darwin-Wolf seamounts, and the Galápagos Islands (shown in white). (d) Along-axis profile of residual mantle Bouguer anomaly showing ~100 mGal decrease from the east and west toward point P. Arrows mark transform offsets.

structure left along the Galápagos hot spot tracks. The dominant effect of the lithospheric correction on the along-axis profiles is to reduce the segment-scale variations in the MBA; it does not appreciably affect the long-wavelength decrease due to the hot spot (Plate 2d). Although the amplitude of the along-axis RMBA is increased slightly (by 10 mGal) from that of the along-axis MBA, the lateral extent and location of the maximum are the same for the two anomalies. For this reason, we focus on the MBA for the remainder of the paper.

Compensation of Topography

The mantle Bouguer correction has been widely used as a first-order correction for oceanic crustal structure [e.g. *Kuo and Forsyth*, 1988; *Lin et al.*, 1990; *Madsen et al.*, 1990; *Blackman and Forsyth*, 1991; *Morris and Detrick*, 1991] since the total global variation in oceanic crustal thickness is ~3 km about a mean of 6 km [*Chen*, 1992]. Our assumption of a constant 6-km-thick crust is merely a first approximation of crustal structure from which we reference departures in density structure. Deviations from this reference model could be lateral variations in crustal thickness, lateral mantle density variations, or a combination of the two. The nonuniqueness of gravity solutions necessitates additional constraints. An obvious constraint is topography since, if in isostatic equilibrium, it too depends directly on density structure. Here we test two modes of isostatic compensation: (1) crustal compensation (Airy isostasy) and (2) compensation from lateral density variations in the mantle (Pratt isostasy).

Airy and Pratt Isostasy Admittance Functions

The theoretical mantle Bouguer gravity anomaly due to the two modes of isostatic compensation is solved using standard spectral methods as follows. In the spectral domain, the mantle Bouguer gravity anomaly $B(\mathbf{k})$ is related to bathymetry $H(\mathbf{k})$ by an isostatic response function, or admittance function $Q(k)$, according to

$$B(\mathbf{k})=Q(k)\cdot H(\mathbf{k}) \qquad (1)$$

where $\mathbf{k}$ is the two-dimensional wavenumber, $k=|\mathbf{k}|=2\pi/\lambda$. Included in $Q(k)$, are the effects of density structure that differs from the "reference" structure (i.e., a crust of uniform thickness overlying a mantle of uniform density). In Airy compensation models, it is the crustal structure that differs from the "reference" since topography is assumed to be supported by laterally varying crustal thickness. If we assume that elevated topography is supported by crust that is anomalously thick, the admittance function must include two terms to account for the effects at two interfaces as follows:

$$Q(k)=-2\pi G[\Delta\rho\exp(-kz_c)+\rho_c\exp(-kz_o)], \qquad (2)$$

where $G=6.67\times10^{-11}$ m^3/kg s^2 is Newton's gravitational constant, $\Delta\rho$ is the crust-mantle density contrast (500 kg/m^3), and ρ_c is the crust-water density contrast (1800 kg/m^3). The first term replaces the attraction of mantle by that of crust at the "reference" Moho (z_c=8.7 is the average seafloor depth of 2.7 km plus 6.0 km). The second term accounts for the effects of the Airy crustal root at its assumed mean depth z_o of 11.0 km beneath the sea surface.

For Pratt compensation, it is mantle density that differs from the "reference" structure since topography is assumed to be compensated by laterally varying mantle densities. The

amplitude of the density reduction in a vertical column required to support a given topographic elevation is $H\rho_m/z_p$ where ρ_m is the mantle-water density contrast (2300 kg/m^3) and z_p is the depth of compensation. The Pratt admittance function must therefore consider the integrated effects of all density layers from z_c to (z_c+z_p) and is thus defined as

$$Q(k) = -2\pi G\rho_m \exp(-kz_c)\frac{[1-\exp(-kz_p)]}{kz_p}. \qquad (3)$$

Results

Mantle Bouguer profiles taken along the present-day ridge axis and selected isochrons (Plate 2a) are compared with the Airy and Pratt theoretical profiles (Figure 2a). The standard deviation misfit between theoretical and observed profiles is plotted versus
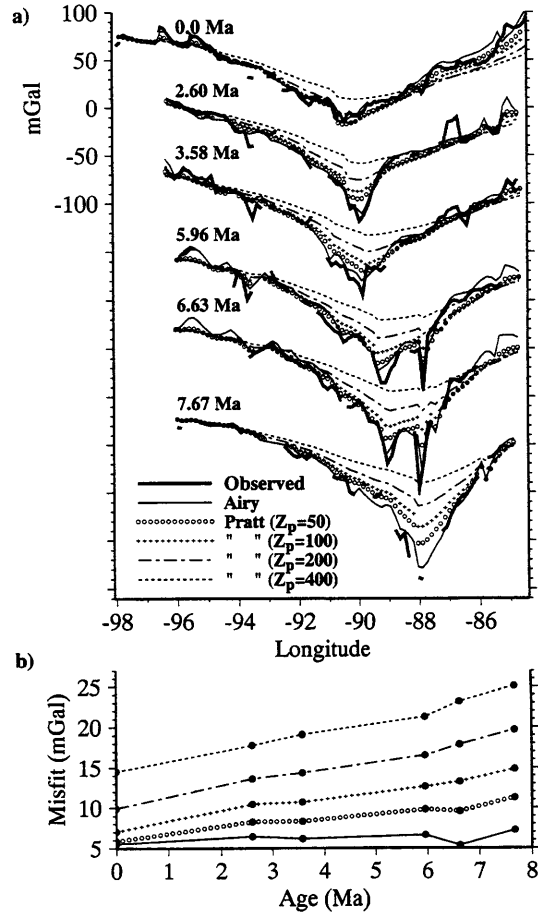
Figure 2. (a) Profiles of observed mantle Bouguer anomalies (shaded profiles) are compared with theoretical models for different assumed compensation mechanisms and depths. The locations of the off-axis crustal isochrons (labeled with ages from *Wilson* [1993]) are in Plate 2c. (b) The standard deviation misfit is plotted against crustal age for the five compensation models tested. Note that models of shallow depths of compensation yield the smaller misfits.

26

age in Figure 2b. For the crustal ages examined (0.0-7.67 Ma) the standard deviation misfit for the Airy compensation profiles has a nearly constant value of ~6 mGal, which is close to our estimated data uncertainty of 5.5 mGal. For the Pratt compensation models, standard deviation misfits increase with compensation depth (z_p) and with age. Along the present-day axis, the Pratt models of z_p=50 and 100 km are the most reasonable with standard deviations of 5.9 and 7.1 mGal, respectively.

Although the Airy profiles yield the lowest misfits to the observed MBA, the Pratt calculations with shallow compensation depths (z_p=50 and 100 km) also yield small misfits. Most of the misfit by the shallow Pratt calculations appears to be due to short-wavelength variations (<200 km) in the observed MBA which may come from local variations in crustal structure. We thus do not exclude the possibility that at least some of the gravity and topographic signal is due to density variations in the shallow mantle. The increase in misfits with age for the Pratt calculations may, however, reflect a decrease in the mantle contribution relative to that of the crust along paleoridge axes.

Topography may also be supported dynamically by lithospheric or upper mantle stresses. Previous work has shown that shallow stresses induced by plate spreading contribute significantly to axial topography [e.g., *Phipps Morgan et al.*, 1987; *Lin and Parmentier*, 1989; *Small and Sandwell*, 1989; *Chen and Morgan*, 1990; *Neumann and Forsyth*, 1993]. *Neumann and Forsyth* [1993], for example, demonstrated that the correlation between gravity and topography along the Mid-Atlantic Ridge is due to dynamic stresses in the lithosphere which depend on crustal thickness and mantle thermal structure. However, for the Galápagos spreading rates of 48-64 mm/yr and possible crustal thickness structure, these extension-related stresses would be small [*Neumann and Forsyth*, 1993]. Significant topography (>1 km) can also be maintained by viscous stresses in a convecting mantle [*Anderson et al.*, 1973; *McKenzie et al.*, 1980]. If viscous stresses are important along the Galápagos spreading center, they must be associated with low densities in the shallow mantle as indicated by our MBA modeling (Figure 2). We thus suggest that the long-wavelength topography of the Galápagos spreading center and nearby Cocos Plate is essentially isostatic and is supported by density anomalies primarily within 100 km beneath the seafloor.

Present-Day Axial Mantle Temperatures

As demonstrated above, crustal thickness and shallow mantle density variations are both likely sources of topographic compensation. We suggest that they both occur and that both are controlled by mantle temperature: crustal thickness by temperature-enhanced melting, and mantle density by thermal expansion. For the following analysis, we investigate the mantle temperature variation required to generate the ~90-mGal variation in along-axis MBA and the ~1.1-km increase in axial topography.

Model Configuration

Using the same numerical methods as were used for the lithospheric cooling calculations, we solve for 3-D mantle temperatures due to passive upwelling; this time, however, we impose a temperature anomaly ΔT at the base layer (Figure 3). To estimate the additional crust that may result from a given ΔT, we take the fraction of partial melting f to depend on mantle temperature T by $f=(T-T_s)/600°$, where T_s is the mantle solidus
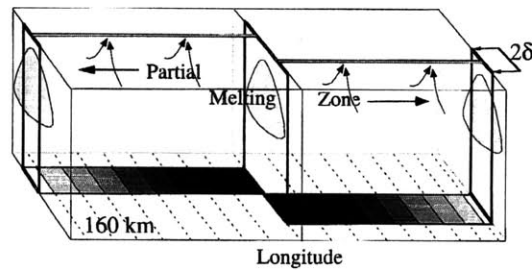
Figure 3. Schematic illustration of our simplified 3-D melt generation models. The ridge axis (shaded gray lines at the top surface) is offset by the 91° transform fault. The region of melt transport, with width 2δ, is outlined by the bold dark lines. The melting zone beneath ridge segments is shown on depth cross sections as shaded triangular shapes; curved arrows denote melt transport toward the ridge axis. The region of melt transport at the base layer is shaded gray according to the imposed temperature with the greatest temperature anomaly near the 91° transform fault.

and 600°C is the supersolidus temperature required to fully melt a unit volume of peridotite [*Reid and Jackson*, 1981]. The rate of melt generation $\dot{f}$ depends on the gradient of f and mantle flow rate **v** by $\dot{f}$=**v**· ∇f [*Reid and Jackson*, 1981]. We estimate the mantle solidus to be linearly dependent on pressure and thus depth z (in kilometers below the seafloor), by T_s=1100°C + 3.25(°C/km)z. Crustal accretion at the ridge crest depends on the spatial distribution of melting and subsequent migration of melt toward the ridge. The process of melt migration is still largely unconstrained; therefore we simplify this calculation by treating ridge segments as line sinks which draw in melt from the mantle below [*Phipps Morgan and Forsyth*, 1988]. Assuming that melt migrates over a finite lateral extent, we define a width δ, on each side of the ridge axis, as the region of melt transport (Figure 3); outside of this melt transportation zone, we assume that melts are carried away by the cooling lithospheric plates thus do not contribute to the crust. We also assume that a small melt fraction f_o is retained in the mantle matrix within this zone of melt transport. We adjust the parameters δ and f_o such that the resulting crustal thickness for a normal base layer temperature (1350°C) is 6 km at the ridge segment centers. This result is achieved for f_o values of 0-6% [*Forsyth*, 1992] and corresponding δ values of 30-50 km. We assume that f_o does not vary along-axis therefore it does not contribute to the long-wavelength variation in mantle density. The base layer is set to a depth of 160 km to ensure that the entire melting region is included.

Base Layer Temperature Distributions

For the base layer temperature anomalies, we investigate three geometries. In our first set of calculations (model A), we vary temperatures linearly along-axis with the maximum anomaly beneath the 91°W transform (Figure 4a). This is the simplest model, designed to test the effects of strictly along-axis variation in temperatures. For the second set of calculations (model B), we impose a circular anomaly centered on the island Fernandina, thought to mark the current location of the Galápagos hot spot center [*White et al.*, 1993] (point H, Figure 4b). Temperatures decrease linearly away from point H. We envision this model to represent the temperature distribution from a radial dispersion of plume material from the hot spot center. For the third set of
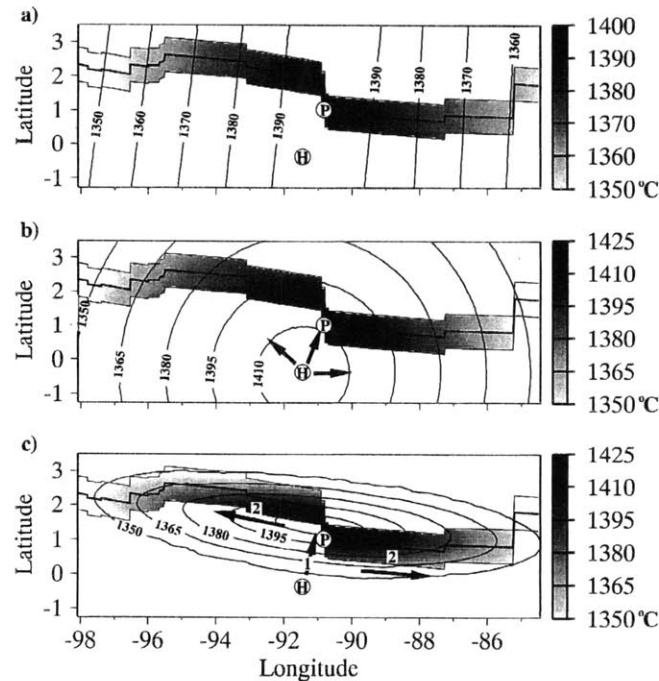
Figure 4. (a) Map of temperatures imposed at the base layer of our best fitting linear model A. Temperatures in the zone of melt transport are shaded to emphasize the importance of this region in gravity and bathymetry calculations. Point H marks the location of the Galápagos hot spot, while point P marks the location of the peak in along-axis MBA and bathymetry. (b) Temperatures imposed at the base layer of our best fitting circular model (model B) with maximum temperature located at point H. Arrows denote hypothetical radial dispersion of hot spot material from point H. (c) Base layer temperatures imposed for our best fitting elliptical model (model C). Arrows denote plume channeling from point H to point P (arrow 1) and then along-axis away from P (arrows 2).

calculations (model C), we use an elliptical temperature anomaly which is centered midway along the 91°W transform and decreases linearly away from the ellipse center (Figure 4c). This model is designed to approximate the temperature distribution along the ridge axis that might result from *Schilling's* [1985, 1991] plume flow model which incorporates ideas of *Vogt* [1976] and *Morgan* [1978]. According to this model, Galápagos plume material feeds through a conduit connecting point H to the ridge axis (arrow 1, Figure 4c), and then disperses preferentially along axis (2 arrows, Figure 4c). We approximate the preferential along-axis flow as an ellipse aligned with the ridge axis. Each of the three models has a base layer temperature maximum near point P directly beneath the ridge axis with a gradual decrease along axis toward the east and west edges of the study region. Gravity and bathymetry calculations for these models are sensitive mostly to temperature conditions within the region of melt transport since only melts in this region are assumed to contribute to accretion of the crust.

Results

Gravity calculations for the three models are done by applying *Parker's* [1973] method to the density layers in the mantle and the crust-mantle interface treating the crustal thickness as only varying along-axis. Since we have shown that the long-wavelength seafloor topography is compensated at shallow

depths, we calculate theoretical bathymetry assuming Airy compensation for the crust and Pratt compensation for the mantle shallower than 160 km. Figures 5a and 5b compare theoretical results of model A for different base layer temperature anomalies[1] at point P (ΔT_p) with observed MBA and bathymetry profiles. Profile sections near transform faults are omitted since our models gave unrealistically small crustal thicknesses due to local cooling effects near ridge segment ends. Removal of these local effects, however, do not affect the larger-scale thermal anomaly related to the Galápagos hot spot.

As illustrated in Figures 5a and 5b, the model for ΔT_p of 50°C best fits both the MBA and bathymetry profiles. The ΔT_p=25 and 75°C solutions are the upper and lower limits for model A. Table 1 outlines the corresponding results of models B and C and the associated standard deviation misfits. Despite differences in the detail 3-D temperature structure between the three models, all three suggest similar values of ΔT_p with comparable minimum misfit. This finding indicates that axial crustal and density structure is sensitive primarily to temperatures directly beneath the ridge axis and insensitive to subtle temperature changes away from the ridge axis. We conclude ΔT_p to be ~50±25°C with a corresponding crustal thickening of 3±1 km (Figure 5c). As the crust thickens toward point P, it gives rise to 70-75% of the topographic swell and MBA gravity signal. The remaining 25-30% of topography and gravity signal is supplied by the anomalously hot and less dense mantle beneath the ridge axis.
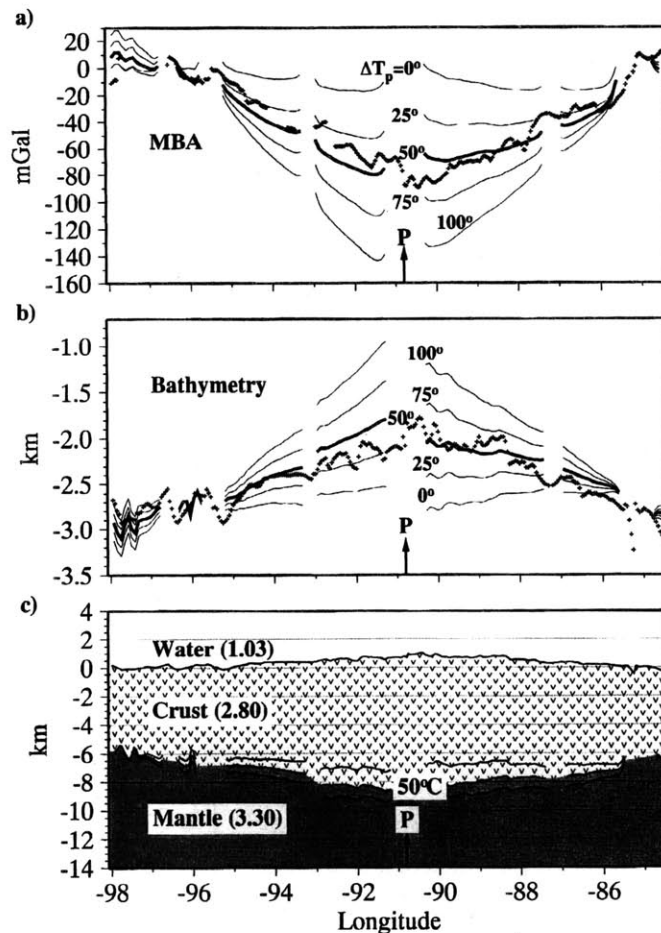
Figure 5. The observed profiles (small crosses) of (a) along-axis MBA and (b) bathymetry are compared with theoretical profiles from model A with different values of point P, base layer temperature anomalies, ΔT_p. Sections of profiles near transform faults are omitted to accentuate the broad wavelength anomaly (solid lines) associated with the hot spot. The best fitting profiles are denoted by bold lines. (c) Predicted along-axis cross section of the crustal structure based on model A results. The Moho is drawn according to our best fitting result (+50°C model); the two other profiles are drawn according to the +25°C (shallower curve) +75°C (deeper curve) results. The Moho boundary is omitted near transform faults as marked by arrows. Densities are in grams per cubic centimeter.

Our crustal model is consistent with estimates of *Feighner and Richards* [1994] based on flexural modeling of gravity near the Galápagos Archipelago. Confirming this crustal model, however, requires future marine seismic experiments since few seismic constraints exist to date.

Discussion

Our primary focus in this study is the effects of mantle temperature on crustal thickness and on mantle density changes by thermal expansion. A number of factors not incorporated into our models may also contribute to crustal thickness and mantle density structure and lead to changes in our ΔT_p estimate. These include (1) compositionally dependent and disequilibrium melting, (2) melt depletion and latent heat loss in the mantle, (3) buoyancy-driven mantle flow, and (4) mantle compositional effects on melting and on mantle densities. We briefly discuss these factors below.

Compositionally dependent and disequilibrium melting. The simple linear melt function and linear depth-solidus relation that we used was defined by *Reid and Jackson* [1981] based on results of batch melting experiments in which melt maintained equilibrium with the remaining solid phases. If melt is extracted rapidly in the mantle such that it fails to equilibrate with the matrix, then the solidus of the depleted residue increases with increasing melt extents [*Kinzler and Grove*, 1992; *Cordery and Phipps Morgan*, 1993]. If this disequilibrium melting scenario is the dominant process in the mantle, then a greater ΔT_p than we estimated may be required beneath the Galápagos spreading center to thicken the crust by 3±1 km.

Melt depletion and latent heat loss in the mantle. In addition to inhibiting melting, melt depletion may also reduce

29

Table 1. Model Results

	MBA		Bathymetry	
	Best Fit ΔT_p, °C	Misfit, mGal	Best Fit ΔT_p, °C	Misfit, km
Model A	50±25	9	50±25	0.13
Model B	49±25	10	49±25	0.13
Model C	47±25	8	49±25	0.14

mantle densities, primarily by decreasing the Fe/Mg ratio of the residue [*Oxburgh and Parmentier*, 1977]. The opposite effect, however, may result from latent heat removal which cools the mantle thus increases its density. Numerical experiments by *Magde et al.* [1995] indicate that to generate an oceanic crust of normal thickness, the two factors would lead to a net decrease in mantle densities of the order of 1%, or ~6 times the thermal expansion effect of heating the mantle by 50°C. This potential density reduction may contribute to the Galápagos bathymetry and gravity anomalies significantly enough that the crustal thickness and thus ΔT_p are smaller than we estimated.

Buoyancy-driven mantle flow. In addition to their direct signature on surface observables, mantle density variations lead to buoyancy forces which drive mantle flow. Beneath normal oceanic spreading centers the dominant sources of buoyancy are most likely melt depletion-related and melt retention-related density reductions [*Jha et al.*, 1994]. If buoyancy forces are important, they are likely to enhance vertical flow and increase the rate of melting and thus may lead to a lower ΔT_p prediction.

Mantle compositional effects on melting and on mantle densities. A hot spot-related temperature anomaly as investigated in this study is an obvious source for thickened crust and reduced mantle densities; however, mantle source heterogeneity may also play important roles. Enrichment in volatile [*Bonatti*, 1990] or incompatible elements [*Michael et al.*, 1994] in the mantle may enhance melting and thus yield a thicker crust for a given mantle temperature anomaly. While there is little evidence for a volatile enrichment beneath the Galápagos spreading center, there is evidence for an increase in incompatible element concentration toward point P from ridge axis samples [*Schilling et al.*, 1982; *Langmuir et al.*, 1992]. In addition, a decrease in Fe/Mg was observed in axial samples toward point P [*Schilling et al.*, 1982; *Langmuir et al.*, 1992], possibly reflecting a low Fe/Mg and thus low-density mantle source near the Galápagos hot spot. Including such heterogeneities of the mantle source in incompatible element content and Fe/Mg ratio may yield a lower ΔT_p estimate.

In summary, while considering factor 1 would increase an estimate of ΔT_p, considering factors 2, 3, and 4 would substantially decrease an estimate of ΔT_p. We therefore anticipate that our estimate of ΔT_p is an upper bound, although the interplay of the above four factors may be complex and requires comprehensive investigation that is beyond the scope of this study.

By considering the first-order aspects of mantle flow, heat transport, and decompression melting, we have established a relation between crustal thickness, temperature-dependent mantle density, and mantle temperature anomaly. Our approach is consistent with previous studies of intraplate hot spot anomalies.

For example, *Crough* [1978], *Sleep* [1990], and *McNutt* [1987] constrained hot spot temperature anomalies based on mantle-density anomalies which they took to be strictly temperature dependent. *McKenzie* [1984] constrained hot spot anomalies based on estimates of crustal thickness assuming, as we do, that melting occurs under equilibrium conditions. Our relationship between ΔT and the mantle component of topography is essentially the same as *Sleep's* [1990], and our relationship between ΔT and crustal thickness is consistent with that of *McKenzie* [1984] (50-75°C for crustal thickening of 2-4 km).

Our constraints on ΔT beneath the Galápagos spreading center have implications for the nature of heat transport both along the ridge axis and from the hot spot to the ridge axis. Using *Feighner and Richard's* [1994] estimate for the volcanic thickness of the Galápagos Archipelago (15-20 km) and *McKenzie's* [1984] melting relationships, we estimate a temperature anomaly of ~200°C at the hot spot center (point H, Figure 6). This temperature estimate is similar to the 214°C anomaly estimated by *Schilling* [1991] based on buoyancy flux arguments. Considering our upper (75°C) and lower (25°C) estimates for the temperature anomaly at point P, the average gradient from the hot spot to the ridge axis (H to P, Figure 6) is 0.74-1.03°C/km. In contrast, the along-axis gradient is only 0.04-0.11°C/km. Therefore any successful models of sublithospheric plume dispersion must yield an along-axis temperature gradient that is an order of magnitude less than that from the hot spot to the ridge axis. Rigorous investigation of this question requires further experimental [*Kincaid*, 1994] and numerical [*Rowley et al.*, 1992] work.

Paleoaxial Temperature Anomalies

To better constrain the temporal evolution of the Galápagos ridge-hot spot system, we next examine MBA and bathymetry anomalies along paleoaxes of the Galápagos spreading center. From our model calculations we derive empirical relations between ΔT and MBA and bathymetry that we then use to estimate past temperature anomalies from the observed amplitudes of along-isochron MBA and bathymetry anomalies. In order to apply relationships derived from the active spreading center to off-axis anomalies, we must make two assumptions. First, we assume that any off-axis crustal accretion on the Cocos Plate is insignificant and that the spreading rate has not changed significantly over the past 7.7 m.y. Second, we assume the
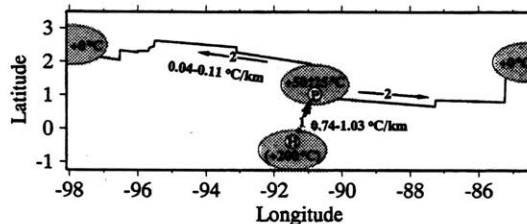
Figure 6. Map of the Galápagos region marked with estimated base layer temperature anomalies at various points along the ridge axis (solid line) and at the hot spot center (point H). Arrows point in the direction of decreasing temperature anomalies from the hot spot to ridge-axis (arrow 1) and along the ridge axis (arrows 2). Estimated temperature gradients in both directions are labeled. Note that gradient 1 is 10-20 times greater than gradient 2.
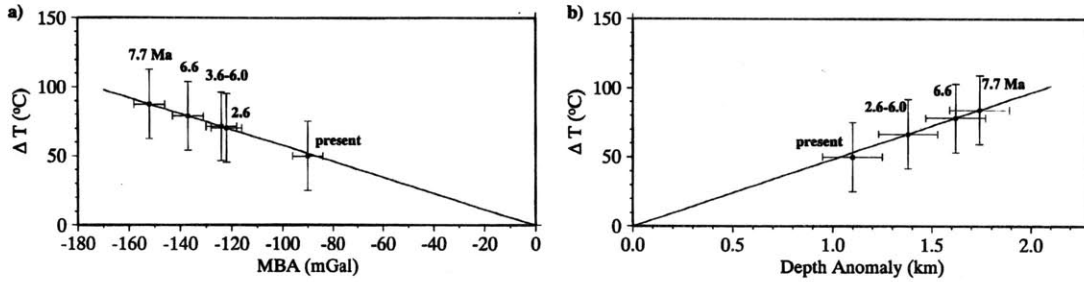
Figure 7. The empirical relationships between base layer temperature anomaly and (a) MBA and (b) bathymetry anomaly (solid lines). Also plotted are derived ΔT values for maximums in observed MBA and bathymetry along crustal isochrons (dots). Errors in gravity (12 mGal) and bathymetry (0.3) are the estimated variations due to ridge segmentation, while errors in ΔT are ±25°C, as defined according model A results.

observed MBA and bathymetry along isochrons are due primarily to the crustal structure that was frozen into the lithosphere at the time of accretion.

Our linear melting function yields an essentially linear relation between ΔT and MBA and bathymetry. This relation is derived empirically by a least squares fit between theoretical values of MBA and bathymetry and corresponding values of base layer ΔT for model A calculations. Only points further than ~80 km from transform offsets are used in the fit. The dependence of ΔT on MBA is found to be

$$\Delta T = -0.576 \Delta MBA \qquad (4)$$

with a < 3°C standard deviation misfit to model calculations. The dependence of ΔT on depth anomaly ΔH is found to be

$$\Delta T = 48.3 \Delta H \qquad (5)$$

with a < 5°C standard deviation misfit to model calculations.

Using the peak mantle Bouguer and bathymetry anomalies along each isochron, we derive peak temperature anomalies beneath paleospreading centers (Figure 7). Along the 7.7 Ma isochron the observed MBA is ~150 mGal, and bathymetry
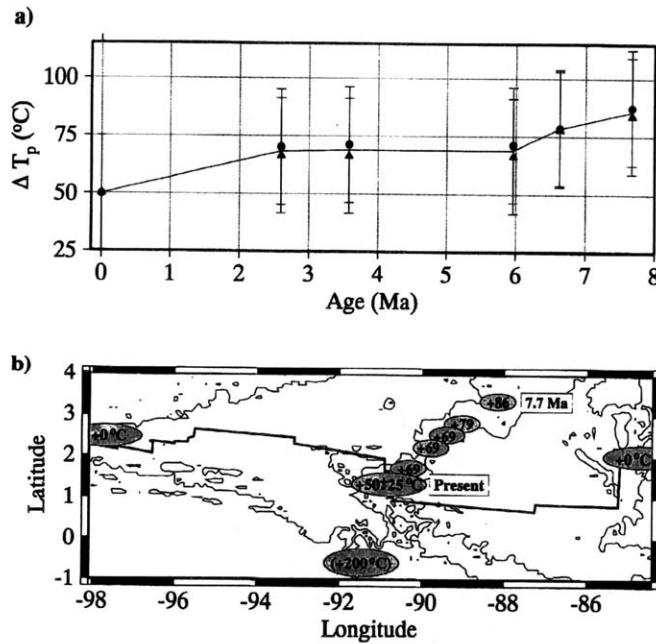
Figure 8. (a) Peak base layer ΔT calculated from MBA (circles) and bathymetry anomalies (triangles) along selected isochrons are plotted against the isochron ages. The solid line marks ΔT averaged between the gravity and bathymetry calculations. The uncertainty of ±25°C in ΔT is the uncertainty estimated from results for the present-day ridge axis. (b) Map showing the Galápagos hot spot and the locations of peak temperature anomalies along the present and paleoaxes of the Galápagos spreading center. The 3.0-, 2.0-, and 1.0-km depth intervals are contoured, and the ridge axis is marked as a bold solid line.

31

anomaly is ~1.7 km; these anomalies yield a past temperature anomaly of ~86±25°C, 70% greater than the anomaly along the present-day ridge axis. As shown in Figure 8a both MBA (circles) and bathymetry (triangles) relationships produce consistent temperature anomalies.

Also illustrated in Figure 8a is the decrease in amplitudes of the MBA and bathymetry anomalies with decreasing isochron age. This behavior indicates that the peak temperature anomaly beneath the Galápagos spreading center has steadily decreased since 7.7 Ma, when the hot spot was at or near the ridge axis. As the hot spot migrated southwest away from the ridge axis beneath the Nazca Plate, the maximum in ΔT decreased and the axial position of the peak in ΔT moved westward at approximately the same rate as the westward velocity component of the hot spot with respect to the Cocos Plate (Figure 8b). If we assume that the temperature anomaly of the hot spot has remained constant over the past ~8 m.y., the above results provide evidence that the amplitude of temperature anomaly beneath the Galápagos ridge axis is a function of the distance separating the hot spot and ridge axis. Such a dependence may reflect the cooling of plume material as it migrates from the Galápagos hot spot to the ridge axis and may provide importance constraints on the mechanisms of heat transfer between hot spots and nearby ridges.

Conclusions

The 2-D pattern of the mantle Bouguer and bathymetry anomalies reflect temperature-dependent density structure imposed by the Galápagos hot spot. Correlation of MBA and bathymetry with geochemical anomalies supports the notion of mixing of a hot, enriched plume with the cooler, depleted upper mantle. Profiles of mantle Bouguer gravity anomalies taken along isochrons of ages 0.0-7.67 Ma indicate that long-wavelength topography is isostatically compensated by density structure in the crust and upper 100 km of the mantle. To account for the ~90 mGal along-axis decrease in MBA and the ~1.1 km decrease in depth, our models require a subaxial temperature anomaly of 50±25°C and an associated crustal thickness increase of 3±1 km. Mantle temperatures decrease dramatically from the hot spot to the ridge axis but decrease much more gradually along axis with a lateral temperature gradient 10-20 times less. This contrast places important constraints on hot spot-to-ridge and along-ridge heat transport.

From the crustal isochron of age 7.7 Ma to the present-day axis, the along-isochron amplitudes of MBA decrease from ~150 to ~90 mGal. The corresponding along-isochron bathymetry anomalies decrease from ~1.7 to ~1.1 km. These MBA and bathymetry anomalies indicate that the axial temperature anomaly was 70% hotter in the past (86±25°C) and has steadily decreased to 50±25°C as the ridge axis migrated away from the Galápagos hot spot. The simplest explanation for this apparent decrease in the mantle anomaly beneath the Galápagos spreading center since 7.7 Ma is that the ridge axis temperature structure depends on the distance separating the hot spot and ridge axis. These conclusions point to the need for further experimental and numerical investigations to better understand the dynamic interaction between the Galápagos spreading center and hot spot and the effects of such interactive processes on the internal structure of the oceanic lithosphere.

References

Anderson, R N., D. McKenzie, and J. G. Sclater, Gravity, bathymetry and convection in the Earth, *Earth Planet Sci. Lett*, *18*, 391-407, 1973

Bell, R E , and W.R. Buck, Crustal control of ridge segmentation inferred from observations of the Reykjanes Ridge, *Nature, 357*, 583-586, 1992

Blackman, D. K , and D. W Forsyth, Isostatic compensation of tectonic features of the Mid-Atlantic Ridge: 25-27°30'S, *J Geophys Res, 96*, 11,741-11,758, 1991.

Bonatti, E., Not so hot "hot spots" in the oceanic mantle, *Science, 250*, 107-251, 1990

Chen, Y. J , Oceanic crustal thickness versus spreading rate, *Geophys. Res. Lett., 19*, 753-756, 1992.

Chen, Y , and W J. Morgan, Rift valley/no rift valley transition at mid-ocean ridges, *J. Geophys. Res., 95*, 17,571-17581, 1990

Cochran, J. R., and M. Talwani, Free-air gravity anomalies in the world's oceans and their relationship to residual elevation, *Geophys J R. Astron Soc., 50*, 495-552, 1977

Cordery, M. J., and J. Phipps Morgan, Convection and melting at mid-ocean ridges, *J Geophys Res, 98*, 19,477-19,503, 1993

Crough, S T , Thermal origin of mid-plate hot-spot swells, *Geophys J. R. Astron. Soc., 55*, 451-469, 1978

Crough, S. T , Hotspot swells, *Annu. Rev. Earth Planet Sci., 11*, 165-193, 1983

DeMets, C , R G. Gordon, D. F Argus, and S Stein, Current plate motions, *Geophys. J. Int , 101*, 425-478, 1990

Detrick, R. S., H. D Needham, and V. Renard, Gravity anomalies and crustal thickness variations along the Mid-Atlantic Ridge between 33°N and 40°N, *J. Geophys. Res.*, in press, 1995.

Epp, D., Possible perturbations to hotspot traces and implications for the origin and structure of the Line Islands, *J Geophys Res , 89*, 11,273-11,286, 1984.

Feighner, M.A., and M. A. Richards, Lithospheric structure and compensation mechanisms of the Galápagos Archipelago, *J Geophys. Res , 99*, 6711-6729, 1994.

Forsyth, D. W., Seismological constraints on partial melting beneath the East Pacific Rise (abstract), *Eos Trans. AGU, 73* (14), Spring Meeting suppl., 290, 1992.

Hart, S. R., J.-G. Schilling, and J. L. Powell, Basalts from Iceland and along the Reykjanes Ridge. Sr isotope geochemistry, *Nature Phys. Sci , 246*, 104-107, 1973.

Hey, R., Tectonic evolution of the Cocos-Nazca spreading center, *Geol. Soc. Am. Bull., 88*, 1404-1420, 1977.

Jha, K., E. M. Parmentier, and J. Phipps Morgan, The role of mantle-depletion and melt-retention buoyancy in spreading-center segmentation, *Earth Planet. Sci. Lett.*, 125, 221-234, 1994.

Kincaid, C., Laboratory experiments on the dynamics of plume-ridge interaction (abstract), *Eos Trans. AGU, 75* (16), Spring Meeting suppl., 336, 1994

Kinzler, R. J , and T. L. Grove, Primary magmas of mid-ocean ridges and basalts 2. Applications, *J. Geophys. Res., 97*, 6907-6926, 1992.

Kuo, B.-Y., and D. W. Forsyth, Gravity anomalies of the ridge-transform system in the South Atlantic between 31° and 34.5°S: Upwelling centers and variations in crustal thickness, *Mar. Geophys. Res., 10*, 205-232, 1988.

Langmuir, C. H., E. M. Klein, and T. Plank, Petrological systematics of mid-ocean ridge basalts: constraints on melt generation beneath ocean ridges, in *Mantle Flow and Melt Generation at Mid-Ocean Ridges, Geophys. Monogr. Ser.*, vol. 71, edited by J. Phipps Morgan, D. K.

Blackman, and J M. Sinton, pp 183-280, AGU, Washington, D C, 1992

Lin, J, and E. M. Parmentier, Mechanisms of lithospheric extension at mid-ocean ridges, Geophys. J, 96, 1-22, 1989

Lin, J., and J Phipps Morgan, The spreading rate dependence of three-dimensional mid-ocean ridge gravity structure, Geophys Res Lett, 19, 13-16, 1992.

Lin, J., G. M. Purdy, H Schouten, J -C. Sempere, and C. Zervas, Evidence for focused magmatic accretion along the Mid-Atlantic Ridge, Nature, 344, 627-632, 1990

Madsen, J. A, R. S. Detrick, J. C Mutter, and P Buhl, A two- and three-dimensional analysis of gravity anomalies associated with the East Pacific Rise at 9°N and 13°N, J Geophys. Res., 95, 4967-4987, 1990.

Magde, L, R. S. Detrick, and the Tera Group, The crust and upper mantle contribution to the axial gravity anomaly at the southern East Pacific Rise, J Geophys. Res., in press, 1995

McKenzie, D, The generation and compaction of partially molten rock, J. Petrol, 25, 713-765, 1984.

McKenzie, D, A. Watts, B. Parsons, and M Roufosse, Planform of mantle convection beneath the Pacific Ocean, Nature, 288, 422-446, 1980

McNutt, M, Temperature beneath midplate swells: The inverse problem, in Seamounts, Islands, and Atolls, Geophys. Monogr Ser., vol. 43, edited by B. Keating and R. Batiza, pp 123-132, AGU, Washington, D C., 1987.

McNutt, M, The origin of the Marquesas fracture zone ridge and its implications for the nature of hot spots., Earth Planet. Sci. Lett., 91, 381-393, 1989

Michael, P. J, et al., Mantle control of a dynamically evolving spreading center: Mid-Atlantic Ridge 31-34°S, Earth Planet. Sci Lett., 121, 451-468, 1994

Morgan, W. J., Rodriguez, Darwin, Amsterdam, .., A second type of hotspot island, J. Geophys Res, 83, 5355-5360, 1978.

Morris, E., and R. S Detrick, Three-dimensional analysis of gravity anomalies in the MARK area, Mid-Atlantic Ridge 23°N, J. Geophys. Res., 96, 4355-4366, 1991

Neumann, G. A., and D. W. Forsyth, The paradox of the axial profile. Isostatic compensation along the axis of the Mid-Atlantic Ridge?, J Geophys. Res, 98, 17,891-17,910, 1993

Oxburgh, E. R, and E. M. Parmentier, Compositional and density stratification in the oceanic lithosphere—Causes and consequences, J. Geol. Soc London, 133, 343-354, 1977.

Parker, R. L., The rapid calculation of potential anomalies, Geophys J. R. Astron Soc, 31, 447-455, 1973

Parmentier, E. M, and J. Phipps Morgan, The spreading rate dependence of three-dimensional spreading center structure, Nature, 348, 325-328, 1990

Phipps Morgan, J., and D. W Forsyth, Three-dimensional flow and temperature perturbations due to a transform offset: Effect on oceanic crustal and upper mantle structure, J. Geophys. Res., 93, 2955-2966, 1988.

Phipps Morgan, J., and M. C. Kleinrock, Transform zone migration: Implications of bookshelf faulting at oceanic and Icelandic propagating rifts, Tectonics, 10, 920-935, 1991.

Phipps Morgan, J., E. M. Parmentier, and J. Lin, Mechanisms for the origin of mid-ocean ridge axial topography: Implications for the thermal and mechanical structure of accreting plate boundaries, J Geophys Res., 92, 12,823-12,836, 1987.

Prince, R. A, and D. W. Forsyth, A simple objective method for minimizing crossover errors in marine gravity data, Geophysics, 49, 1070-1083, 1984

Prince, R. A., and D W. Forsyth, Horizontal extent of anomalously thick crust near the Vema Fracture Zone from the three-dimensional analysis of gravity anomalies, J. Geophys Res., 93, 8051-8063, 1988

Reid, I., and H. R. Jackson, Oceanic spreading rate and crustal thickness, Mar. Geophys Res, 5 165-172, 1981

Rowley, C., C. W. Gable, and C. Kincaid, Dynamical interaction between

upper mantle plumes and a spreading ridge Three-dimensional experiments (abstract), Eos Trans AGU, 73 (43), Fall Meeting suppl., 582, 1992

Schilling, J.-G, Iceland mantle plume geochemical evidence along Reykjanes Ridge, Nature, 242, 565-571, 1973

Schilling, J.-G., Rare-earth variations across "normal" segments of the Reykjanes Ridge, 60°-53°N, Mid-Atlantic Ridge, 29°S, and East Pacific Rise, 2°-19°S, and evidence on the compositions of the underlying low velocity layer, J Geophys. Res, 80, 1459-1473, 1975a.

Schilling, J -G., Azores mantle blob Rare earth evidence, Earth Planet. Sci. Lett., 25, 103-115, 1975b

Schilling, J.-G., Upper mantle heterogeneities and dynamics, Nature, 314, 62-67, 1985.

Schilling, J -G., Fluxes and excess temperatures of mantle plumes inferred from their interaction with migrating mid-ocean ridges, Nature, 352, 397-403, 1991.

Schilling, J.-G., R. N. Anderson, and P Vogt, Rare earth, Fe and Ti variations along the Galapagos spreading centre, and their relationship to the Galapagos mantle plume, Nature, 261, 108-113, 1976.

Schilling, J.-G., R. Kingsley, and J Devine, Galapagos hot spot-spreading center system, 1, Spatial petrological and geochemical variations (83W-101°W), J Geophys. Res., 87, 5593-5610, 1982

Sleep, N. H, Hotspots and mantle plumes: Some phenomenology, J Geophys. Res., 95, 6715-6736, 1990.

Small, C., and S. T. Sandwell, An abrupt change in the ridge axis gravity with spreading rate, J Geophys. Res, 94, 17,383-17,392, 1989.

Sparks, D. W, E. M. Parmentier, and J Phipps Morgan, Three-dimensional mantle convection beneath a segmented spreading center: Implications for along-axis variations in crustal thickness and gravity, J Geophys Res., 98, 21,977-21,995, 1993.

Verma, S. P., and J.-G. Schilling, Galapagos hot spot-spreading center system, 2, 87Sr/86Sr and large ion lithophile element variations (85°W-101°W), J Geophys. Res., 87, 10,838-10,856, 1982.

Verma, S. P, J -G. Schilling, and D G Waggoner, Neodymium isotopic evidence for Galapagos hotspot-spreading centre system evolution, Nature, 306, 654-657, 1983.

Vink, G E., A hotspot model for Iceland and the Voring Plateau, J Geophys Res., 89, 9949-9959, 1984.

Vogt, P. R, Plumes, subaxial pipe flow, and topography along the mid-oceanic ridge, Earth Planet Sci Lett., 29, 309-325, 1976

White, R. S, A hot-spot model for early Tertiary volcanism in the N Atlantic, in Early Tertiary Volcanism and the Opening of the NE Atlantic, edited by A.C Morton and L.M. Parson, Spec. Publ. Geol. Soc. London, 39, 3-13, 1988.

White, W M, S. R. Hart, and J -G Schilling, Geochemistry of the Azores and the Mid-Atlantic Ridge: 29°N to 60°N, Yearbook Carnegie Inst Washington, 74, 224-234, 1975.

White, W M., J.-G. Schilling, and S R. Hart, Evidence for the Azores mantle plume for strontium isotope geochemistry of the central north Atlantic, Nature, 263, 659-663, 1976.

White, W M., A. R McBirney, and R A. Duncan, Petrology and geochemistry of the Galápagos Islands. Portrait of a pathological mantle plume, J Geophys. Res., 98, 19,533-19,563, 1993.

Wilson, D. S., Confidence intervals for motion and deformation of the Juan de Fuca plate, J. Geophys. Res, 98, 16,053-16,071, 1993.

Wilson, D. S. and R. N. Hey, History of rift propagation and magnetization intensity for the Cocos-Nazca spreading center, J Geophys. Res., in press, 1995.

G. Ito and J. Lin, Department of Geology and Geophysics, Woods Hole Oceanographic Institution, Woods Hole, MA 02543 (e-mail: gito@magellan.whoi.edu; jlin@whoi edu)

CHAPTER 2

OCEANIC SPREADING CENTER-HOTSPOT INTERACTIONS: CONSTRAINTS FROM ALONG-AXIS BATHYMETRIC AND GRAVITY ANOMALIES

Oceanic spreading center–hotspot interactions: Constraints from along-isochron bathymetric and gravity anomalies

Garrett Ito   Woods Hole Oceanographic Institution–Massachusetts Institute of Technology Joint Program in Oceanography, Woods Hole, Massachusetts 02543
Jian Lin   Woods Hole Oceanographic Institution, Woods Hole, Massachusetts 02543

ABSTRACT

We analyzed bathymetric and gravity anomalies along present and paleoaxes of oceanic spreading centers influenced by the Iceland, Azores, Galápagos, Tristan, and Easter hotspots. Residual bathymetry (up to 4.7 km) and mantle Bouguer gravity (up to −340 km) anomalies are maximum at on-axis hotspots and decrease with increasing ridge-hotspot separation distance (D), until becoming insignificant at D ~500 km. Along-isochron widths of bathymetric anomalies (up to 2700 km) depend inversely on paleo–spreading rate, reflecting the extent to which plume material will flow along axis before being swept away by the spreading lithosphere. Flux balance arguments suggest that the five hotspots feed material to ridges with comparable fluxes of ~2.2 × 10⁶ km³/m.y. Assuming that the amplitudes of these geophysical anomalies reflect temperature-dependent crustal thickness and mantle density variations, we suggest that ridge temperature anomalies are maximum (150–225 °C) when plumes are ridge centered and decrease with increasing ridge-hotspot distance due to cooling of the ridgeward-migrating plume material.

INTRODUCTION

When mantle plumes rise near oceanic spreading centers, they generate not only near-ridge hotspots, but also melt anomalies at the axis of the nearby ridges (e.g., Morgan, 1978). Direct evidence that near-ridge plumes divert toward and feed ridges is the ocean-island basalt (OIB) geochemical signature in ridge basalts (e.g., Hart et al., 1973). Furthermore, along-axis gradients in the strength of OIB signatures and in topography (e.g., Vogt, 1976; Schilling, 1991) indicate that once a plume reaches a ridge, it spreads laterally along axis.

Previous studies of ridge-plume interactions have focused primarily on present-day spreading centers. Ito and Lin (1995), however, demonstrated that 70%–75% of off-axis bathymetric and gravity anomalies of the Cocos plate can be attributed to the anomalous crustal thicknesses generated at the paleo-Galápagos ridge axis. We attributed long-wavelength (>200 km) variations in bathymetry and gravity along crustal isochrons to temperature conditions beneath the hotspot-influenced ridge axis at the time the crust was created.

In this study we investigated the evolution of five prominent plume-ridge systems over wide ranges in ridge-hotspot separation distance and spreading rate. The results of this study provide observational constraints on the amplitudes of along-isochron bathymetric and gravity anomalies as they depend on ridge-hotspot separation distance, and along-isochron widths of bathymetric anomalies as they depend on ridge spreading rate.

ALONG-ISOCHRON BATHYMETRIC AND GRAVITY ANOMALIES

Iceland, Azores, Tristan, Galápagos, and Easter (Fig. 1) are the five hotspots that impose the most prominent bathymetric and geo-
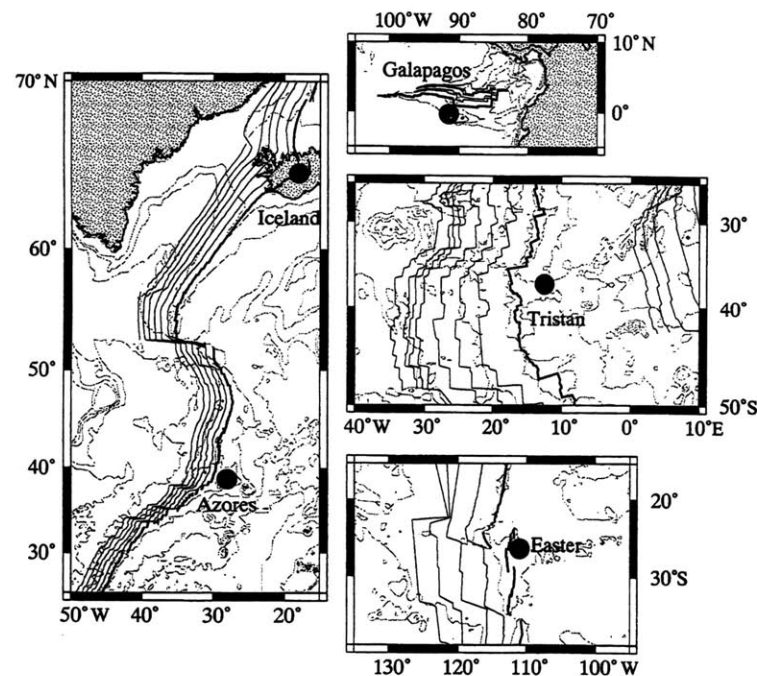
Figure 1. Regional bathymetric maps (mercator projections) of five prominent hotspot-ridge systems: Iceland, Azores, and Tristan, near Mid-Atlantic Ridge; Galápagos, near Galápagos spreading center; and Easter, near East Pacific Rise. Etopo5 (Earth topography at 5 minute grid spacing, National Geophysical Data Center Report MGG-5) bathymetry points within 5 min of ship data points were omitted before gridding at 5 min grid spacing. Circles mark present-day locations of hotspots; solid lines mark ridge axes and off-axis isochrons along which data profiles were taken. To exclude sea floor affected by off-axis volcanism we used isochrons of ages 0–30 Ma for Iceland and 0–25 Ma for Azores on North American plate; 0–8 Ma for Galápagos on Cocos plate; and 0–20 Ma for Easter on Pacific plate. For Tristan, we used isochrons of ages 0–70 Ma on South American plate and ages 80–110 Ma on African plate because hotspot crossed from South American to African plate at ~80 Ma (O'Connor and Duncan, 1990).

657

37

chemical anomalies observed at nearby oceanic spreading centers (Hart et al., 1973; Hamelin et al., 1984; Schilling, 1985). Encompassing each of the five systems, we obtained shipboard bathymetric data from the National Geophysical Data Center (NGDC) and Lamont-Doherty Earth Observatory (LDEO), and gridded bathymetry from NGDC. To derive residual bathymetry, we first corrected the raw data for isostatic effects of sediment loading and then subtracted predicted depths of a cooling mantle half space (Carlson and Johnson, 1994). Sediment thicknesses were obtained from the LDEO database (A. Cazenave, Centre National d'Etudes Spatiales, Toulouse, France), and density contrasts between the sediments and mantle, and mantle and water were assumed to be 1600 kg/m^3 and 2300 kg/m^3, respectively.

Free-air gravity data were taken from the ship surveys and the satellite altimetry-derived gravity grid of Sandwell and Smith (1992). To isolate the effects of sub–sea-floor density structure, we generated mantle Bouguer anomalies by subtracting from the free-air gravity the attractions of the sea-floor–water (density contrast, $\Delta\rho$ = 1800 kg/m^3) and crust-mantle ($\Delta\rho$ = 500 kg/m^3) interfaces using raw bathymetry, and assuming a crust of uniform thickness (6.5 km) (e.g., Kuo and Forsyth, 1988).

Coordinates of present-day ridge axes and crustal isochrons were defined by using plate boundary and age data of Müller et al. (1993a). Because our focus was on anomalies generated at the axes of spreading centers, we considered only data from sea floor unaffected by off-axis volcanism, as detailed in the Figure 1 caption. From our residual bathymetry and mantle Bouguer grids, we then extracted along-isochron profiles (Fig. 2).

ANOMALY AMPLITUDES VS. PALEORIDGE-HOTSPOT DISTANCE

To determine hotspot locations relative to paleo–spreading centers, we assumed that the hotspots were stationary with respect to each other and used plate-reconstruction poles (Lonsdale 1988;
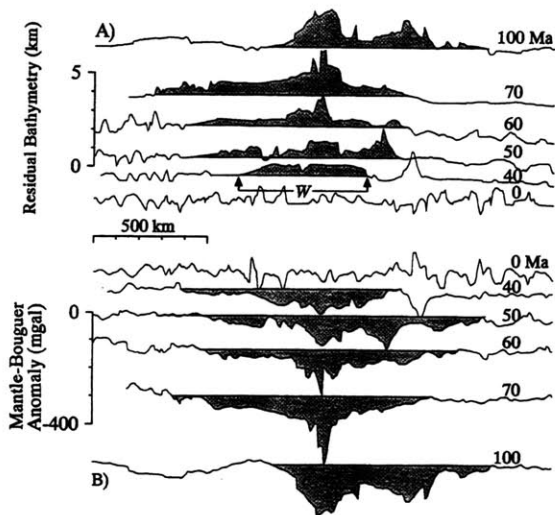
Figure 2. (A) Residual bathymetry (RB) and (B) mantle Bouguer anomaly (MBA) profiles along six example isochrons of Tristan system. Shaded parts mark long-wavelength signals we attribute to hotspots. W defines along-isochron width over which long-wavelength topographic swells are shallower than depths predicted by cooling half-space reference model. ΔRB and ΔMBA are maximum amplitudes along each profile. Decrease in amplitudes with decreasing isochron age coincide with migration of Tristan hotspot away from ridge axis since ~80 Ma when it was ridge centered.

Müller et al., 1993b) to rotate isochrons with respect to the hotspots back to their positions at the time of accretion. We then measured distances between the paleo–ridge axes and hotspot centers, which we took to be the locations of most recent volcanism.

The along-isochron variations in residual bathymetric (ΔRB) and mantle Bouguer anomalies (ΔMBA) display a decrease with increasing paleoridge-hotspot distance (D, Fig. 3). The on-ridge hotspot cases (D <50 km) for the Tristan system (80–90 Ma isochrons) and Iceland system (0–30 Ma isochrons) display the highest $\Delta RB$ (3.5–4.7 km) and most negative ΔMBA (−250 to −340 mgal), which are approximately twice those of ridge-centered cases for the Galápagos and Azores systems. At $D \sim 500$ km, the hotspot signals become very weak and in the case of Tristan, become indistinguishable from normal ridge-segmentation–related variations. The individual Galápagos and Tristan systems show a decrease in ΔRB and ΔMBA with increasing D, whereas the Azores system is more complex and the Easter trend is very weak. The predominant decrease of ΔRB and ΔMBA with increasing D is consistent with Schilling's (1985) study of present-day ridge-axis bathymetry.

ANOMALY WIDTHS VS. PALEO–SPREADING RATE

Whereas amplitudes of ΔRB and ΔMBA are functions of ridge-hotspot distance, along-isochron widths (W) of the bathymetric anomalies (see Fig. 2 caption) depend primarily on the full spreading rate (U) at the time of crustal accretion. The maximum values of W are found along the slowest-spreading Mid-Atlantic Ridge near Iceland (2700 km, Fig. 4A); these values are comparable to the along-axis extent of the helium isotope anomaly, but are a factor of two greater than the widths of rare-earth-element anomalies (Schilling, 1986). Values of W decrease with increasing U to a minimum along the fast-spreading East Pacific Rise.

The observed dependence of W on spreading rate lends strong support to previous notions of along-axis plume material flow (Vogt, 1976; Schilling, 1985). Similarly to Schilling (1991), we estimate that the flux of plume material feeding the ridge (Q) is eventually carried away by the spreading lithospheric plates (Fig. 4A, inset), such that

$$Q = \int_{-W/2}^{W/2} P(y)hU \, dy = \frac{hUW}{2}, \tag{1}$$

where y is the along-axis coordinate, h is the thickness of the fully developed lithosphere (assumed to be 80 km), and $P(y)$ is the percentage of accreted lithosphere derived from the plume material assumed to decrease linearly from 1 at $y = 0$ to 0 at $y = \pm W/2$.

We treat the hotspot to ridge flow as a simple laminar flow problem in which the lithospheric drag opposes the ridgeward flow of plume material. The channel connecting the ridge and hotspot has a characteristic width w_1 and thickness w_2 (see Fig. 4, A and B, insets). Therefore, the net flux from the hotspot to the ridge is

$$Q = w_1 w_2 \left(V - \frac{U}{4} \right), \tag{2}$$

where V is the average ridgeward velocity of plume flow, $w_1 w_2 V$ is the ridgeward flux, and $w_1 w_2 U/4$ is the opposing plate-driven flux. Combining equations 1 and 2 yields the dependence of W on spreading rate,

$$W = \left(\frac{2w_1 w_2}{hU} \right) \left(V - \frac{U}{4} \right). \tag{3}$$

The solid curve in Figure 4A is that predicted for assumed values of $V = 70$ km/m.y. and $w_1 w_2 = 3 \times 10^4$ km^2, which yields a root-mean-square misfit to the data of 500 km. Similar misfits are achieved for $V = 30$–100 km/m.y. and corresponding values of $w_1 w_2$ of 8–2 $\times 10^4$ km^2. These results suggest that the ridgeward fluxes from the five
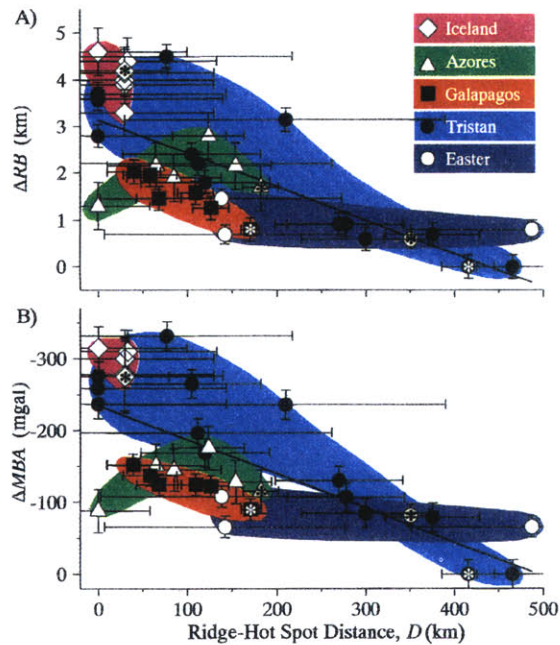
38

Figure 3. Along-isochron amplitudes of (A) ΔRB and (B) ΔMBA plotted against distance between paleo–ridge axes and hotspots at times corresponding to isochron ages. Asterisks mark present-day ridge-axis anomalies; solid lines are those that best fit all data. Uncertainties in ΔRB and ΔMBA are segmentation-scale variations (Lin and Phipps Morgan, 1992) that are independent of larger wavelength hotspot signals. Uncertainties in D reflect uncertainties in isochron ages and in plate motion relative to hotspots (Cande and Kent, 1992).

hotspots are comparable, the average value being $\sim 2.2 \times 10^6$ km^3/m.y. Increasing or decreasing $w_1 w_2 V$ by 1×10^6 km^3/m.y. increases the data misfit by a factor of two.

Our theoretical relation between W and U is based on one end-member scenario in which lateral spreading of plume material beneath ridges is strictly ridge parallel. A numerical study that considers both ridge-parallel and ridge-perpendicular spreading of plumes beneath ridges (Feighner et al., 1995) may represent the other end member; it thus predicts that W is proportional to $(Q/U)^{1/2}$ rather than (Q/U), as does our model.

PALEO–RIDGE-AXIS TEMPERATURE ANOMALIES

We show here how the amplitudes of ΔRB and ΔMBA may reflect the temperature anomalies beneath the paleo–ridge axes. We assume that ΔRB and ΔMBA arise from crustal-thickness and mantle-density anomalies, both of which depend on the ridge-axis temperature anomaly at the time of crustal accretion. ΔRB and ΔMBA can be related to a hotspot-induced mantle temperature anomaly (ΔT) using the model of Ito and Lin (1995), which considered changes in mantle density by thermal expansion, and in crustal thickness by increased decompression melting. Assuming passive mantle upwelling, Ito and Lin (1995) imposed temperature anomalies below the melting zone and then combined the effects of crustal-thickness and mantle-density variations to yield theoretical isostatic bathymetric variations and ΔMBA.

Applying this method for ranges of imposed temperature anomalies and model spreading rates, we derive the empirical relations:

$$\Delta T = (0.11U + 35.3)\Delta RB, \tag{4}$$
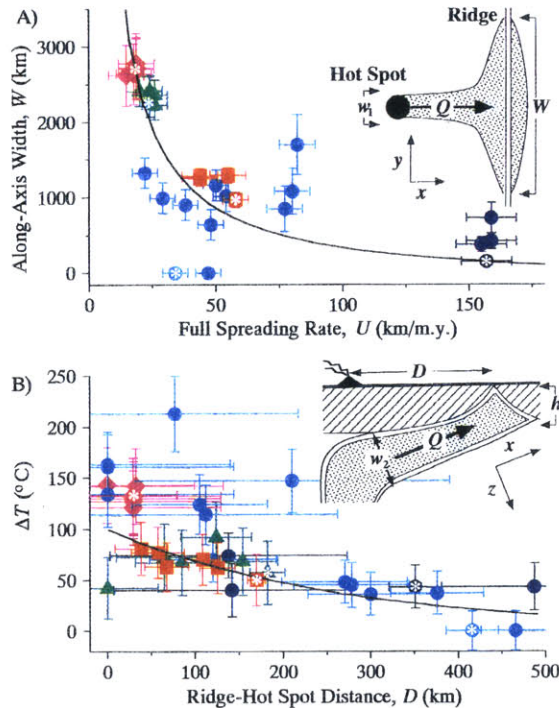
Figure 4. A: Along-isochron widths of residual bathymetric anomalies vs. full spreading rates during times corresponding to isochron ages. Diamonds—Iceland, triangles—Azores, squares—Galápagos, light blue circles—Tristan, dark blue circles—Easter. Asterisks mark present-day ridge-axis anomalies. Present-day spreading rates are from DeMets et al. (1990); paleorates are from Cande and Kent (1992), Mayes et al. (1990), Srivastava and Tapscott (1986), and Wilson and Hey (1995). Note that Iceland, Azores, Galápagos, and Easter plot in tight groupings, each defining narrow range in W (≤ 600 km) and U (≤ 20 km/m.y.). Tristan anomalies encompass wider range in W, reflecting secondary dependence on D (best fitting line is $W = 1690 - 3.3D$; root-mean-square misfit is 250 km). Solid curve is relation derived in text. Inset illustrates map view of plume-ridge flow pattern; dot pattern marks plume material. **B:** Along-isochron temperature anomalies (derived from method of Ito and Lin, 1995) plotted against D. Solid curve is predicted by conductive cooling. Inset illustrates depth cross section of plume conduit between hotspot and ridge axis.

and

$$\Delta T = -(0.0017U + 0.45)\Delta MBA. \tag{5}$$

The dependence of ΔT on U reflects a subtle dependence of crustal thickness on spreading rate that is consistent with calculations of Su et al. (1994). For $\Delta T = 100$ °C and $U = 20$–100 km/m.y., for example, we predict corresponding values of crustal thickening of 9–4.5 km.

Temperature anomalies derived accordingly from the observed ΔRB and ΔMBA are maximum for the on-ridge cases (150–225 °C), and decrease to near zero for $D \sim 500$ km (Fig. 4B). Such a behavior can be interpreted as the cooling trend of plume material as it migrates from hotspot centers to nearby ridges, the ridge-centered cases reflecting the temperature anomaly of the hotspot itself.

As plume material migrates from a hotspot center to a ridge, it conducts heat to the surrounding mantle (see Fig. 4, A and B, insets). Assuming that the amount of heat conducted in the direction of plume flow is negligible, the heat balance equation is

659

39

$$\rho c_p \frac{\partial T}{\partial x} V = -\left(\frac{\partial q_y}{\partial y} + \frac{\partial q_z}{\partial z}\right), \tag{6}$$

where T is the average temperature of the plume conduit, ρ and c_p are the density and heat capacity of the plume material, respectively, and q_y and q_z are the components of conductive heat flow out of the conduit walls. If we assume that heat loss occurs through a thermal boundary layer surrounding the plume channel with thickness δ,

$$q_z \sim q_y \sim \frac{k\Delta T}{\delta}, \tag{7}$$

where k is the mantle thermal conductivity ($3\ \text{W}\cdot\text{m}^{-1}\cdot{}^{\circ}\text{C}^{-1}$) and δ is defined such that $q = 30\text{--}100\ \text{mW/m}^3$, comparable to heat-flux values on the sea floor. If it is assumed that the gradients $\partial q_y/\partial y$ and $\partial q_z/\partial z$ are proportional to $1/w_1$ and $1/w_2$, respectively, and $Q \sim w_1 w_2 V$ (i.e., $V \gg U/4$), the combination of equations 6 and 7 yields

$$\frac{\partial T}{\partial x} = -\frac{2\kappa}{Q\delta}(w_1 + w_2)\Delta T, \tag{8}$$

where $\kappa = k/\rho c_p$ is thermal diffusivity ($10^{-6}\ \text{m}^2/\text{s}$). Integrating with respect to x from 0 to D yields

$$\Delta T = \Delta T_o \exp\left[-\frac{2\kappa}{Q\delta}(w_1 + w_2)D\right], \tag{9}$$

where ΔT_o is the temperature anomaly at the hotspot center.

Taking $\Delta T_o = 100\ {}^{\circ}\text{C}$, $(w_1 + w_2) = 400\ \text{km}$, and $Q = 2.2 \times 10^6\ \text{km}^3/\text{m.y.}$ as consistent with the observed W vs. U trend above, we produce a theoretical curve (Fig. 4B) that effectively matches the inferred temperature anomalies for $D > 50$ km. For $D \leq 100$ km, the Iceland and Tristan points lie significantly higher than the theoretical curve. This mismatch may be because (1) the Iceland and early Tristan plumes are hotter than the other hotspots and/or (2) latent heat loss due to melting at the hotspot centers rapidly cools the plume before it migrates to nearby ridges in the off-axis cases. For $D \sim 500$ km, ΔT is small enough that its effects on ΔRB and ΔMBA are negligible, even though the plume may still be feeding the ridge. Consequently, the geochemical signal may persist to a ridge-hotspot distance of up to 850 km (Schilling et al., 1985), long after the signals in ΔRB and ΔMBA have disappeared.

CONCLUSIONS

Along-isochron variations in residual bathymetry and mantle Bouguer gravity reflect the influence of hotspots on paleoaxes of nearby spreading centers. The amplitudes of along-isochron anomalies for the five prominent plume-ridge systems reach a maximum of 4.7 km for ΔRB and -340 mgal for ΔMBA and decrease with increasing paleoridge-hotspot distance. The along-isochron widths (0–2700 km), however, depend inversely on paleo–spreading rate. Whereas the widths of ΔRB reflect the balance between ridgeward plume flux and lithospheric accretion, the amplitudes of ΔRB and ΔMBA reflect paleoaxial temperature anomalies that decrease as the plume material cools along its lateral migration to nearby ridges. The five hotspots appear to deliver material to ridges with comparable fluxes of $\sim 2.2 \times 10^6\ \text{km}^3/\text{m.y.}$ and produce excess mantle temperature anomalies of 50 to 225 °C that influence ridge-axis structure to a maximum ridge-hotspot distance of ~ 500 km.

ACKNOWLEDGMENTS

REFERENCES CITED

Cande, S. C., and Kent, D. V., 1992, A new geomagnetic polarity time scale for the Late Cretaceous and Cenozoic: Journal of Geophysical Research, v. 97, p. 13,917–13,951.

Carlson, R. L., and Johnson, H. P., 1994, On modeling the thermal evolution of the oceanic upper mantle: An assessment of the cooling plate model: Journal of Geophysical Research, v. 99, p. 3201–3214.

DeMets, C., Gordon, R. G., Argus, D. F., and Stein, S., 1990, Current plate motions: Geophysical Journal International, v. 101, p. 425–478.

Feighner, M. A., Kellogg, L. H., and Travis, B. J., 1995, Numerical modeling of chemically buoyant mantle plumes at spreading ridges: Geophysical Research Letters, v. 22, p. 715–718.

Hamelin, B., Dupré, B., and Allègre, C. J., 1984, Lead-strontium isotopic variations along the East Pacific Rise and the Mid-Atlantic Ridge: A comparative study: Earth and Planetary Science Letters, v. 67, p. 340–350.

Hart, S. R., Schilling, J.-G., and Powell, J. L., 1973, Basalts from Iceland and along the Reykjanes Ridge: Sr isotope geochemistry: Nature, Physical Science, v. 246, p. 104–107.

Ito, G., and Lin, J., 1995, Mantle temperature anomalies along the present and paleoaxes of the Galápagos spreading center as inferred from gravity analyses: Journal of Geophysical Research, v. 100, p. 3733–3745.

Kuo, B.-Y., and Forsyth, D. W., 1988, Gravity anomalies of the ridge-transform system in the South Atlantic between 31 and 34.5 °S: Upwelling centers and variations in crustal thickness: Marine Geophysical Research, v. 10, p. 205–232.

Lin, J., and Phipps Morgan, J., 1992, The spreading rate dependence of three-dimensional mid-ocean ridge gravity structure: Geophysical Research Letters, v. 19, p. 13–16.

Lonsdale, P., 1988, Geography and history of the Louisville hotspot chain in the southwest Pacific: Journal of Geophysical Research, v. 93, p. 3078–3104.

Mayes, C. L., Lawver, L. A., and Sandwell, D. T., 1990, Tectonic history and new isochron chart of the South Pacific: Journal of Geophysical Research, v. 95, p. 8543–8567.

Morgan, W. J., 1978, Rodriguez, Darwin, Amsterdam, .., A second type of hot spot island: Journal of Geophysical Research, v. 83, p. 5355–5360.

Müller, R. D., Roest, W. R., Royer, J.-Y., Gahagan, L. M., and Sclater, J. G., 1993a, A digital age map of the ocean floor: Scripps Institution of Oceanography Reference Series 93-30.

Müller, R. D., Royer, J.-Y., and Lawver, L. A., 1993b, Revised plate motions relative to the hotspots from combined Atlantic and Indian Ocean hotspot tracks: Geology, v. 21, p. 275–278.

O'Connor, J. M., and Duncan, R. A., 1990, Evolution of the Walvis Ridge–Rio Grande Rise hot spot system: Implications for the African and South American plate motions over plumes: Journal of Geophysical Research, v. 95, p. 17,475–17,502.

Sandwell, D. T., and Smith, W. H., 1992, Global marine gravity from ERS-1, GEOSAT and SEASAT reveals new tectonic fabric [abs.]: Eos (Transactions, American Geophysical Union), v. 73, p. 133.

Schilling, J.-G., 1985, Upper mantle heterogeneities and dynamics: Nature, v. 314, p. 62–67.

Schilling, J.-G., 1986, Geochemical and isotopic variation along the Mid-Atlantic Ridge axis from 79°N to 0°N, in Vogt, P. R., and Tucholke, B. E., eds., The western North Atlantic region: Boulder, Colorado, Geological Society of America, Geology of North America, v. M, p. 137–156.

Schilling, J.-G., 1991, Fluxes and excess temperatures of mantle plumes inferred from their interaction with migrating mid-ocean ridges: Nature, v. 352, p. 397–403.

Schilling, J.-G., Thompson, G., Kingsley, R., and Humphris, S., 1985, Hotspot–migrating ridge interaction in the South Atlantic: Nature, v. 313, p. 187–191.

Srivastava, S. P., and Tapscott, C. R., 1986, Plate kinematics of the North Atlantic, in Vogt, P. R., and Tucholke, B. E., eds., The western North Atlantic region: Boulder, Colorado, Geological Society of America, Geology of North America, v. M, p. 379–404.

Su, W., Mutter, C. Z., Mutter, J. C., and Buck, W. R., 1994, Some theoretical predictions on the relationships among spreading rate, mantle temperature, and crustal thickness: Journal of Geophysical Research, v. 99, p. 3215–3227.

Vogt, P. R., 1976, Plumes, subaxial pipe flow, and topography along the mid-oceanic ridge: Earth and Planetary Science Letters, v. 29, p. 309–325.

Wilson, D. S., and Hey, R. N., 1995, History of rift propagation and magnetization intensity for the Cocos-Nazca spreading center: Journal of Geophysical Research (in press).

CHAPTER 3

DYNAMICS OF MANTLE FLOW AND MELTING AT A RIDGE-CENTERED HOTSPOT: ICELAND AND THE MID-ATLANTIC RIDGE

Dynamics of mantle flow and melting at a ridge-centered hotspot: Iceland and the Mid-Atlantic Ridge

Garrett Ito[a], Jian Lin[b], and Carl W. Gable[c]

[a]*MIT/WHOI Joint Program, Department of Geology and Geophysics, Woods Hole Oceanographic Institution, Woods Hole, MA, 02543*
508-289-2575 (tel), 508-457-2187 (fax), gito@magellan.whoi.edu

[b]*Department of Geology and Geophysics, Woods Hole Oceanographic Institution, Woods Hole, MA, 02543*
508-289-2576 (tel), 508-457-2187 (fax), jlin@whoi.edu

[c]*Earth and Environmental Sciences, Los Alamos National Laboratories, Los Alamos, NM, 87545*
505-665-3533 (tel), gable@lanl.gov

Abstract

We investigate the dynamics of mantle flow and melting of a ridge-centered plume with three-dimensional variable-viscosity numerical models, focusing on three buoyancy sources: temperature, melt depletion, and melt retention. The width W, to which a plume spreads along a ridge axis, depends on plume volume flux Q, full spreading rate U, buoyancy number B, and ambient/plume viscosity contrast γ. When all melting effects are considered, our numerical results are best parameterized by $W=2.37(Q/U)^{1/2}(B\gamma)^{0.04}$. Thermal buoyancy is first order in controlling along-axis plume spreading while latent heat loss due to melting, and depletion and retention buoyancy forces contribute second-order effects. We propose two end-member models for the Iceland plume beneath the Mid-Atlantic Ridge (MAR). The first has a broad plume source with temperature anomaly ΔT_p of 75°C, radius a of 300 km, and Q of 1.2×10^7 km^3/my. The second is of a narrower and hotter plume source with ΔT_p of 170°C, radius of 60 km, and Q of 2.1×10^6 km^3/my. The broad plume source predicts successfully the observed seismic crustal thickness, topographic, and gravity anomalies along the MAR, but predicts an along-axis geochemical plume width substantially broader than that suggested by the observed Sr^{87}/Sr^{86} anomaly. The narrow plume source model predicts successfully the total excess crustal production rate along the MAR (2.5×10^5 km^3/my) and a geochemical width consistent with that of the Sr^{87}/Sr^{86} anomaly, but it requires substantial along-axis melt transport to explain the observed along-axis variations in crustal thickness, bathymetry, and gravity. Calculations suggest that lateral plume dispersion may be radially symmetric rather than channeled along the ridge axis and that the topographic swell, which is elongated along the Reykjanes Ridge, may be due to rapid off-axis subsidence associated with lithospheric cooling

superimposed on a broader hotspot swell. The two plume source models predict seismic P-wave velocity reductions of 0.5-2% in the center of the plume, producing travel time delays of 0.2-1.2 s. Predicted P-wave delay-times for the narrow plume source model are more consistent with recent seismic observations beneath Iceland, suggesting that this model may be more representative of the Iceland plume.

---

1. Introduction

Centered on the Mid-Atlantic Ridge (MAR), the Iceland hotspot is the largest melt anomaly throughout the world's mid-ocean ridge system and is among the large oceanic igneous provinces [1]. The idea that Iceland marks a mantle convection plume rising beneath the MAR has become well established since its original conception in the early 1970's (e.g. ref. [2, 3, 4]). The broad topographic swell (Fig. 1) and correlated along-spreading-axis geochemical anomalies indicate that the plume rises beneath Iceland and spreads laterally along the ridge axis [4, 5]. Such along-axis spreading of a mantle plume feeding a ridge axis may also explain topographic and geochemical anomalies affected by other near ridge-axis hotspots (e.g. ref [6, 7, 8])—many of which may have contributed substantially to the earth's heat and magmatic budget throughout geologic history.

While the original concept that plumes feed and spread along nearby ridges was proposed two decades ago, only recently have the fluid dynamic aspects been investigated quantitatively. Recent numerical and laboratory tank experiments have shown that the width W, over which a plume spreads along axis, increases with plume volume flux Q, and decreases with plate full-spreading rate U [9, 10, 11]. Such studies are important in revealing the pertinent physical processes governing plume-ridge interactions and in placing theoretical constraints on properties of mantle plumes such as temperature anomaly, size, and volume flux.

Two potentially important sources of buoyancy, however, have not been considered in previous plume-ridge studies. These are melt depletion, which lowers the Fe/Mg ratio in the residual mantle and thus reduces its density [12], and melt retention in the mantle, which also reduces mantle bulk density (e.g. [13, 14, 15]). It has been proposed that melt depletion may be primary in driving spreading of intraplate plumes beneath the lithosphere [16]. It has also been proposed that both melt retention buoyancy and depletion buoyancy may contribute significantly to along-axis variations in mantle flow and crustal thickness beneath normal mid-ocean ridges [17, 18].

The objectives for this study are two fold. First we investigate numerically the effects of thermal- and melting-related buoyancy forces on along-axis spreading of ridge-centered plumes. We use three-dimensional (3D), variable viscosity, numerical models to simulate a buoyant plume rising beneath spreading plates and systematically test the effects of thermal, melt depletion, and melt retention buoyancy forces. Our second objective is to constrain the temperature anomaly, dimension, and volume flux of the Iceland plume by comparing theoretical predictions with observed variations in seismic crustal thickness, topography, gravity, and geochemistry on Iceland and along the Mid-Atlantic Ridge. We propose two end-member models for the mantle plume source beneath Iceland to explain the observations, and discuss their implications on basalt geochemistry, melt migration, and seismic velocity variations along the Mid-Atlantic Ridge axis.

2. Governing equations

To model mantle flow of a plume-ridge system in the upper-mantle, we treat the mantle as a fluid of zero Reynolds number and infinite Prandtl number. The 3D stress tensor, τ, is defined according to

$$\tau = 2\eta(T_R, p)\,\dot{\varepsilon} - pI \tag{1}$$

where I is the identity matrix and η is viscosity which depends on real temperature T_R and hydrostatic pressure p. The strain rate tensor $\dot{\varepsilon}$ depends on spatial derivatives of mantle flow rate u according to $\dot{\varepsilon} = 1/2(u_{i,j} + u_{j,i})$. The equilibrium equations include conservation of mass

$$\nabla \bullet u = 0, \tag{2}$$

momentum

$$\nabla \bullet \tau = -\Delta\rho(T, X, \phi)g\hat{z}, \tag{3}$$

and energy

$$\frac{\partial T}{\partial t} = \kappa\nabla^2 T - u \bullet \nabla T - \frac{T\Delta S}{c_p}\dot{M} \tag{4}$$

(see Table 1 for definition of variables). Eq. (2) satisfies the Boussinesq approximation and neglects dilational flow due to the extraction of melt which is likely to be small [19]. Eq. (3) balances viscous stresses with the body force due to density variations which depend on potential temperature T, melt depletion X, and mantle porosity ϕ, according to,

45

$$\Delta\rho = -\rho_o \left(\alpha T + \beta X + \frac{\rho_o - \rho_m}{\rho_o} \phi \right). \tag{5}$$

Eq. (4) balances energy transfer associated with heat conduction, heat advection, and latent heat loss due to melting. Melt depletion is governed by

$$\frac{\partial X}{\partial t} = -\boldsymbol{u} \bullet \nabla X + \dot{M} \tag{6}$$

where M is melt fraction and $\dot{M} = \dfrac{\partial M(p,T)}{\partial t}$.

To estimate the distribution of porosity ϕ, we assume that melt migrates vertically through the mantle at a melt-mantle velocity contrast $(\omega\text{-}w)$ as governed by Darcy's flow law,

$$\phi(\omega - w) = \frac{(\rho_o - \rho_m)gK}{\eta_m}. \tag{7}$$

Permeability K depends on grain size b according to $K = \dfrac{b^2\phi^2}{72\pi}$. Finally, the rate of melt percolation is assumed to be equivalent to the rate at which melt is generated such that

$$\phi(z)\omega(z) = \frac{\rho_o}{\rho_m} \int_D^z \dot{M}dz. \tag{8}$$

3. Numerical method and boundary conditions

To solve the above equations, we use a Cartesian numerical code presented by Gable [20, 21]. Time integration is achieved by iterating through discrete time steps, during each of which we solve for mantle flow, mantle potential temperature, and melt depletion. In solving the dimensionless forms of the flow equations (Eqs. 1-4), horizontal derivatives are expressed in terms of their Fourier components while vertical derivatives are expressed as finite difference approximations. We then invert for horizontal and vertical components of velocities and stresses using a standard relaxation method.

The dimensionless form of Eq. (3) is

$$\nabla \bullet \tau = \frac{\rho_o g D^3}{\kappa \eta_o}\left(\alpha T_o T + \beta X + \frac{\rho_o - \rho_m}{\rho_o}\phi \right),\qquad (9)$$

where primes denote dimensionless variables. The body force (right hand side of Eq. (9)) is the sum of three terms: the first term, which scales with T, is a Rayleigh number,

$Ra = \frac{\rho_o g D^3}{\kappa \eta_o}\alpha T_o$; the second term, which scales with X, is a melt depletion Rayleigh

number, $Ra_X = \frac{\rho_o g D^3}{\kappa \eta_o}\beta$; and the third term, which scales with ϕ, is a melt retention

Rayleigh number, $Ra_\phi = \frac{\rho_o g D^3}{\kappa \eta_o}\left(\frac{\rho_o - \rho_m}{\rho_o} \right)$. Assumed values for β and $\left(\frac{\rho_o - \rho_m}{\rho_o} \right)$ are

0.06 [12, 16] and 0.121 [14, 18], respectively. Consequently, depleting the mantle by 25% yields a density reduction equivalent to heating the mantle by 440°C, while a melt porosity of 3% yields a density reduction equivalent to heating the mantle by 107°C.

We assume that mantle viscosity varies with real temperature T_R and pressure according to

$$\eta = \eta_o \exp\left\{ \frac{E + pV}{RT_R} - \frac{E + \rho_o g(0.5D)V}{RT_{Ro}} \right\},\qquad (10)$$

where reference viscosity η_o is defined as the mantle viscosity for $T=T_o$ and $z=0.5D$; T_R in Kelvin is $(T + 0.6z + 273)$, where the term $0.6z$ takes into account the adiabatic gradient; and T_{Ro} is the real temperature value of T_o. To approximate numerically the effects of non-Newtonian rheology, we use reduced values of activation energy E and activation volume V [22] (Table 1). Because lateral variations in viscosity introduce nonlinearity to the above flow equations, we linearized the equations by introducing additional body force terms [20, 23]. The nonlinear terms and solutions were then updated upon successive iterations until solutions converged to our specified limit. We found that a convergence criterion of 0.1-0.5% yielded time-integrated solutions with errors of <0.5% while minimizing computing time. This computational method was tested in 2D with independent finite element solutions, while in 3D, it produced solutions within 2.6% of the best-estimated extrapolated solutions of a benchmark problem of ref. [24] .

47

The final velocity field is then used in the advection term in Eq. (4) to solve for a new temperature field. Our energy solver uses finite differences with a tensor diffusion scheme to reduce numerical diffusion which is intrinsic to finite difference methods [20, 21]. The same tensor diffusion method is used to solve Eq. (6) for the depletion field. Vertical flow determines the rate of decompression melting, comprising the source terms in Eqs. (4) and (6). The melting-rate term in Eq. (4) is latent heat loss, which inhibits buoyant mantle flow by increasing both mantle density and viscosity, while the melting-rate term in Eq. (6) generates low-density depleted mantle residuum. To calculate melting rate $\dot{M}$, we incorporate the solidus and liquidus functions of McKenzie and Bickle [25], as well as their functional dependence of M on homologous temperature for adiabatic batch melting.

The rate of melting also determines the volume fraction of melt retained in the mantle ϕ, which is the source of retention buoyancy. To compute porosity we combine Eqs. (7) and (8) and solve the integral in Eq. (8) numerically similar to ref. [18]. The grain-size-dependent melt permeability that we incorporate results in maximum porosities of 1-3% which is slightly higher than the 0.1-1% porosity range inferred from ^{238}U-^{230}Th-^{226}Ra disequilibria in Hawaiian lavas [26].

The numerical model setup is illustrated in Fig. 2. A ridge axis ($x=0$) is simulated by defining reflecting temperature (i.e., zero heat flux) and flow (i.e., zero shear stress) boundary conditions at the vertical sides, and setting the top boundary ($z=0$) to move at a constant half-spreading rate $0.5U$. Temperature at the surface ($z=0$) is maintained at $0°C$ which cools and thickens a high-viscosity lithosphere approximately with the square root of x. A plume is introduced by imposing a columnar-shaped temperature anomaly in the lower portion of the box, centered beneath the ridge axis. The plume is hottest ($T=T_o+\Delta T_p$) at its center and cools as a Gaussian function of radial distance to T_o at its radius a. We exploit the symmetry in x and y by centering the plume column at $x=y=0$, which allows a quarter plume in solution space to represent a fully circular plume in virtual space. In the lower portion of the box ($z > 0.6D$), we impose the potential temperature to be T_o everywhere except inside the plume source. Thus, the energy equation is solved only in the upper portion of the box ($0.6D \geq z \geq 0$).

To ensure numerical accuracy in the flow solutions, we set a non-dimensional viscosity (η/η_o) upper limit of 200 and set a lower limit of 0.1. The upper viscosity limit is sufficient to accurately simulate a rigid lithosphere (i.e., $u=U$ and $v=w=0$ in the lithosphere), while the lower limit allows us to incorporate the full viscosity reduction in a plume with temperature anomaly of $200°C$. The depth dependence of viscosity yields a

factor of ~4 viscosity increase between top and bottom of the box for a constant mantle temperature.

4. Steady-state along-axis width of a mantle plume head

We seek here to quantify the effects of melting on mantle flow and thus the dependence of along-axis plume width W on plume flux Q and plate spreading rate U. We began numerical experiments with the steady-state temperature solution of a ridge without the plume. Then after activating the plume, we integrated through time until both along-axis plume width and plume flux converged to steady-state values. We ran four sets of experiments: experimental set A (Table 2a) includes only thermal buoyancy and omits all melting effects; set B (Table 2b) considers only thermal buoyancy but includes latent heat loss; set C (Table 2c) includes additional buoyancy from melt depletion; and set D (Table 2d) includes additional buoyancy from melt retention.

Fig. 2 shows an example steady-state velocity and temperature field for a calculation in set A with a plume source temperature anomaly of 200°C (model 5a). Velocity vectors illustrate the plume rising from the conduit source and then spreading both perpendicular to and along the ridge axis after it impinges on the base of the lithosphere. Combined effects of thermal buoyancy and reduced plume viscosity result in a maximum plume upwelling rate of 244 km/my, which is >20 times that of the half spreading rate of 10 km/my. The corresponding average upwelling rate in the melting zone ($z \leq 110$ km) is 85 km/my.

Fig. 3a shows the steady-state velocity and mantle density fields for the same plume source temperature anomaly but with the additional effects of latent heat loss (model 5b). In the melting region of the plume center, potential temperatures are ~130°C cooler and consequently the plume is 65% less buoyant and 3 times more viscous than the calculation without latent heat loss (Fig. 2). The resulting average upwelling rate in the melting zone is 50 km/my, only ~60% of the predicted average upwelling rate of the model without latent heat loss (model 5a).

The addition of melt depletion buoyancy in model 5c generates an additional ~1% lateral density contrast between the plume center and the mantle beneath normal ridge sections far from the plume (Fig. 3b). The resulting average melting-zone upwelling rate is 67 km/my. As material rises more rapidly in the plume center, it spreads more rapidly along the base of the rigid lithosphere. This in turn inhibits upwelling at radial distances of 100-150 km shown as negative velocity differences in Fig 3b.

Finally, model 5d considers the additional buoyancy from melt retention (Fig. 3c). The high melting rate in the plume center results in a maximum porosity of 2.5%, to reduce bulk density in the plume center by an additional 0.3%. This added retention buoyancy further enhances the average upwelling rate in the melting zone to 77 km/my, which is ~90% of that predicted by the model that neglects all melting effects (model 5a). Thus, the added melting-related buoyancy forces approximately balance the upwelling-inhibiting effects of latent heat loss.

In all models examined we find, as did Ribe et al. [11], that the thickening lithosphere does not channel the plume preferentially along the ridge axis. On the contrary, the spreading lithosphere enhances ridge-perpendicular flow by pulling plume material away from the ridge-axis, and actually impedes along-axis flow by viscous shear. These effects however are small—the total along-axis flux at $y=70$ km is within a few percent of the total ridge-perpendicular flux at $x=70$ km. Thus, the rate of spreading away from the plume center is approximately equal in all radial directions.

To determine how W depends on Q and U for each experimental set, we examine spreading rates between 20 and 120 km/my and we vary Q by changing ΔT_p between 100°C and 200°C (Table 2). We track the distribution of plume material by introducing a tracer P in the plume and using our tensor diffusion scheme to advect P passively with the mantle. $P=1$ is introduced in the plume source column to represent 100% plume material, while $P=0$ represents 0% plume material and 100% ambient mantle. We define W as the

along-axis extent to which the depth-integrated tracer concentration $\left(\dfrac{1}{0.6D} \displaystyle\int_0^{0.6D} P(0,y,z)dz \right)$

is >0.05 (Fig. 2). The volume flux of the plume is measured at $z=0.6D$ by integrating the vertical flow of the plume source over its cross-sectional area.

For calculations that include thermal buoyancy only without latent heat loss (set A), we find, similar to ref. [9, 11], that W depends primarily on the scaling quantity $(Q/U)^{1/2}$, and

depends secondarily on the plume buoyancy number, $\left(B = \dfrac{Q\rho_o \alpha \Delta T_p}{48\eta_o U^2} \right)$ as defined in ref.

[11], and on the ambient/plume viscosity ratio $\gamma = \eta_o/\eta_p$, at $z=0.5D$. A modified buoyancy number which depends on plume viscosity is thus $(B\gamma)$. The best fit linear regression function obtained by fitting linear and constant coefficients to $\ln(B\gamma)$ is

$$W = 2.35\left(\frac{Q}{U}\right)^{1/2}(B\gamma)^{0.04}.$$ (11)

Calculated values of $W(Q/U)^{-1/2}$ range from 2.2 to 2.9 (Table 2) with a mean value of 2.50. To compare our results directly with those of Ribe et al. [11], we omit the dependence on γ and incorporate their definition of Q which is the integrated vertical plume flux weighted by plume temperature anomaly. With these modifications we obtain a best-fit linear regression of $W=2.80(Q/U)^{1/2}B^{0.05}$ which is in good agreement with that of Ribe et al. [11] of $W=2.93(Q/U)^{1/2}B^{0.052}$. While the scaling and exponential factors vary slightly between our results and those of ref. [9] and [11], the general form of Eq. (11) is robust and insensitive to differences in far-field experimental boundary conditions.

For calculations of thermal buoyancy with latent heat loss (set B), we obtain a best-fit linear regression function,

$$W = 2.21\left(\frac{Q}{U}\right)^{1/2}(B\gamma)^{0.02}.$$ (12)

The smaller constant and exponential coefficients relative to those in Eq. (11) reflect the inhibiting effects of latent heat on along-axis plume spreading. The average values of $W(Q/U)^{-1/2}$ for experimental set B is 2.29, or ~92% of the average in set A.

Addition of depletion buoyancy in experimental set C results in a best-fit regression function,

$$W = 2.37\left(\frac{Q}{U}\right)^{1/2}(B\gamma)^{0.04}$$ (13)

This function is essentially the same as that of Eq. (11) for set A. The average value of $W(Q/U)^{-1/2}$ of 2.51 is also essentially the same as that in set A. The further addition of melt retention (set D) does not change this relationship significantly as shown by the similarity in regression lines of set C and set D (Fig. 4). Thus, the effects of retention buoyancy occurs at wavelengths too short to affect the full width W. In summary, the effects of latent heat loss to inhibit lateral plume spreading are approximately balanced by the added buoyancy of melt depletion which enhances plume spreading.

5. Models of Iceland and the Mid-Atlantic Ridge

We next investigate models of mantle flow and melting beneath Iceland, a relatively well studied example of a ridge-centered plume. Our objective is to constrain the temperature

anomaly, dimension, and volume flux of the Iceland plume by comparing theoretical model predictions with observed along-axis variations in seismic crustal thickness, topography, gravity, and basalt geochemistry. Previous geophysical studies of the Iceland-MAR system demonstrated that the topographic high at Iceland coincides with a low in mantle-Bouguer gravity anomaly (MBA), and that both MBA and topographic anomalies can be explained by the combined effects of anomalously thick crust and low density mantle generated by the Iceland plume [27, 28]. MBA are calculated by subtracting from free-air gravity the attraction of seafloor topography and the crust-mantle interface assuming a uniform crustal thickness of 7 km (e.g., [29, 30]). Because as much as 75% of the along-axis topographic and MBA variations may arise from thickened igneous crust [28, 31], crustal thickness calculations are an important link between our models and surface observations.

To predict crustal thickness from mantle melting calculations, we assume that all melt generated within 200 km of the ridge axis accretes perpendicularly to the ridge axis and take the top of our numerical box to be the isostatic depth of the seafloor for crust of normal thickness (7 km). The crustal thickness as a function of along-axis coordinate y is therefore

$$Cr(y) = \frac{2}{U}\left(\frac{\rho_o}{\rho_m}\right)\int \dot{M}(y)dxdz. \qquad (14)$$

We take the top of our model to be the isostatic depth of the seafloor for a 7-km-thick model crust, and assume isostatic compensation of crustal thickness variations that deviate from this model crust. Consequently, variations in crustal thickness impart no lithostatic pressure variations in the mantle. To prevent melting at depths shallower than the isostatic base of the thickened Icelandic crust we prohibit melting everywhere at depths <28 km. Melting may stop deeper, however, if hydrothermal cooling is important [32].

To calculate isostatic topography of the seafloor, we consider contributions from both the crust (Δh_c) and mantle (Δh_m). In calculating Δh_c, we assume Airy compensation of the crust with a surface density contrast of (ρ_c-ρ_w) for the submarine portion of topography and ρ_c for the subaerial portion. The crust along the Reykjanes and Kolbeinsey Ridges is assumed to have a density of 2800 kg/m^3 except within 500 km of the plume center, where we increase it linearly to a maximum of 3030 kg/m^3 at Iceland, to account for the higher

MgO content of the Icelandic crust [33]. The mantle contribution to topography, or dynamic topography is calculated from vertical normal stress at the top layer of our model,

$$\Delta h_m = \frac{\tau_{zz}}{(\rho_o - \rho_w)g}.$$ (15)

With this definition, our calculations predict seafloor depths to increase approximately with the square-root of distance from the ridge-axis which is consistent with lithospheric half space cooling models (e.g. [34]). In addition to using Δh_m to predict topography, we also use Δh_m to estimate crustal thickness in a manner independent of our mantle melting calculations. This "isostatic crustal thickness" is defined as the isostatic thickness of crust required to account for the difference between the observed topography and Δh_m.

In computing MBA we again consider both crustal and mantle contributions. The crustal contribution is the gravitational signal due to undulations at the crust-mantle interface that deviate from the constant crustal thickness reference model originally assumed in generating MBA. For these calculations we employ the method of ref. [35]. The mantle contribution to gravity is calculated by integrating the contributions from lateral density variations at each model layer [29].

5.1 Broad plume source model

Our first model of the Iceland-MAR system, much like that of Ribe et al. [11], considers a broad plume source with a relatively small temperature anomaly (model Ice 1, a=300 km, and ΔT_p=75°C) rising beneath a model MAR with a full-spreading rate of 19 km/my [36] (Fig. 5a). At this spreading rate, T_0=1350°C is required to produce a ~7 km-thick, normal oceanic crust. The calculation that includes all melting effects (model Ice 1d) predicts a plume volume flux of ~1.2×10^7 km^3/my, generating an along-axis plume-head width W of ~2300 km (Fig.5a). The predicted maximum upwelling rate in model Ice 1d is 105 km/my, which is >10 times that beneath the unaffected portion of the ridge far from the plume. The predicted upwelling rate averaged through the melting zone in plume center is 20 km/my. Melt retention buoyancy contributes minimal effects to this average upwelling rate and thus very little to melting rate.

The enhanced upwelling rate in the plume center, combined with an increase in total melt extent (23% compared to 13% beneath the ridge far away from the plume), generates a maximum crustal thickness of ~30 km, consistent with the seismic measurements on Iceland [37] (Fig. 5b). Along the length of the Reykjanes Ridge, the crustal thickness

53

profiles predicted by melting in model Ice 1d shows striking similarity to the seismic measurements. From the plume center, the predicted crust first thins to 9.5 km at an along-axis distance of ~300 km, then thickens to 11 km at a distance of ~500 km, and finally tapers to a thickness of 6.7 km at a distance of ~1300 km. The predicted local minimum in crustal thickness at y~300 km is caused by a reduced mantle upwelling rate at the plume edge caused by the rapid vertical flux in the plume center. Melt retention does not significantly affect crustal thickness because the predicted 0.5% contrast in porosity between the plume center and normal sub-ridge mantle is too small to appreciably enhance plume upwelling rate in the shallowest 100 km, where melting occurs. The isostatic crustal thickness profile of model Ice 1d also shows good agreement with the observed crustal thickness profile (Fig. 5b). The excess magmatic flux rate required to sustain the anomalous (in excess of a 7-km-thick crust) isostatic crust along the MAR, 1000 km north and south of Iceland, is 2.33×10^5 km^3/my. This value is within a few percent of the 2.45×10^5 km^3/my excess crustal production rate predicted from our melting model.

The predicted topography from the melting-model crustal profile generates 70% (~2.5 km) of the total along-axis topographic anomaly of ~3.5 km (Fig. 5c). We predict the remaining 30% (~1 km) of topography to be supported by dynamic mantle uplift which is obtained with a β value of 0.024 [12, 17]. Of mantle dynamic topography Δh_m, thermal buoyancy generates ~70% while depletion and retention buoyancy generate the remaining 22 and 8%, respectively. The predicted total amplitude of Δh_m is consistent with the 0.5-1.5 km of Eocene uplift as inferred from sediment core analyses [38].

The mantle-Bouguer anomaly along the submarine portions of the ridge is also matched well by predictions of model Ice 1d using both the melting-model and isostatic crust (Fig. 5d). Similar to bathymetry, the crustal MBA accounts for most (70%) of the total predicted anomaly of ~330 mGal with the mantle contributing the remaining 30%. Of the predicted mantle gravity signal, 75% is from thermal expansion, while 20 and 5% are generated by melt depletion and retention, respectively. The successful predictions of both topography and MBA support the hypothesis that these anomalies are from the same sources: primarily crustal thickness variations and secondarily density variations in the shallow mantle.

5.2 Narrow plume source model

Our second set of models (Ice 2) represent another end-member possibility—that of a narrower and hotter plume source (Fig. 6a; a=60 km, and ΔT_p=170°C). With all melting effects included, model Ice 2d predicts a plume volume flux of 2.1×10^6 km^3/my which

spreads plume material to a full width W of 870 km along the ridge axis. The maximum upwelling rate of model Ice 2d is 283 km/my, which is >2.5 times greater than the maximum upwelling rate in the broad plume source (model Ice 1d), and ~30 time faster than normal ridge upwelling rates. In addition, the maximum extent of melting is increased to 30%. Thus a larger volume of mantle material is predicted to circulate more rapidly through a thicker melting zone relative to that of Ice 1d, which results in melting rates an order of magnitude greater than those in model Ice 1d (Fig. 6a). For the model without melt retention (model Ice 2c), the melting-zone averaged upwelling rate is 63 km/my and the maximum melting-model crustal thickness is 147 km. With melt retention (model Ice 2d), the 2.9% porosity in the plume is sufficient to increase the predicted melting-zone-averaged upwelling rate to 80 km/my and the maximum melting-model crustal thickness to 166 km (Fig 6b). In model Ice 2d, the melting-model crust thins to 3 km at an along-axis distance of 120 km, where upwelling and thus melting rate is strongly reduced at the edge of the rapidly upwelling plume center (Fig. 6a).

The high maximum crustal thicknesses predicted by the narrow plume source, melting model drastically exceed calculations of previous studies that assumed passive mantle upwelling (e.g. ref. [28, 39]) and drastically exceed the observed crustal thicknesses (Fig 6b). The resulting topographic and MBA anomalies also fail to match the observations (Fig. 6c, d). The isostatic crustal profile, on the other hand, yields predictions in much better agreement with the observed crustal thicknesses (Fig 6b), topography (by definition) (Fig. 6c), and MBA (Fig. 6d) along the ridge axis. Thus, if the Iceland plume is comparable in radius and temperature to our narrow plume source model, a substantial portion of the melt produced beneath Iceland must accrete more uniformly along-axis than our melting-model crust, much like our isostatic crustal profile. This condition suggests melt migration and/or lower crustal ductile flow [40] occurs over distances of several hundreds of kilometers away from Iceland along the Reykjanes and Kolbeinsey Ridges.

Because the mechanisms of along ridge-axis melt transport are poorly understood, we do not attempt to model this process in this study. Instead, we assume a priori that along-axis melt redistribution does occur and that the end result of this process leads to the isostatic crustal profile. In arriving at our final Ice 2 models, we thus sought values of ΔT_p and a such that the total volume rate of melt produced by the melting model matched that required to sustain the isostatic crustal profile. The best solutions of ΔT_p=170°C and a=60 km yield a total excess melt production rate of 2.54×10^5 km^3/my (model Ice 2d), which is within 1% of that required of the isostatic crustal profile.

In these narrower, hotter plume source models, the mantle contribution to topography and gravity relative to the crustal contribution becomes much larger than in the broader, cooler source models. For example, model Ice 2d predicts a mantle topographic uplift that is 51% (1.8 km) of the observed along-axis topographic anomaly (Fig. 6c), and a mantle contribution to MBA that is 48% (158 mGal) of the observed MBA variation (Fig. 6d). The crust therefore generates only 49 and 52% of the total topographic and MBA variations, respectively. Calculations also predict the importance of melt-related buoyancy to the mantle anomalies to be significantly greater for these hotter plume source models relative to the cooler source models. Thermal buoyancy is predicted to produce 47% of Δh_m, and 60% of the mantle MBA variation; melt depletion produces 39% of Δh_m and 25% of the mantle MBA; and melt retention produces the remaining 14% of Δh_m and 15% of the mantle MBA variation.

5.3 Reykjanes Ridge bathymetric swell

Similar to along-axis topography, we predict map view topography by adding mantle dynamic topography (Eq. (15)) and isostatic topography of the crust considering only along-axis variations in crustal thickness. For model Ice 1d, we use the melting-model crust and for model Ice 2d, we use the isostatic crust. Fig. 7 illustrates the observed topography in map view along the Reykjanes Ridge south of Iceland, and predictions of models Ice 1d and Ice 2d. The similarity between the predictions and observations at broad wavelengths (>~500 km) are compelling: both models predict the ~2.0 km across-axis decrease in broad wavelength topography between Iceland and an across-axis distance of 400 km away from the ridge-axis, and both predict the south-pointing swell, elongated along the Reykjanes Ridge. As demonstrated above, the southward deepening of the ridge axis reflects crustal thinning and mantle density increase with distance from the Iceland plume source. But perpendicular to the ridge-axis, seafloor topography is dominated by the subsidence of the cooling lithosphere. Thus, contrary to previous notions (e.g. [5, 6]), the regional bathymetric swell does not require a pipe-like flow of plume material along the ridge axis. Instead, we predict the plume head to spread radially and explain the general shape of the elongated Icelandic swell as the superposition of radial plume spreading and across-axis lithospheric cooling. The models presented in this study, however, do not consider time-dependent variations in crustal accretion which may also contribute to across-axis topographic variations.

5.4 Rare-earth element and isotopic anomalies

A potentially useful independent constraint on melting depth and extents, which reflect mantle temperature, is rare-earth element (REE) concentrations of axial basalts. A simple comparison can be made with previous inversions of melt fraction versus depth as calculated by White et al. [33]. At the plume center, our broad plume source model (Ice 1d) and narrow plume source model (Ice 2d) predict melt fractions that are lower and higher, respectively, than White et al.'s [33] inversions for Krafla volcano on Iceland (Fig. 8a). The potential temperature of the Iceland plume-source, therefore, is likely to be 1425-1520°C as represented by our two end-member models. At ~550 km from Iceland on the Reykjanes Ridge, model Ice 1d predicts melting depths and extents closely matching those obtained from the REE inversions [33] (Fig. 8b). Model Ice 2d, however, underpredicts the extents and depths because plume material from our narrow plume source did not spread to this along-axis distance. Thus, in order to explain the REE composition of basalts sampled 550 km away from Iceland, once again our model Ice 2d seems to require plume-derived melts to migrate substantially along the Reykjanes Ridge axis.

While REE concentrations reflect melting process beneath Iceland, Sr isotope ratios may reflect the concentration of the plume source material relative to that of normal mid-ocean ridge basalts (MORB). Schilling [8, 41] interprets the peak in $^{87}Sr/^{86}Sr$ at Iceland to mark the center of the Iceland plume, where the plume source concentration is highest, and interprets the decrease in $^{87}Sr/^{86}Sr$ north and south of Iceland to reflect a decrease in percent of plume material comprising the mantle melt source.

To address questions of where and how plume–MORB mixing occurs, we calculate the fraction of plume tracer P in accumulated melts along the model ridge axis (neglecting along-axis melt migration) (Fig 8c). At each numerical grid where new melt is generated, P is weighted by melting rate. We then integrated over each ridge-perpendicular plane to compute a weighted mean value ($\overline{P}$) for each point along the ridge axis,

$$\overline{P}(y) = \frac{\int P(x,y,z)\dot{M}(x,y,z)\mathrm{d}x\mathrm{d}z}{\int \dot{M}(x,y,z)\mathrm{d}x\mathrm{d}z}. \qquad (16)$$

This calculation thus approximates the plume concentration of pooled melts along the ridge axis. For example, $\overline{P}=1.0$ indicates that all of the melt generated in a plane perpendicular to that point of the ridge is entirely plume-source derived. Likewise, $\overline{P}=0.0$ indicates that none of the melts are plume derived and $0.0<\overline{P}<1.0$ indicates plume-MORB mixing.

Model Ice 1d predicts an along-axis geochemical plume width of >2000 km, significantly greater than that suggested by the $^{87}Sr/^{86}Sr$ anomaly. Ice 2d on the other hand predicts a width of ~1000 km which is more consistent with that of the $^{87}Sr/^{86}Sr$ anomaly; however, its profile in $\bar{P}$ would likely be broader if along-axis melt migration were considered. Both model Ice 1d and Ice 2d predict that the melts are entirely plume derived ($\bar{P}$=1.0) over most of the plume width, and become fully ambient mantle derived ($\bar{P}$=0.0) within 200-300 km of the edge of the plume. These results suggest that within most of the plume affected portion of the ridge, very little mixing occurs between plume and ambient source material in the shallow mantle. Thus, if the gradients in $^{87}Sr/^{86}Sr$ away from Iceland reflect plume-MORB mixing, it most likely occurs deeper in the mantle, possibly by ambient mantle entrainment of the ascending plume (e.g. [42]).

5.5 Predictions of P-wave seismic velocity anomalies

Observations of compressional wave (P-wave) seismic travel time variations and associated mantle P-wave velocity variations provide critical constraints on mantle properties beneath Iceland. To predict P-wave seismic velocity anomalies, we assume a reference P-wave velocity of 8 km/s, which decreases by $6.25 \times 10^{-3}\%$ for each 1°C increase in mantle temperature, increases by 0.1% for each 1% increase in depletion, and decreases by 1.25% for each 1% increase in pore volume [43]. We also predict P-wave travel-time residuals by calculating travel times of seismic rays passing vertically through the 400 km thickness of our mantle models.

The broad plume source model (Ice 1d) predicts a maximum decrease in P-wave velocity below the melting region of ~0.5% relative to the surrounding mantle. In the melting region, the predicted P-wave velocity anomaly diminishes because the velocity-enhancing effects of latent heat loss and melt depletion exceed the velocity-reducing effect of melt retention (Fig. 9a). The corresponding travel-time delay for vertically passing rays is predicted to be +0.23 s at the plume center and decrease to zero at an along-axis distance of ~1200 km. The contributions to travel-time delay above the plume center are +0.25 s from excess mantle temperature, -0.09 s from melt depletion, and +0.07 s from melt retention. Across the ridge-axis, lithospheric cooling dominates, resulting in a predicted travel-time difference of 0.5 s between the plume center and at an across-axis distance of 400 km. The broad plume source model thus predicts only a gradual decrease in travel-time delay across the ridge axis and even smaller variations along the ridge axis.

58

In contrast, the narrow plume source of model Ice 2d predicts significantly larger amplitudes of P-wave anomalies over a much narrower lateral extent. Below the melting zone, the 170°C plume temperature anomaly reduces calculated P-wave velocities by more than 1%. In the melt zone, however, the P-wave velocities are reduced to as much as 2% due to the 2.9% melt retention (Fig. 9b). Along the ridge axis, the travel-time delay for vertically passing rays is predicted to be +0.75 s at the plume center and to decrease by 0.85 s within ~80 km. Approximately half of this travel-time residual is predicted to arise in the high-porosity melt zone in the shallow mantle. Across the ridge axis, the additional effect of lithospheric cooling yields a predicted travel-time difference of 1 s within ~80 km of the plume center and a travel-time difference of 1.2 s over an across-axis distance of 400 km. Preliminary results of the ongoing ICEMELT experiment at Iceland have revealed azimuthal variations in P-wave travel times as high as 1 s within 100 km of the ridge axis [44], suggesting that the narrow plume source model better represents Iceland than does the broad plume source model.

6. Discussion

6.1 Importance of melting effects

The importance of melting effects on mantle flow, melt production, and surface observables are summarized in Fig. 10. Mantle melting generates appreciable effects on mantle properties; however, over the range of plume viscosities considered in our models, the effect of latent heat loss on mantle flow largely cancels the effects of depletion and retention buoyancy. As a result, the combined effects of these factors on mantle flow are small as reflected in the small changes in the predicted values of $W(Q/U)^{-1/2}$ (Figs. 4 and 10). Similarly, when plume temperature anomalies are mild as in the Ice 1 models, the melting-related factors have only second order effects on upwelling rate as reflected in small changes in the predicted crustal thickness (Fig. 10). When plume temperature anomalies are larger, however, as in the Ice 2 models, melt retention may enhance the predicted crustal thickness by 20% relative to calculations that do not include retention.

Contrasting with their mild influence on mantle flow, the melting-related factors have substantial effects on the predicted geophysical observables and these effects increase with increasing plume temperature (Fig. 10). For mantle contributions to topography and MBA, latent heat loss reduces the amplitudes of predicted anomalies by 20-40% relative to calculations without latent heat loss. Depletion buoyancy increases predicted mantle topographic anomalies and MBA by 10-65% relative to calculations without depletion,

while retention buoyancy increases predicted anomalies by 5-25% relative to calculations without retention. Melting effects on P-wave delay-time are also important: Latent heat loss decreases predicted delay-time by ~13%, melt depletion decreases delay-time by 20-30%, but melt retention increases delay-time by 20-60%. It is thus important to consider melting effects on mantle properties when predicting geophysical observables.

6.2 Model uncertanties

Because melting-related factors do not affect significantly large-scale mantle flow, uncertainties associated with our melt calculations such as the assumed batch melting [25], our choice of β values, and the melt porosity calculations, are likely to have only secondary effect on our estimates of plume source radius and temperature. By far the most important uncertainty in this regard is mantle rheology. The reference mantle viscosity η_0 controls directly the rate of mantle upwelling in response to density variations (Eq. (9)). But unfortunately, viscosity beneath ridges is not known to within one or even two orders of magnitude (e.g. [45]). One mechanism that may yield a substantially higher viscosity than that we have assumed is dehydration at the onset of melting [45]. A higher melting zone viscosity, for example, would most likely require a greater temperature anomaly of the broad plume source model to explain the geophysical observations, or require a greater source radius and less along-axis melt redistribution of our narrow plume source model to explain the observations. Thus, because of the uncertainty of viscosity, our Iceland plume models are not unique. However, they do provide reasonable bounds on the plume source radius and temperature given the similarities between model predictions and the variety of geophysical and geochemical observations considered.

6.3 Plume volume flux estimates

Still, it may be possible to constraint plume volume flux independent of ambient viscosity based on the observed MBA and bathymetric anomaly widths and the theoretical relationship between flux and W (i.e. Eq. (13)). The use of Eq. (13) to infer plume volume flux is valid if the surface anomaly widths reflects directly the along-axis plume width in the mantle, which would be the case if along-axis melt migration is negligible as assumed in the Ice 1 models. The flux required to match the along-axis MBA and bathymetric anomaly widths as predicted from model Ice 1d is 1.2×10^7 km^3/my. This flux, however, is several times larger than previous estimates of the Iceland plume of 2×10^6 km/my [46], 1.43×10^6 km/my [8], and 2.2×10^6 km/my [28]. If on the other hand,

along-axis melt migration is important as suggested for the Ice 2 models, we can not use Eq. (13) to constrain the Iceland plume volume flux independent of η_0. We must therefore rely on the fact that our melt production rate estimates are consistent with the total volume of observed excess crust as we did for the Ice 2 models. Indeed, model Ice 2d predicts a plume volume flux of 2.1×10^6 km^3/my which is more consistent with the above estimates of the previous studies. An intriguing new question arising from this narrow plume source model is, what specific mechanisms may allow melt generated beneath Iceland to migrate hundreds of kilometers along-axis? Possible evidence for such melt transport may include the V-shaped axial bathymetric highs propagating away from Iceland along the Reykjanes Ridge as first noted by Vogt [47] in 1971.

7. Conclusions

We have investigated the dynamics of mantle flow and melting of a ridge-centered plume using three-dimensional, variable-viscosity models with focus on three buoyancy sources: temperature, melt depletion, and melt retention. When all melting effects are considered, the relationship between along-axis plume width W, plume volume flux Q, full spreading rate U, buoyancy number B, and ambient/plume viscosity ratio γ, is best parameterized by $W=2.37(Q/U)^{1/2}(B\gamma)^{0.04}$. Calculations that include melting yield a similar relationship to those that do not include melting because of the competing effects of latent heat loss and depletion buoyancy. We propose two end-member models for the Iceland plume beneath the MAR. The broad plume source of radius=300 km represents a low temperature (ΔT_p=75°C) and high flux (Q=1.2x10^7 km^3/my) end-member, while the narrow plume source of radius=60 km represents a high temperature (ΔT_p=170°C) and low flux (Q=2.1x10^6 km^3/my) end-member. The broad plume source predicts successfully the observed along-axis variations in seismic crustal thickness, topography, and mantle-Bouguer gravity anomalies; whereas the narrow source model predicts adequately the total excess crustal production rate (2.5x10^5 km^3/my) but requires extensive melt migration and/or lower crustal ductile flow to occur over hundreds of kilometers along the MAR in order to explain the geophysical and geochemical observations. Our calculations predict that plume spreading away from the plume center is radially symmetric rather than channeled preferentially along the ridge axis. The elongated bathymetric swell along the Reykjanes Ridge can be explained by rapid off-axis subsidence due to lithospheric cooling superimposed on a broader hotspot swell. Both the broad and narrow plume source models predict very little mixing between the plume and MORB sources in

the shallow mantle; hence, we suggest that mixing may occur deeper in the mantle possibly due to entrainment of the isotopically depleted portion of the mantle by the rising mantle plume. Our narrow plume source model predicts seismic P-wave velocity variations more consistent with recent seismic observations beneath Iceland, suggesting that this model may better represent the Iceland plume.

Acknowledgments

References

1 M.F. Coffin and O. Eldholm, Large igneous provinces: Crustal structure, dimensions, and external consequences, Rev. Geophys., 32, 1-36, 1994.

2 W.J. Morgan, Convection plumes in the lower mantle, Nature, 230, 42-43, 1971.

3 P.R. Vogt, Evidence for global synchronism in mantle plume convection, and possible significance for geology, Nature, 240, 338-342, 1972.

4 J.-G. Schilling, Iceland mantle plume: Geochemical study of Reykjanes Ridge, Nature, 242, 565-571, 1973.

5 P.R. Vogt, Plumes, subaxial pipe flow, and topography along the mid-ocean ridge, Earth Planet. Sci. Lett., 29, 309-325, 1976.

6 J.-G. Schilling, Upper mantle heterogeneities and dynamics, Nature, 314, 62-67, 1985.

7 J.-G. Schilling, G. Thompson, R. Kingsley and S. Humphris, Hotspot-migrating ridge interaction in the South Atlantic, Nature, 313, 187-191, 1985.

8 J.-G. Schilling, Fluxes and excess temperatures of mantle plumes inferred from their interaction with migrating mid-ocean ridges, Nature, 352, 397-403, 1991.

9 M.A. Feighner and M.A. Richards, The fluid dynamics of plume-ridge and plume-plate interactions: an experimental investigation, Earth Planet. Sci. Lett., 129, 171-182, 1995.

10 M.A. Feighner, L.H. Kellogg and B.J. Travis, Numerical modeling of chemically buoyant mantle plumes at spreading ridges, Geophys. Res. Lett., 22, 715-718, 1995.

11 N. Ribe, U.R. Christensen and J. Theissing, The dynamics of plume-ridge interaction, 1: Ridge-centered plumes, Earth Planet. Sci. Lett., 134, 155-168, 1995.

12 E.R. Oxburgh and E.M. Parmentier, Compositional and density stratification in oceanic lithosphere—causes and consequences, Geol. Soc. Lond., 133, 343-355, 1977.

13 J.L. Ahern and D.L. Turcotte, Magma migration beneath an ocean ridge, Earth Planet. Sci. Lett., 45, 115-122, 1979.

14 J. Phipps Morgan, Melt migration beneath mid-ocean spreading centers, Geophys. Res. Lett., 14, 1238-1241, 1987.

15 D.R. Scott and D.J. Stevenson, A self-consistent model for melting, magma migration and buoyancy-driven circulation beneath mid-ocean ridges, J. Geophys. Res., 94, 2973-2988, 1989.

16 J. Phipps Morgan, W.J. Morgan and E. Price, Hotspot melting generates both hotspot volcanism and a hotspot swell?, J. Geophys. Res., 100, 8045-8062, 1995.

17 D.W. Sparks, E.M. Parmentier and J. Phipps Morgan, Three-dimensional mantle convection beneath a segmented spreading center: Implications for along-axis variations in crustal thickness and gravity, J. Geophys. Res., 98, 21,977-21,995, 1993.

18 K. Jha, E.M. Parmentier and J. Phipps Morgan, The role of mantle depletion and melt-retention buoyancy in spreading-center segmentation, Earth Planet. Sci. Lett., 125, 221-234, 1994.

19 D.L. Turcotte and J. Phipps Morgan, The Physics of magma migration and mantle flow beneath a mid-ocean ridge, in: Mantle Flow and Melt Generation Beneath Mid-Ocean Ridges, J. Phipps Morgan, D. K. Blackman and J. M. Sinton, ed., pp. 155-182, AGU, Washington, D.C., 1992.

20 C.W. Gable, Numerical models of plate tectonics and mantle convection in three dimensions, Ph.D. thesis, Harvard University, Cambridge MA, 1989.

21 C.W. Gable, R.J. O'Connel and B.J. Travis, Convection in three dimensions with surface plates: Generation of toroidal flow, J. Geophys. Res., 96, 8391-8405, 1991.

22 U. Christensen, Convection with pressure- and temperature-dependent non-Newtonian rheology, Geophys. J. R. Astr. Soc, 77, 343-384, 1984.

23 U. Christensen and H. Harder, 3-D convection with variable viscosity, Geophys. J. Int., 104, 213-226, 1991.

24 F. Busse, U. Christensen, R. Clever et al., 3D convection at infinite Prandtl number in Cartesian geometry- A benchmark comparison, Geophys. Astrophys. Fluid Dynamics, 75, 39-59, 1993.

25 D. McKenzie and M.J. Bickle, The volume and composition of melt generated by extension of the lithosphere, J. Petrol., 29, 625-679, 1988.

26 K.W.W. Sims and D.J. DePaolo, Porosity of the melting zone beneath Hawaii and mid-ocean ridges: Inferences from ^{238}U-^{230}Th-^{226}Ra disequilibria, in: Sixth V. M. Goldschmidt Conference, Heidelberg Germany, 1996.

27 G. Ito, J. Lin and R.S. Detrick, The effects of near-ridge hot spots on mid-ocean ridge density and temperature structure from analysis of gravity and bathymetry: Results from the Galapagos, Azores, and Iceland, EOS Trans. Amer. Geophys. Union., Spring Meeting Suppl., 75, 335, 1994.

28 G. Ito and J. Lin, Oceanic spreading center-hotspot interactions: Constraints from along-isochron bathymetric and gravity anomalies, Geology, 23, 657-660, 1995.

29 B.-Y. Kuo and D.W. Forsyth, Gravity anomalies of the ridge-transform system in the South Atlantic between 31° and 34.5°S: Upwelling centers and variations in crustal thickness, Mar. Geophys. Res., 10, 205-232, 1988.

30 J. Lin, G.M. Purdy, H. Schouten J.-C. Sempéré and C. Zervas, Evidence from gravity data for focused magmatic accretion along the Mid-Atlantic Ridge, Nature, 344, 627-632, 1990.

31 G. Ito and J. Lin, Mantle temperature anomalies along the present and paleoaxes of the Galápagos Spreading Center as inferred from gravity analyses, J. Geophys. Res., 100, 3733-3745, 1995.

32 W. Menke and D. Sparks, Crustal accretion model for Iceland predicts 'cold' crust, Geophys. Res. Lett., 22, 1673-1676, 1995.

33 R.S. White, J.W. Bown and J.R. Smallwood, The temperature of the Iceland plume and origin of outward propagating V-shaped ridges, J. Geol. Soc. Lond., 152, 1039-1045, 1995.

34 B. Parsons and J.G. Sclater, An analysis of the variation of ocean floor bathymetry and heat flow with age, J. Geophys. Res., 82, 803-827, 1977.

35 R.L. Parker, The rapid calculation of potential anomalies, Geophys. J. R. astr. Soc., 31, 447-455, 1973.

36 C. DeMets, R.G. Gordon, D.F. Argus and S. Stein, Effect of recent revisions to the geomagnetic reversal time scale on estimates of current plate motions, Geophys. Res. Lett., 21, 2191-2194, 1994.

37 J.R. Smallwood, R.S. White and T.A. Minshull, Sea-floor spreading in the presence of the Iceland plume: the structure of the Reykjanes Ridge at 61°40'N, J. Geol. Soc. Lond., 152, 1023-1029, 1995.

38 P.D. Clift, J. Turner and ODP Leg 152 Scientific Party, Dynamic support by the Iceland plume and its effect on the subsidence of the northern Atlantic margins, J. Geol. Soc. Lond., 152, 935-942, 1995.

39 D. McKenzie, The generation and compaction of partially molten rock, J. Petrol., 25, 713-765, 1984.

40 W.R. Buck, Along-axis crustal flow and ridge topographic segmentation, EOS Trans. of Amer. Geophys. Union, Spring Meeting Suppl., 77, 276, 1996.

41 J.-G. Schilling, Geochemical and isotopic variation along the Mid-Atlantic Ridge axis from 79°N to 0°N, in: The Geology of North America, P. R. Vogt and B. E. Tucholke, ed., pp. 137-156, GSA, 1986.

42 E.H. Hauri, J.A. Whitehead and S.R. Hart, Fluid dynamics and geochemical aspects of entrainment in mantle plumes, J. Geophys. Res., 99, 24,275-24,300, 1994.

43 E.D. Humphreys and K.G. Dueker, Physical state of the western U.S. upper mantle, J. Geophys. Res., 99, 9635-9650, 1994.

44 I.T. Bjarnason, C.J. Wolfe and S.C. Solomon, Initial results from the ICEMELT experiment: Body-wave delay times and shear-wave splitting across Iceland, Geophys. Res. Lett., 23, 459-462, 1996.

45 G. Hirth and D.L. Kohlstedt, Water in the oceanic upper mantle: Implications for rheology, melt extraction, and the evolution of the lithosphere, Earth Planet. Sci. Lett., in press, 1996.

46 N.H. Sleep, Hotspots and mantle plumes: Some phenomenology, J. Geophys. Res., 95, 6715-6736, 1990.

47 P.R. Vogt, Asthenosphere motion recorded by the by the ocean floor south of Iceland, Earth Planet. Sci. Lett., 13, 153-160, 1971.

48 P. Wessel and W.H.F. Smith, New version of the Generic Mapping Tools released, EOS Trans. Amer. Geophys. U., 76, 329, 1995.

49 M. Spiegelman, Geochemical consequences of melt transport in 2-D: The sensitivity of trace elements to mantle dynamics, Earth Planet. Sci. Lett., 139, 115-132, 1996.

Table 1. Notation

Variable	Meaning	Value	Units
a	plume radius		km
b	grain size	3×10^{-4}	m
B	buoyancy number		
c_p	specific heat	1000	J kg^{-1} °C^{-1}
D	fluid depth	400	km
E	activation energy	1.9×10^5	J
g	acceleration of gravity	9.8	m/s
Δh_c	isostatic crustal topography		km
Δh_m	mantle dynamic topography		km
K	mantle permeability		m^2
M	melt fraction		wt%
p	pressure		Pa
P	plume tracer concentration		
Q	volumetric plume flux		km^3/my
R	gas constant	8.314	J K^{-1} mol^{-1}
Ra	thermal Rayleigh number		
Ra_x	depletion Rayleigh number		
Ra_ϕ	retention Rayleigh number		
ΔS	entropy change on melting	400	J kg^{-1} °C
T	mantle potential temperature		°C
T_R	mantle real temperature		K
ΔT_p	plume temperature anomaly		°C
$u\ (u,v,w)$	mantle flow rate vector		km/my
U	ridge full spreading rate		km/my
V	activation volume	4×10^{-6}	m^3
W	along-axis plume width		km
X	melt depletion		wt%
α	coefficient of thermal expansion	3.4×10^{-5}	K^{-1}
β	coefficient of depletion density reduction		
γ	η_o/η_p		
κ	thermal diffusivity	31	km^2/my
η	viscosity		Pa s
η_o	reference viscosity		Pa s
η_p	plume viscosity at $0.5D$		Pa s
η_m	melt viscosity	1.0	Pa s
ω	vertical melt flow rate		km/my
ρ	mantle density		kg/m^3
ρ_c	crust density	2800-3030	kg/m^3
ρ_m	melt density	2900	kg/m^3
ρ_o	mantle reference density	3300	kg/m^3
ρ_w	water density	1000	kg/m^3

Table 2a. Parameters and results of experimental set A: thermal buoyancy without latent heat loss

Model	grid size, dx-dy (km)	U (km/my)	ΔT_p	B	γ	Q (10^6 km^3/my)	W	$W(Q/U)^{-1/2}$
1a	12.5–12.5	20	100	1.729	2.352	0.974	512	2.322
2a	12.5–6.25	120	100	0.0522	2.352	1.059	219	2.328
3a	12.5–6.25	60	100	0.195	2.352	0.987	281	2.193
4a	12.5–6.25	40	100	0.460	2.352	1.038	362	2.251
5a	12.5–12.5	20	200	6.977	5.054	1.965	938	2.991
6a	12.5–6.25	120	200	0.244	5.054	2.478	331	2.305
7a	12.5–6.25	60	200	0.746	5.054	1.892	419	2.358
8a	12.5-12.5	50	200	1.468	5.054	2.585	662	2.914
Ice 1a	12.5-12.5	19	75	36.553	1.849	12.39	2312	2.864
Ice 2a	10.0-10.0	19	170	14.866	3.757	2.186	830	2.447

For all experiments vertical grid separation dz is 8 km.

Models 1-8: β=0.06, ΔT=1300°C, η_0=1x10^{20} Pa s, Ra=0.915 x 10^6, $Ra\chi$=1.35 x 10^6, Ra_ϕ=2.75 x 10^6, a=70 km.

Models Ice 1-2: β=0.024, ΔT=1350°C, η_0=5x10^{19}Pa s, Ra=1.90 x 10^6, $Ra\chi$=1.12 x 10^6, Ra_ϕ=5.70 x 10^6.

Model Ice 1: a=300 km, ΔT_p=75°C.

Model Ice 2: a=60 km, ΔT_p=170°C.

Table 2b. Parameters and results of experimental set B: thermal buoyancy with latent heat loss

Model	grid size, dx-dy (km)	U (km/my)	ΔT_p	B	γ	Q (10^6 km^3/my)	W	$W(Q/U)^{-1/2}$
1b	12.5-12.5	20	100	1.720	2.352	0.969	488	2.215
2b	12.5-6.25	120	100	0.0463	2.352	0.939	206	2.331
3b	12.5-6.25	60	100	0.166	2.352	0.843	256	2.162
4b	12.5-12.5	40	100	0.389	2.352	0.876	312	2.111
5b	12.5-12.5	20	200	7.001	5.054	1.972	838	2.667
6b	12.5-6.25	120	200	0.203	5.054	2.059	281	2.147
7b	12.5-6.25	60	200	0.750	5.054	1.901	369	2.072
8b	12.5-12.5	50	200	1.193	5.054	2.100	462	2.257
Ice 1b	12.5-12.5	19	75	34.774	1.849	11.79	2212	2.809
Ice 2b	10.0-10.0	19	170	14.857	3.757	2.185	710	2.094

Table 2c. Parameters and results of experimental set C: thermal + depletion buoyancy with latent heat loss

Model	grid size, dx-dy (km)	U (km/my)	ΔT_p	B	γ	Q (10^6 km^3/my)	W	$W(Q/U)^{-1/2}$
1c	12.5-12.5	20	100	1.427	2.352	0.804	488	2.431
2c	12.5-6.25	120	100	0.0452	2.352	0.917	206	2.360
3c	12.5-6.25	60	100	0.164	2.352	0.834	256	2.173
4c	12.5-12.5	40	100	0.385	2.352	0.868	338	2.291
5c	12.5-12.5	20	200	6.788	5.054	1.912	988	3.194
6c	12.5-6.25	120	200	0.188	5.054	1.902	281	2.234
7c	12.5-6.25	60	200	0.724	5.054	1.835	406	2.323
8c	12.5-12.5	50	200	1.159	5.054	2.040	538	2.661
Ice 1c	12.5-12.5	19	75	34.117	1.849	11.56	2288	2.932
Ice 2c	10.0-10.0	19	170	14.597	3.757	2.147	830	2.469

Table 2d. Parameters and results of experimental set D: thermal + depletion + retention buoyancy with latent heat loss

Model	grid size, dx-dy (km)	U (km/my)	ΔT_p	B	γ	Q (10^6 km^{3}my)	W	$W(Q/U)^{-1/2}$
1d	12.5-12.5	20	100	1.433	2.352	0.808	488	2.426
2d	12.5-6.25	120	100	0.0452	2.352	0.917	206	2.359
3d	12.5-6.25	60	100	0.1648	2.352	0.836	256	2.171
4d	12.5-12.5	40	100	0.358	2.352	0.868	338	2.292
5d	12.5-12.5	20	200	6.764	5.054	1.905	913	2.956
6d	12.5-6.25	120	200	0.193	5.054	1.961	281	2.200
7d	12.5-6.25	60	200	0.718	5.054	1.820	419	2.404
8d	12.5-12.5	50	200	1.139	5.054	2.005	563	2.809
Ice 1d	12.5-12.5	19	75	34.089	1.849	11.56	2288	2.933
Ice 2d	10.0-10.0	19	170	14.501	3.757	2.133	870	2.597

Fig. 1. Combined shipboard and Etopo5 bathymetry map (contour interval of 0.5 km) showing Iceland (65°N, 18°W) and the Reykjanes (south of Iceland) and Kolbeinsey (north of Iceland) Ridges. Bold lines marks the ridge axes. This figure and Figs. 4, 7, 8, and 10 were produced using the GMT software package [48].
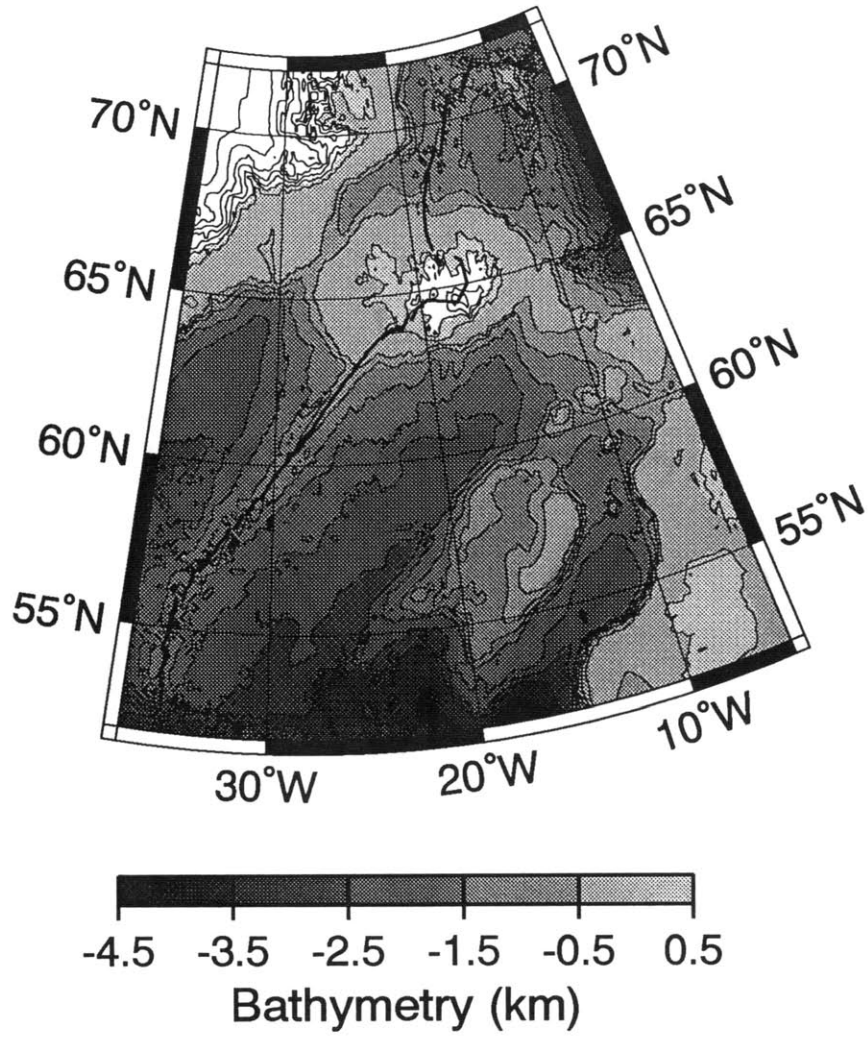
Bathymetry (km)

Figure 1

Fig. 2. Perspective diagram illustrating steady-state flow (small arrows) and potential temperature (shaded and contoured at 100°C-intervals) fields of an example calculation that considers thermal buoyancy only and no melting effects (model 5a). Vertical plane on the right is a depth cross-section along the ridge axis (x=0), while the vertical plane to the left is a depth cross-section perpendicular to the ridge axis (y=0). Top plot shows depth-averaged plume tracer concentration P along the ridge axis which we used to define plume width W. Both top (z=0) and bottom (z=D) boundaries are isothermal planes with the bottom, a free slip boundary and the top, fixed at a horizontal velocity of $0.5U$ (large horizontal arrow). All boundaries are closed to flow both in and out of the numerical box, thus material flows downward at the end of the box opposite the ridge (x=800 km) and recirculates toward the ridge axis along the base of the box. The effect of this recirculation on the interaction between plume and ridge are insignificant.
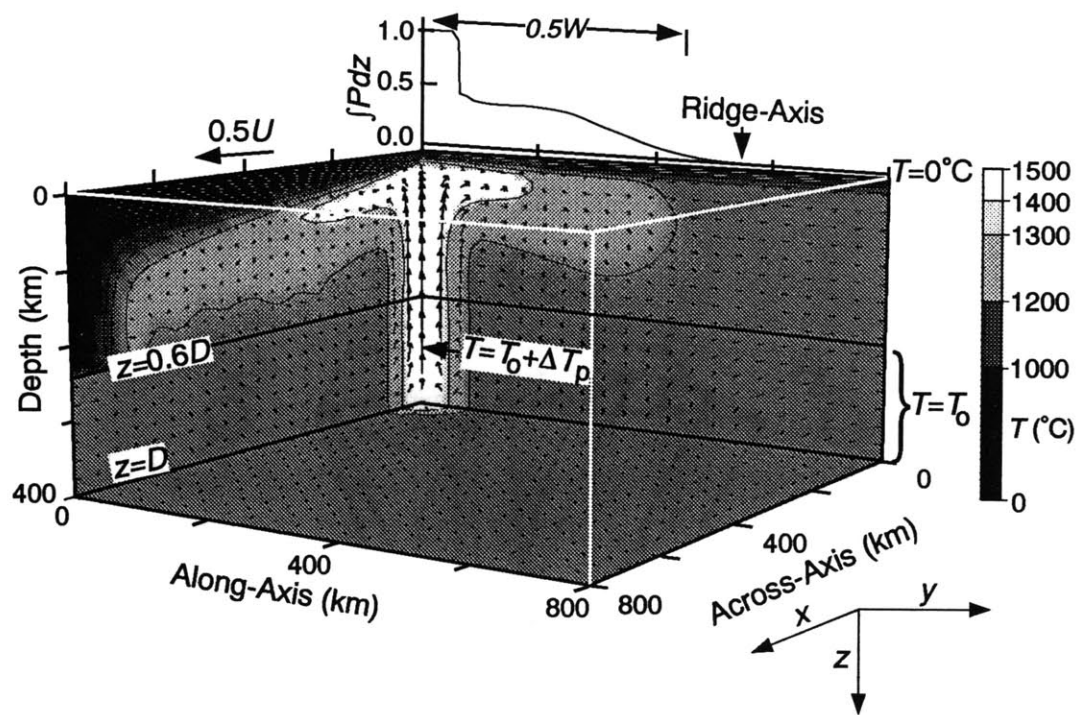
Figure 2

Fig. 3. Perspective views of depth cross-sections showing % density reduction in the mantle due to (a) thermal buoyancy with latent heat loss (ΔT_p=200°C) (model 5b), (b) plus melt depletion buoyancy (model 5c), and (c) plus melt retention buoyancy (model 5d). Contour interval is 0.5%. Vectors in (a) show mantle flow. Vectors in (b) show the differences between flows with and without melt depletion buoyancy. Vectors in (c) show the difference between flows with and without melt retention buoyancy. Downward pointing vectors in (b) and (c) illustrate reduced upwelling, not downwelling.

a) 0.5U   Ridge Axis

w_{max} = 244 km/my

b) Depth (km)

Δw_{max} = 27.5 km/my

% Density Reduction

c)

Δw_{max} =16.5 km/my

Along-Axis (km)   Across-Axis (km)

Figure 3

75
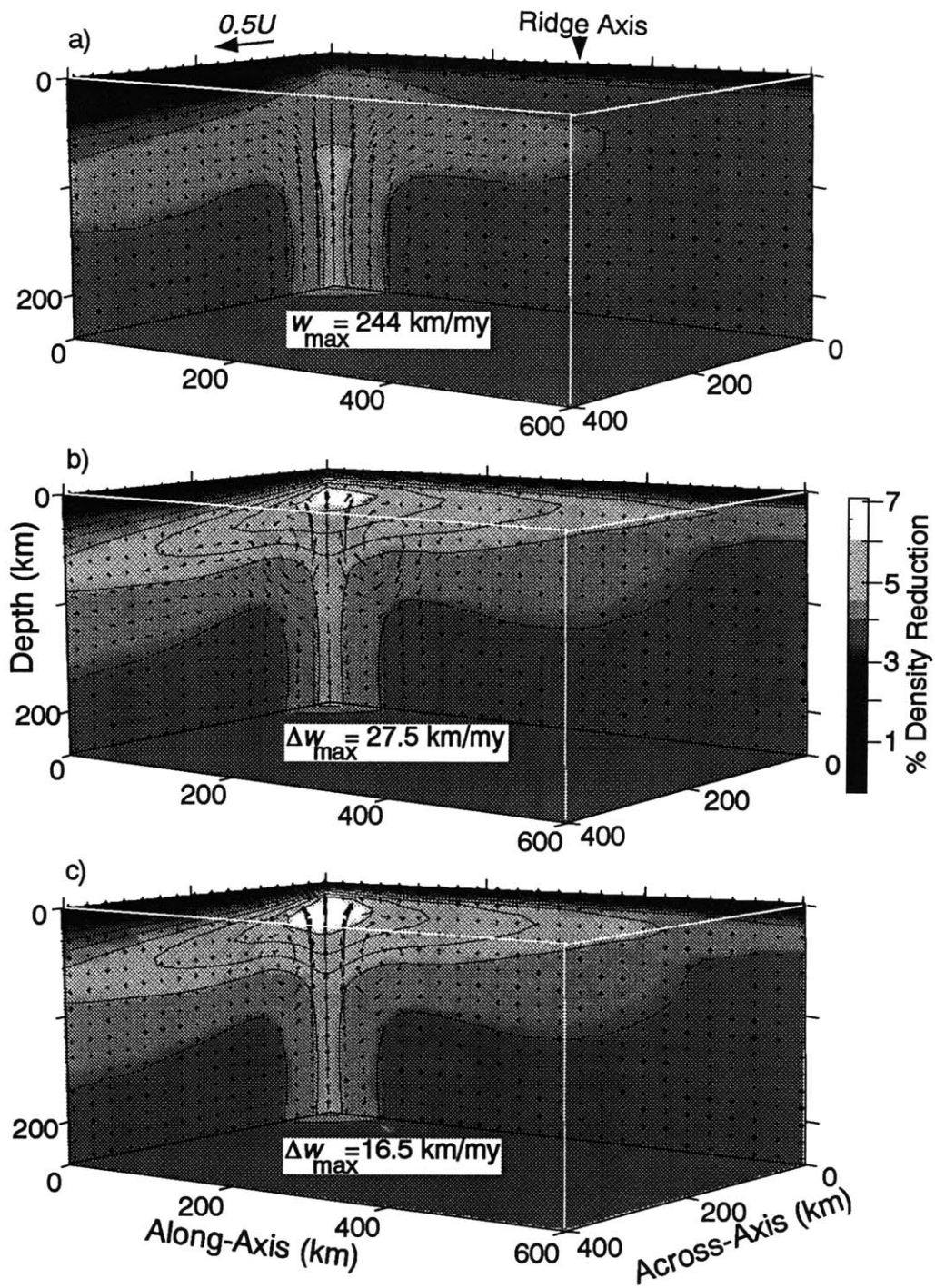
Fig. 4. Numerical results (dots) of calculations with all melting effects included (set D). The two Iceland models are circled. The solid black line is the best-fit linear regression shown by Eq. (13) which yields a standard deviation misfit that is 7% of the median value of $W(Q/U)^{-1/2}$. Also shown are corresponding linear regressions of calculations of thermal buoyancy without latent heat loss (set A, gray), thermal buoyancy with latent heat loss (set B, dotted), and additional buoyancy from melt depletion (set C, dashed).

Figure 4

Fig. 5. (a) Perspective diagram of model Ice 1d (broad plume source) shaded according to temperature. Black contours are depletion (contour interval is 5%) and white contours are melting rates of 0.01, 0.03, and 0.05 my^{-1}.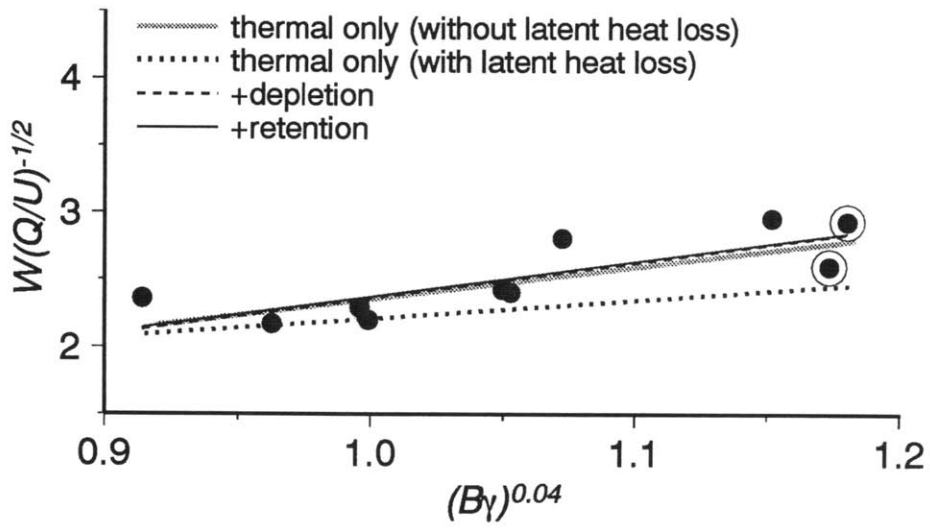 (b) Comparison between model Ice 1d melting-model crust (solid) and isostatic crust (dashed), and seismic crustal thickness measurements along the Reykjanes Ridge (dots) and at older seafloor near the continental margins (triangles) from ref. [37]. (c and d) Comparison between the observed bathymetry (thick gray curve in c) and MBA (thick gray curve in d) along the MAR and predicted profiles of model Ice 1d using the melting-model crust (bold curves in c and d) and isostatic crust (thick dashed curved in d). Also shown are predicted mantle components due to various mantle density sources as labeled. Bathymetry data and MBA are from ref [28]. We do not consider on-land gravity of Iceland.

Figure 5

79
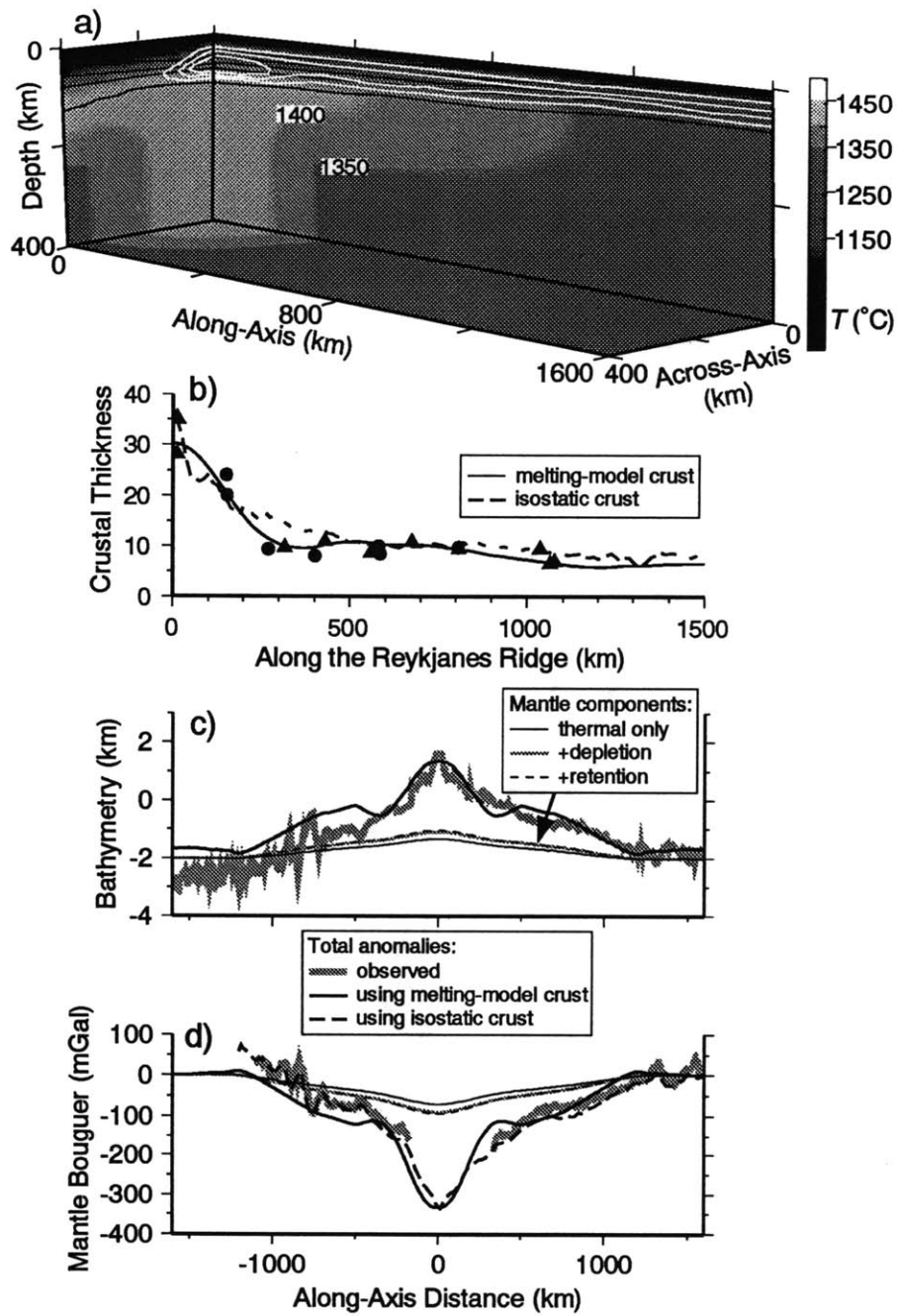
Fig. 6. Same as Fig. 5 but for Ice 2 models (narrow plume source). Symbols are the same as in Fig. 5 except melting rate contours in (a) are 0.01, 0.03, 0.05, 0.2, 0.4 my^{-1}.

Figure 6

81
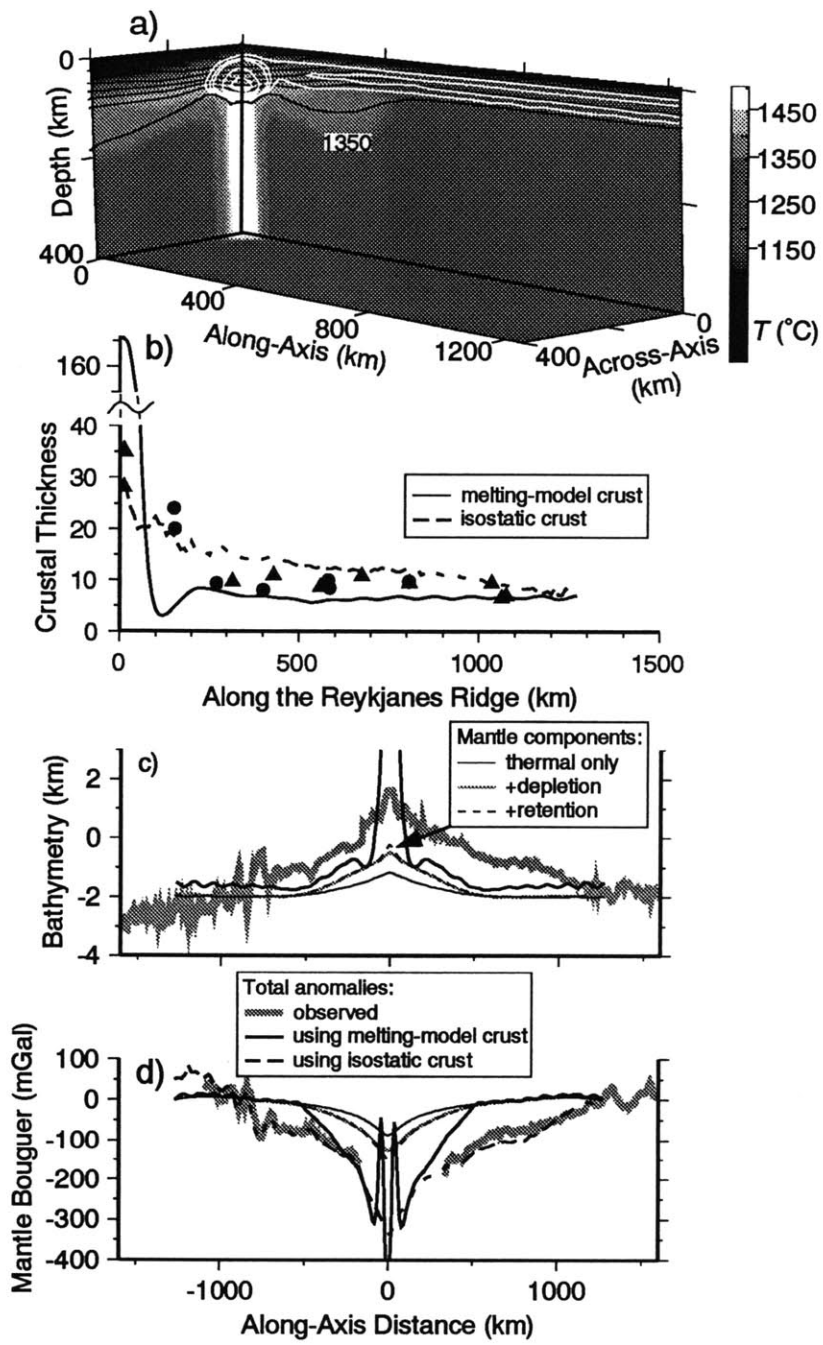
Fig. 7. (a) Observed topography of Iceland and the Reykjanes Ridge (oblique Mercator projection). (b) Mantle + crustal topography predicted from our broad plume source model Ice 1d using the melting-model crust. (c) Mantle + crustal topography predicted from our narrow plume source model Ice 2d using the isostatic crust.

a) Observed Topography   b) Model Ice 1d   c) Model Ice 2d

Across-Axis (km)

Depth (km)
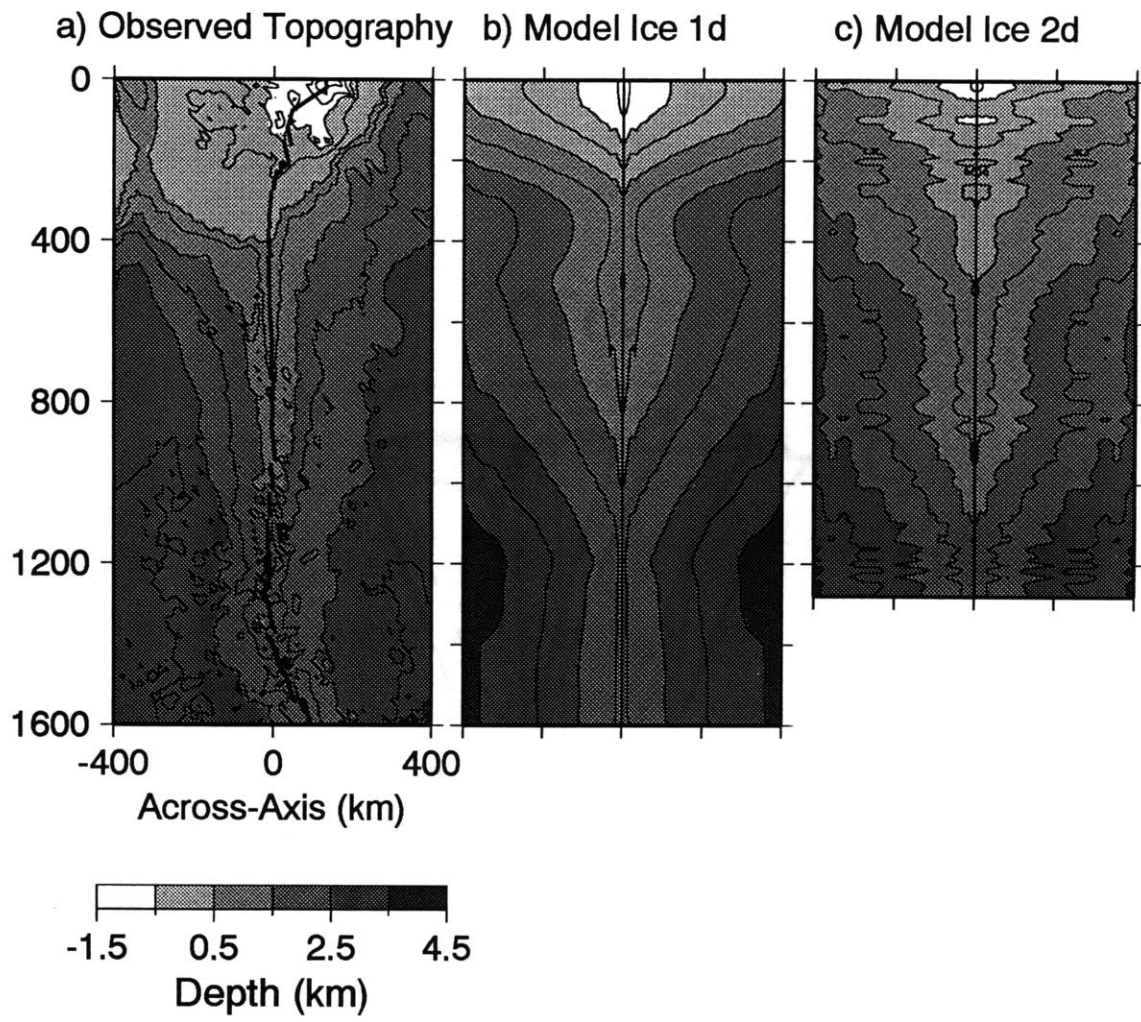
Figure 7

Fig. 8. (a and b) Comparison between White et al.'s [33] REE inversion of melt fraction (gray) and our predictions from models Ice 1d (solid) and Ice 2d (dashed) at Krafla, near the plume center (a), and at DSDP Site 409 on the Reykjanes Ridge 550 km away from the plume center (b). This inversion method assumes fractional melting and includes differences in partitioning coefficients between the spinel and garnet stability fields. It also assumes complete extraction and mixing of all melts generated in the melting region, which makes the estimation of maximum depth of melting sensitive to the low-degree melt compositions [49]. Another assumption is the parent source composition (primitive mantle beneath Krafla and a 50-50% mix of primitive and depleted MORB source along the Reykjanes Ridge), which is important in estimating the maximum extent of melting. (c) Comparison between observed Sr isotope concentrations [41] along Iceland and the MAR and weighted mean plume tracer concentration $\overline{P}$ in the accumulated melts for models Ice 1d (solid) and Ice 2d (dashed). The peak in $^{87}Sr/^{86}Sr$ to the north of Iceland is due to the Jan Mayen hotspot [41] which we do not model.
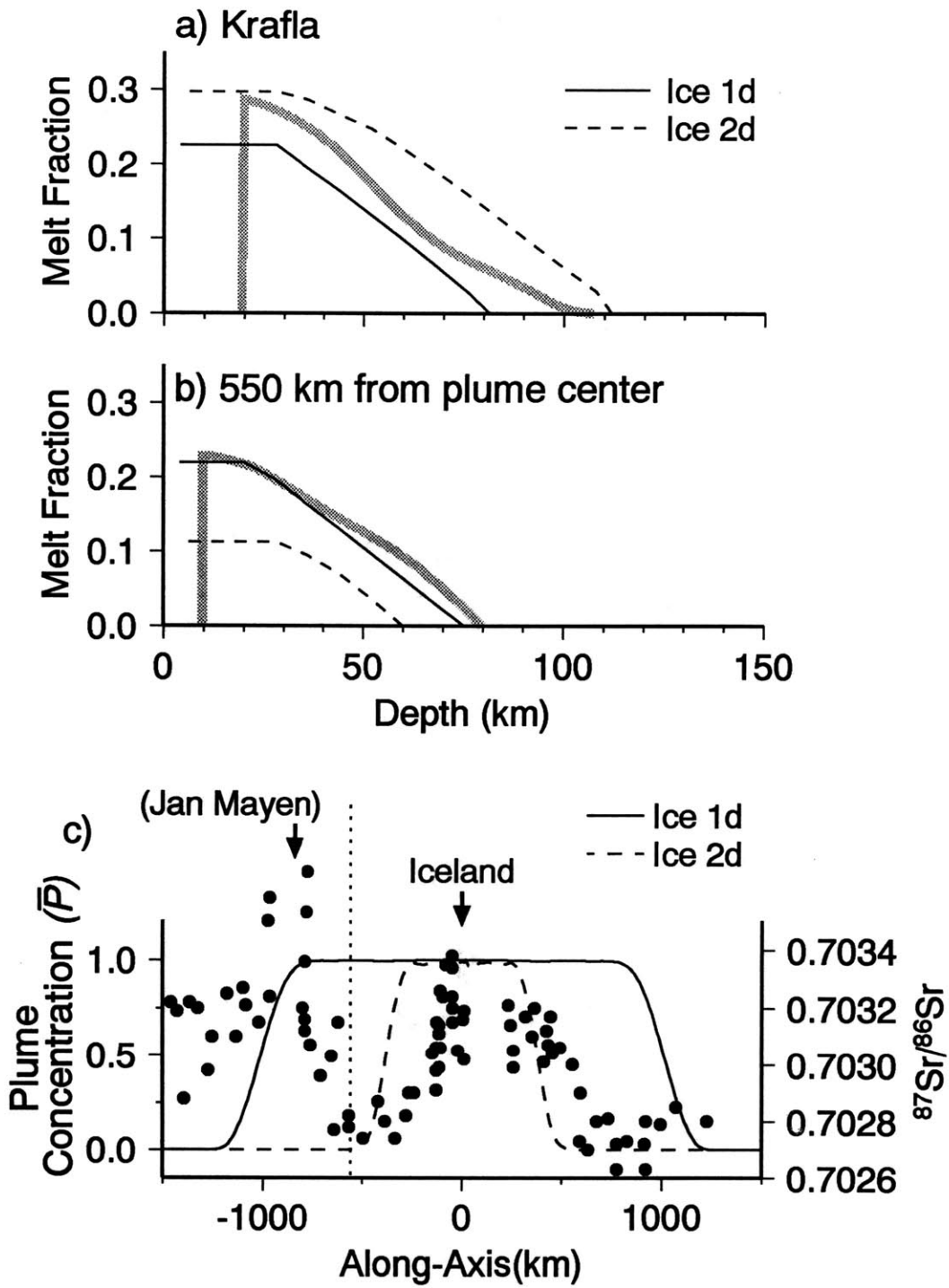
Figure 8

Fig. 9. (a) Lower diagram shows predicted P-wave velocity variations with contour interval of 0.5% for model Ice 1d (broad plume source) caused by the combined effects of temperature, melt depletion, and melt retention. Top panel illustrates the predicted P-wave travel-time delays, assuming vertically passing rays, for along axial and across-axis profiles due to successively added mantle effects as labeled. (b) Same as (a) but for model Ice 2d (narrow plume source). The lowest velocity region occurs at depths 50-100 km due to the predicted high melt retention.

a)

b)
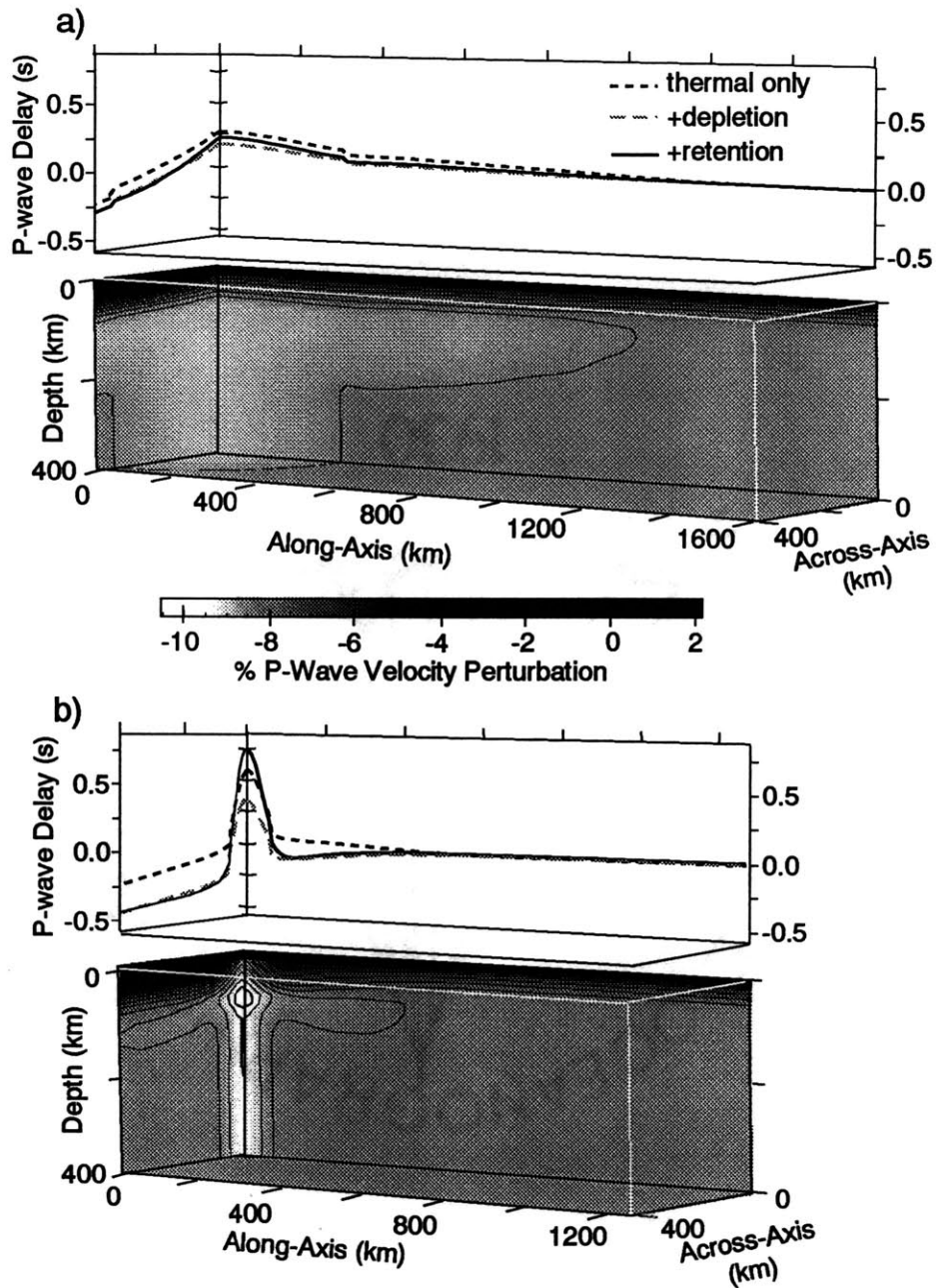
Figure 9

Fig. 10. Characteristic variables predicted by models with melting normalized by those predicted by models without melting. We choose the mean value of $W(Q/U)^{-1/2}$ for each experimental set and maximum value of along-axis variations for each of the other variables. Crustal thickness anomalies are normalized by calculations with thermal buoyancy and latent heat loss.

Figure 10
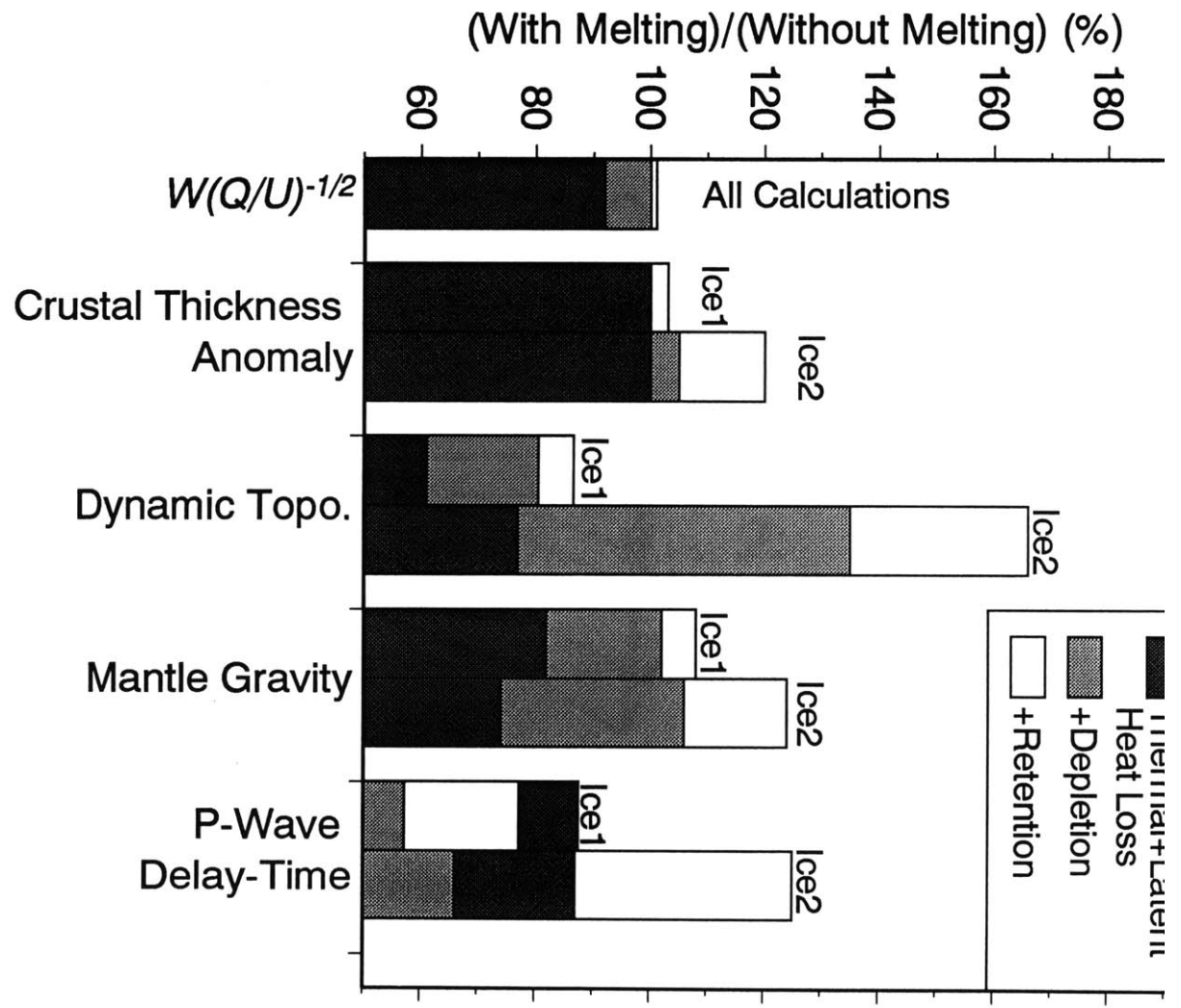
CHAPTER 4

DYNAMIC INTERACTION BETWEEN MANTLE PLUMES AND MIGRATING MIDOCEAN RIDGES

Dynamic interaction between mantle plumes and migrating midocean ridges

Garrett Ito

MIT/WHOI Joint Program, Department of Geology and Geophysics, Woods Hole Oceanographic Institution, Woods Hole, MA, 02543; 508-289-2575 (tel), 508-457-2187 (fax), gito@magellan.whoi.edu

Jian Lin

Department of Geology and Geophysics, Woods Hole Oceanographic Institution, Woods Hole, MA, 02543; 508-289-2576 (tel), 508-457-2187 (fax), jlin@whoi.edu

Carl W. Gable

Earth and Environmental Sciences, Los Alamos National Laboratories, Los Alamos, NM, 87545; 505-665-3533 (tel), gable@lanl.gov

Abstract. We investigate the three-dimensional interaction of mantle plumes and migrating midocean ridges with variable viscosity numerical models. Scaling laws derived for stationary ridges in steady state with near-ridge plumes are consistent with those obtained from independent studies of *Ribe* [1996]. Our numerical results suggest that along axis plume width W and maximum distance of plume-ridge interaction x_{max} scale with $(Q/U)^{1/2}$, where Q is plume source volume flux and U is ridge full spreading rate. Both W and x_{max} increase with buoyancy number Π_b, which reflects the strength of gravitational- versus plate-driven spreading, and γ, which is the ratio of ambient/plume viscosity. In the case of a migrating ridge, the distance of plume-ridge interaction is reduced when a ridge migrates toward the plume due to the excess drag of the faster-moving leading plate, and enhanced when a ridge migrates away from the plume due to the reduced drag of the slower-moving trailing plate. Thermal erosion of the lithospheric boundary layer by the plume further enhances W and x_{max} but to a degree that is secondary to the differential migration rates of the leading and trailing plates. These numerical models are tested by comparing model predictions of bathymetry and gravity with observations of the Galápagos plume-migrating ridge system. The amplitudes and widths of along-isochron bathymetric and gravity anomalies can be explained with models of a plume source temperature anomaly of 80-120°C, radius of 80-100 km, and volume flux of 4.5 x 10^6 km^3/m.y. The observed increase in anomaly amplitude with isochron age is also explained by our models which predict higher crustal production rates when the ridge was closer to the plume source several million years ago. The same plume-source models also predict crustal production rates of the Galápagos Islands that are consistent with those estimated independently from the observed island topography. Predictions of the

geochemical signature of the plume along the present-day ridge suggest that mixing between the plume and ambient mantle sources, as inferred from geochemical observations, is unlikely to occur in the asthenosphere or crust. Instead, mixing most likely occurs much deeper in the mantle, possibly by entrainment of ambient material as the plume ascends through the depleted portion of the mantle from its deep source reservoir.

INTRODUCTION

A wide range of geologic and geochemical observations provide strong evidence that mantle plumes feed material to nearby midocean ridges [e.g. *Vogt*, 1971; *Schilling*, 1973; *Schilling et al.*, 1976; *Morgan*, 1978]. Near-ridge plumes are documented to generate along-axis geophysical anomalies with widths exceeding 2000 km [*Ito and Lin*, 1995b] and can induced geochemical signatures for plume-ridge separation distances of nearly 1500 km [*Schilling*, 1991]. The "mantle-plume source/migrating ridge sink" model of Schilling and co-workers suggests that migrating ridges are "fed and dynamically affected by a preferential plume flow along a thermally induced channel at the base of the lithosphere" [*Schilling*, 1991]. This model suggests that a thermal channel is progressively carved into the lithosphere as the ridge migrates over and away from the impinging hot plume [*Morgan*, 1978; *Schilling*, 1985; *Schilling et al.*, 1985]. All of the 13 plume ridge systems considered by *Schilling* [1991] have ridges migrating away from their nearby plumes in support of this plume source-migrating ridge sink model.

Recent numerical modeling and laboratory experimental studies have begun to characterize the kinematic and dynamic aspects of the interaction between mantle plumes and stationary midocean ridges. For ridge-centered plumes, scaling laws for the dependence of along-axis plume width W on plume volume flux Q and ridge full spreading rate U were first explored in tank experiments [*Feighner and Richards*, 1995] and further developed in numerical studies [*Feighner et al.*, 1995; *Ribe et al.*, 1995; *Ito et al.*, 1996]. The dynamics of off-axis plumes were first investigated in the laboratory by *Kincaid et al.* [1995a] and in 2-dimensional (2-D) numerical experiments by *Kincaid et al.* [1995b]. Finally, *Ribe*'s [1996] study of off-ridge plumes established scaling laws for the dependence of W on a range of variables including Q, U, plume-ridge distance x_p, and lithospheric thickening with age.

While the above studies established scaling parameters of plume ridge interaction they did not investigate the effects of ridge migration. In the more realistic case of a migrating ridge, not only may thermal thinning of the lithosphere be important as proposed by

Schilling's and co-worker's plume source-ridge sink hypothesis, but also the plate trailing the migrating ridge moves significantly slower than the plate leading the ridge, thereby inducing less drag on the plume away from the ridge [*Ribe*, 1996] .

We here explore the dynamics of migrating ridges and plumes with 3-D numerical models that include thermal diffusion and fully pressure- and temperature-dependent rheology. We will first establish scaling laws for along-axis plume width W and maximum plume-ridge interaction distance x_{max} for steady-state systems of stationary ridges. These results will be compared with those of the chemically buoyant, constant viscosity plume models of *Ribe* [1996] first to verify the scaling parameters and then to quantify the importance of thermal diffusion and variable plume viscosity on these scaling laws. We will then quantify the effects of ridge migration on W and x_{max} and identify the physical mechanisms controlling this plume source-migrating ridge sink model. Finally, we will test our models by comparing model predictions with geophysical observations of the Galápagos plume-migrating ridge system, and then discuss the implications for the dimensions, temperature anomaly, volume flux, and geochemical signature of the Galápagos plume.

GOVERNING EQUATIONS AND NUMERICAL METHOD

The mantle is modeled as a viscous Boussinesq fluid of zero Reynolds number and infinite Prandtl number. The equilibrium equations include conservation of mass

$$\nabla \bullet u = 0, \tag{1}$$

momentum

$$\nabla \bullet \tau = \Delta \rho g, \tag{2}$$

and energy

$$\frac{\partial T}{\partial t} = \kappa \nabla^2 T - u \bullet \nabla T \tag{3}$$

(see Table 1 for definition of variables). Mantle density ρ is reduced by thermal expansion such that $\Delta \rho = \rho_o \alpha \Delta T$, and the 3-D stress tensor τ depends on the strain rate tensor $\dot{\varepsilon}$ according to $\tau = 2\eta \dot{\varepsilon} - pI$. Viscosity η depends on pressure p and real temperature T_R according to.

$$\eta = \eta_o \exp\left\{ \frac{E + pV}{RT_R} - \frac{E + \rho_o g(0.5D)V}{RT_{Ro}} \right\} \tag{4}$$

95

in which T_{Ro} is the real temperature of the mantle at $z = 0.5D$. Reduced values of R and V are used to simulate numerically the behavior of a non-Newtonian rheology (i.e. $\dot{\varepsilon} \propto \tau^3$) [*Christensen*, 1984]. The ratio of ambient/plume viscosity γ is defined as η_o/η_p, where η_p is the viscosity of the plume at $z = 0.5\ D$.

Calculations were done using the Cartesian numerical code first written by *Gable* [1989] and *Gable et al.* [1991], and later modified by *Ito et al.* [1996] to incorporate variable viscosity. The numerical setup is illustrated in Fig. 1. Two spreading plates are simulated by imposing surface horizontal velocities of $u_x = +U/2$ and $u_x = -U/2$ on both sides of a model ridge axis. A plume is introduced by imposing a columnar-shaped temperature anomaly in the lower portion of the box at a distance x_p from the ridge axis. The plume source is hottest $(T = T_o + \Delta T_p)$ at its center and cools as a Gaussian function of radial distance to T_o at its full radius. The vertical sides of the box are free of shear stress and have zero horizontal temperature gradient. Therefore, the symmetry introduced by the reflecting side boundaries allow this half-of plume-ridge system in numerical models to simulate a full plume-ridge system in virtual space. Temperature at the surface is maintained at $0°C$ which cools and thickens a high viscosity lithosphere approximately with the square root of distance from the ridge axis. Temperatures in the lower portion of the box $(z > 0.6D)$ are maintained at the reference mantle potential temperature T_o everywhere except inside the plume source. Correspondingly, the energy equation is solved in only the upper portion of the box $(0.6D \geq z \geq 0)$. The purpose of the lower volume of the box is to simulate an open boundary at the base of the upper volume where the plume-ridge interaction occurs. To ensure numerical accuracy of the flow solutions, we limit the horizontal viscosity variation to be $<10^3$ by defining an upper viscosity limit for the lithosphere depending on the viscosity of the hot plume.

To track the flow of the mantle plume, we introduce a passive tracer P in the plume source with value of 1.0 to represent 100% plume material. A finite difference, tensor diffusion method [*Gable*, 1989; *Travis et al.*, 1990] is used to solve for advection of P, from the source and throughout the upper volume of the box $(z < 0.6D)$. Diffusion of P is required by our numerical method but the rate of diffusion is reduced by a factor of 3 relative to the rate of thermal diffusion. P is also used to determine along-axis width of the plume by measuring the along-axis distance over which the mean value of P beneath the

ridge, $\left(\dfrac{1}{0.6D} \displaystyle\int\limits_{0}^{0.6D} P(0,y,z)dz \right) | \ P > 0$, is greater than 0.1. Finally, we use P in the steady-state stationary ridge case, to measure the volume flux of plume material crossing the ridge axis by integrating horizontal velocities on the side of the ridge opposite the plume where $P > 0.4$. The volume flux of the plume source Q is measured by integrating vertical velocities at $z = 0.6D$ over the cross-sectional area of the source column.

SCALING LAWS FOR STATIONARY RIDGES

Feighner and Richards [1995] and *Feighner et al.* [1995] demonstrated that $W_o = (Q/U)^{1/2}$ is an effective length scale for characterizing the horizontal dimension of a ridge-centered, gravitationally spreading plume. They also defined a plume buoyancy number $\Pi_b = Q\sigma/U^2$ where $\sigma = g\Delta\rho/48\eta_o$, which characterizes the relative strength of gravitational versus plate-driven spreading. Subsequent analyses of *Ribe et al.* [1995] derived a characteristic plume thickness scale $S_o = (Q/\sigma)^{1/4}$, which determines Π_b according to $\Pi_b = (W_o/S_o)^4$. The effect of the sloping lithosphere on the interaction of off-axis plumes was characterized with the "upslope number" $\Pi_u = Q^{1/8}\sigma^{3/8}\kappa^{1/2}/U$ by *Ribe* [1996].

The above scaling quantities were shown by lubrication theory models of *Ribe* [1996] to define a full scaling law of along-axis width W for steady-state stationary ridges,

$$W = W_o F_1(\Pi_b) F_4(\Pi_b,\Pi_u) F_3(\frac{x_p}{W_o},\Pi_b,\Pi_u). \tag{5}$$

Functions F_1 and F_4 describe the increase in steady-state width with increasing values of Π_b and Π_u, for ridge-centered plumes ($x_p = 0$); whereas function F_3 describes the first-order dependence of W on plume-ridge separation distance x_p and the second-order dependence on Π_b and Π_u. We now further investigate this scaling law with numerical models that include both thermal diffusion and temperature-dependent plume viscosity.

Ridge-centered plumes

The simplest case is that of a ridge-centered plume. In this case $x_p = 0$ and $F_3 = 1.0$, therefore we seek to define functions F_1 and F_4. In our numerical experiments, we vary full spreading rate U between 20 and 120 km/m.y. and modulate plume flux Q by varying plume temperature anomaly ΔT_p between 100 and 200°C (see Table 2). Three models of

plume viscosity structure are examined. The first is designed to simulate the constant plume-viscosity calculations of *Ribe* [1996]. This viscosity structure omits the pressure-dependence of Eq. 4 and has $\eta = \eta_o$ for $T \geq T_o$, thus plume viscosity is the same as the ambient fluid ($\gamma = 1.0$). To allow for a thickening lithospheric boundary layer, we incorporate the temperature-dependence in Eq. 4, for $T < T_o$. The second and third viscosity models have the full pressure- and temperature-dependence as defined by Eq. 4; the second has $\gamma = 2.352$ for $\Delta T_p = 100°C$, and the third has $\gamma = 5.053$ for $\Delta T_p = 200°C$.

A scaling law for normalized plume width W/W_o, which defines F_1, is determined by fitting W/W_o to exponential functions of the quantity $\Pi_b\gamma$, a modified buoyancy number defined by the viscosity of the plume [*Ito et al.*, 1996]. W/W_o is described well by the function

$$\log_{10}(W/W_o) = 0.32 + 0.01[\log_{10}(\Pi_b\gamma)] + 0.05[\log_{10}(\Pi_b\gamma)]^2 \qquad (6)$$

with a standard deviation misfit of 8% of the median value of 2.25 (Fig. 2). This function is consistent in general form with *Ribe*'s [1996] results of $\log_{10}(W/W_o) = 0.217 + 0.0569[\log_{10}(\Pi_b\gamma)] + 0.0176[\log_{10}(\Pi_b\gamma)]^2 + 0.0275[\log_{10}(\Pi_b\gamma)]^3$. The relatively weak dependence of W on $\log_{10}(\Pi_b\gamma)$ in our results may reflect our source radius of finite width, which becomes comparable to W_o at low values of $\Pi_b\gamma$ and thus contributes to along-axis width in a manner unlike by *Ribe*'s [1996] point source plumes. In addition, we are unable to identify a dependence on Π_u which is described by *Ribe*'s [1996] function $F_4 = (1 + 1.77 \, \Pi_u \, \Pi_b^{-0.33})$.

Off-axis plumes

To derive scaling laws for off-axis plumes, we seek to define the function F_3. Fig. 3 illustrates the shape of the plume at different distances from the ridge axis. When the plume is ridge-centered, it spreads along the ridge-axis, is divided by the spreading plates, and then spreads symmetrically away from the ridge axis. When it is off the ridge, the plume spreads asymmetrically beneath the moving plate with the upwind side tapering towards the ridge and the downwind side widening away from the ridge as it is sheared away by the moving plate. The ridge thus captures a narrower width of the plume as x_p is increased. If x_p is large enough, the ridgeward flowing plume material stagnates against the migrating plate as investigated by *Sleep* [1987] and *Ribe and Christensen* [1994]. It is this stagnation distance that defines the maximum distance to which plume material will contact the ridge axis, x_{max}.

Function F_3 is the dependence of W on plume-ridge distance and is equivalent to $W/W(x_p=0)$ (Eq. 5). Fig. 4a shows numerical results of F_3 versus x_p/W_o. The best fitting function is a binomial function of the form

$$F_3 = [1.0 - 0.68(x_p/W_oF_2)^2]^{1/2} \qquad (7)$$

as consistent with that of *Ribe* [1996]. As evident in Fig. 4a, cases with $\gamma = 1.0$ yield the shortest distances of plume-ridge interaction, whereas increasing values of γ result in greater distances of plume-ridge interaction. This second order variation in plume width reflects a stretching function F_2, which depends primarily on γ and secondarily on Π_b with a best fitting function

$$F_2(\Pi_b\gamma) = (\Pi_b\gamma)^{0.01}\gamma^{0.14}. \qquad (8)$$

As illustrated in Fig. 4b, F_2 collapses values of $W/W(x_p=0)$ on to a single curve. Thus the combined Eqs. 7 and 8 describe effectively the dependence of W on plume ridge distance for steady-state cases. The primary dependence of F_2 on γ may indicate that not only do less viscous plumes spread stronger gravitationally, but also they are subject to less shearing from the overlying migrating plate. The increase in x_{max} with γ as predicted here is consistent with results of 2-D experiment by *Kincaid et al.* [1995b]. F_2 derived from our numerical models captures the linear exponential term of *Ribe*'s [1996] function, $\log_{10}(F_2)=0.043[\log_{10}(\Pi_b)] + 0.060[\log_{10}(\Pi_b)]^2 - 0.0062[\log_{10}(\Pi_b)]^3$; however, our results show a weaker dependence on Π_b. We again do not observe a strong dependence of F_3 on Π_u over the range of Π_u examined.

We also investigate the percentage of the plume flux that crosses the ridge axis Q_r. For ridge-centered cases, half of the plume material flows to each side of the ridge such that $Q_r = 0.50$. As the plume moves away from the ridge axis, Q_r decreases according to

$$Q_r = 0.50 - 0.41(x_p/W_oF_2) \qquad (9)$$

as illustrated in Fig. 5. This function is again similar to that of *Ribe's* [1996], $Q_r = 0.5 - 0.79p + 0.24p^2$, where $p = (x_p/W_oF_2)$.

Functions F_3 and Q_r (Eqs. 7 and 9) are zero when $x_p = x_{max}$, and consequently

$$x_{max} = 1.21W_oF_2. \qquad (10)$$

For the case of $\gamma = 1.0$, our predicted values of x_{max}/W_o are ~50% greater than those predicted by *Ribe* [1996]. Some of this discrepancy may be due to differences in numerical models; for example our finite source radius versus *Ribe*'s [1996] point source as mentioned earlier. Another potentially important cause of this discrepancy may be thermal erosion of the lithosphere. Fig 6. illustrates the thickness of the lithosphere that was eroded by the plume scaled by the modified characteristic plume thickness $S_o\gamma^{-1/4} =$

$$\left(\frac{48Q\eta_p}{g\Delta\rho}\right)^{1/4}$$. The greatest erosion occurs downwind of the plume where the plume has been in contact with the lithosphere the longest. The downwind slope of the channel acts to inhibit ridgeward spreading as noted by *Kincaid et al.* [1995a,b]; however, our results suggest that the dominant effect is the slope of the channel in the *y*-direction which enhances spreading toward the ridge by inhibiting spreading in the along-axis direction. *Ribe* [1996] predicted this effect to enhance W by ~10%.

The similarities between the above scaling laws for ridge-centered and off-axis plumes and those of *Ribe* [1996] indicate that the general form of these scaling laws are robust and insensitive to differences in far field boundary conditions. The additional physics we include are variable plume viscosity and thermal erosion, both of which enhance W at a given value of x_p as well as the total range over which an off-axis plume interacts with a nearby stationary ridge.

SCALING LAWS FOR MIGRATING RIDGES

To derive scaling laws for the case of a migrating ridge we simulate a ridge moving in the positive *x*-direction at velocity V_r. With respect to the ridge, both plates are assumed to spread symmetrically at a rate of $U/2$; therefore with respect to the plume, Plate 1 (the leading plate moving in the positive *x*-direction) spreads with velocity $+U/2 + V_r$ and Plate 2 (the trailing plate moving in the negative *x*-direction) spreads with velocity $-U/2 + V_r$ (Fig. 7). These velocity conditions are incorporated by defining the appropriate horizontal velocities of the surface boundary, whereas the motion of the ridge is simulated by redefining the *x*-position of the diverging surface velocities at each step during time integration.

Numerical experiments began with the steady-state configuration of a plume and stationary ridge, with the plume beneath Plate 1 at $x_p > x_{max}$. We then allowed the ridge to migrate toward, over, and away from the plume such that the plume ends up beneath Plate 2. We use the convention, $x_p > 0$ when the plume is beneath Plate 1 and $x_p < 0$ when the plume is beneath Plate 2. Three ridge migration velocities are tested for parameters of experiments 3, 5, 7, 8, and 12 (Table 2). In each case, the maximum V_r examined is equal to the half spreading rate.

The dependence of W on x_p is shown in Fig. 8 for experiment 7. The form of the function of W versus x_p/W_0 is the same as that of F_3 in Eq. 7, but the curves are shifted

increasingly in the negative x_p-direction with increasing V_r, and the total range over which the plume interacts with the ridge broadens with V_r. F_3 is thus modified to

$$F_3 = \left[1.0 - 0.68 F_6(s, \Pi_b \gamma) \left(\frac{x_p / W_o + F_5(s, \Pi_b \gamma)}{F_2(s, \Pi_b \gamma)} \right)^2 \right]^{1/2}, \quad s = (2V_r/U). \quad (11)$$

Function F_5 describes the shift of the curves in the negative x_p-direction and is best fit by the function

$$F_5 = 0.39 (\Pi_b \gamma)^{-0.12} (2V_r/U) \quad (12)$$

(Fig. 9a). Function F_6 controls the increase in total range of plume-ridge interaction and is best fit by the function

$$F_6 = 1.0 - 0.17 (\Pi_b \gamma)^{-0.12} (2V_r/U)^{1/2} \quad (13)$$

(Fig. 9b).

Function F_5 reflects largely the differential shearing of the plume by the asymmetrically moving plates and has the largest effect on the range of plume ridge interaction. When $x_p > 0$, the plume's upwind stagnation point defines the maximum distance to which the plume interacts with the ridge. The faster moving Plate 1 induces more drag on the plume away from the ridge (Fig 7a) therefore pushing the stagnation point closer to the plume source and reducing x_{max} relative to the case in which $V_r = 0$. When $x_p < 0$, the plume separates from the ridge when the ridgeward spreading velocity of the plume drops below the migration rate of the ridge. The slower moving Plate 2 induces less shear away from the ridge (Fig. 7b), consequently, the plume is able to keep up with the migrating ridge over a greater distance. F_5 reduces x_{max} for $x > 0$ and increases x_{max} for $x < 0$ by as much as 35% of x_{max} for a stationary ridge. The degree to which the differential motion of the two plates is able to alter the shape of a plume diminishes for strong plumes. This is reflected in the inverse relationship between F_5 and $\Pi_b \gamma$.

Function F_6 most likely reflects the effects of lithospheric erosion, which increases the total range over which the plume interacts with the ridge. Thermal erosion has the strongest effect on the system after the ridge has migrated over and away from the plume (Fig 10) as hypothesized by *Schilling* [1991]. In the case that V_r is small (Fig. 10a), the velocity of Plate 2 is largest thus allowing the plume to erode a greater area of the plate downwind of plume source. Consequently, the plume spreads more easily away from the ridge through the downwind eroded channel. On the other hand, when V_r is larger (Fig. 10b and 10c), Plate 2 moves slower, and the downwind channel is more confined to the

101

plume source, thereby enhancing spreading toward the ridge. The dependence of F_6 on $2V_r/U$ weakens, however, with increasing $\Pi_b\gamma$ because the shape of the overlying lithosphere has less effect on gravitational spreading of the plume at higher values of $\Pi_b\gamma$. For $V_r = U/2$, F_6 increases the total range of plume ridge communication by an average of 11%.

Thus, lithospheric erosion has only second-order importance in influencing the flow of near-ridge plumes—a result that differs from that envisioned in Schilling and co-worker's plume source-migrating ridge sink model. The effects of the lithosphere are likely to be weakest when the characteristic plume thickness $S_o\gamma^{-1/4}$ is large relative to the thickness of the lithospheric boundary layer. Indeed, the values of $S_o\gamma^{-1/4}$ examined here are 100-150 km—3-5 times the thickness of the lithosphere overlying the plumes. The regime in which $S_o\gamma^{-1/4}$ is comparable to the thickness of the lithosphere would allow the lithosphere to influence more strongly the ability of the plume to spread to the ridge. This low-$S_o\gamma^{-1/4}$ regime would require significantly hotter plumes to reduce η_p, as well as significantly narrower sources radii to limit Q. Such conditions, however, may be unusual in the Earth given that the 50-km radius and 100-200°C temperature anomalies examined here are reasonable properties of Earth plume examples [e.g. *Ito and Lin*, 1995b; *Schilling*, 1991; *Wolfe et al.*, 1996]

Our complete scaling law for plume width and migrating ridge is thus

$$W = W_o\, F_1(\Pi_b\gamma)\left[1.0 - 0.68F_6(s,\Pi_b\gamma)\left(\frac{x_p/W_o + F_5(s,\Pi_b\gamma)}{F_2(s,\Pi_b\gamma)}\right)^2\right]^{1/2}, \qquad (14)$$

and our complete our scaling law for the maximum plume-ridge interaction distance is

$$x_{max} = (\pm 1.21 F_2 F_6^{-1/2} - F_5)W_o. \qquad (15)$$

Ridge migration has first order effects on the dynamics of plume-ridge interaction. On average, ridges migrating toward plumes at rates comparable to their half spreading rates, can sample plume material over distances ~24% less than stationary ridges. Ridges migrating away from plumes at rates comparable to their half spreading, however, are able to sample plume material to plume-ridge distances ~36% greater than stationary ridges and almost twice as far as ridges migrating toward plumes.

THE GALÁPAGOS PLUME-MIGRATING RIDGE SYSTEM

We compare model predictions with observations at the Galápagos plume and spreading center, a classic and relatively well studied example of an off-axis plume-migrating ridge system (Fig. 11). The Galápagos spreading center separates the Cocos plate to the north and the Nazca plate to the south with a full spreading rate of ~55 km/m.y. at 91°W [*DeMets et al.*, 1994]. The ridge is currently migrating northward with respect to the hotspot at a rate of 27 km/m.y. [*Gripp and Gordon*, 1990], which is ~1 km/m.y. less than the half-spreading rate. *Ito and Lin* [1995a] documented that the total amplitude of bathymetric and mantle-Bouguer gravity anomalies (MBA) along Cocos Plate isochrons increase with isochron age, and suggested that this behavior reflects increased crustal production in the past when the plume was closer to the ridge. Our purpose here is to compare predicted and observed profiles of bathymetry and MBA in order to assess the degree to which the models can explain the observations and to place theoretical constraints on the dimensions, temperature anomaly, and flux of the Galápagos plume.

Calculations of crustal thickness, bathymetric, and gravity anomalies

Because 70-75% of the along-isochron bathymetric and gravity variations most likely arise from plume induced thickening of the igneous crust [*Ito and Lin*, 1995a], crustal thickness calculations are a crucial link between our fluid dynamic models and surface observations. To predict crustal thickness along a model ridge axis, we incorporate the solidus and liquidus functions of *McKenzie and Bickle* [1988], as well as their functional dependence of melt fraction M on homologous temperature for adiabatic batch melting. Assuming melt generated in the mantle accretes perpendicularly to the ridge axis, crustal thickness along the ridge is calculated according to

$$Cr(y) = \frac{1}{U}\left(\frac{\rho_o}{\rho_m}\right)\iint \dot{M}(x,y,z)dxdz \qquad (16)$$

where $\dot{M} = \dfrac{\partial M(p,T)}{\partial t}$. This method generates a normal ridge crustal thickness of 6.5 km with the assumed ambient mantle temperature T_O of 1300 °C. Because the Galápagos plume enhances crustal production at the ridge as well as generates Galápagos Islands, an important source of uncertainty is how melt produced by the plume is partitioned between the ridge and hotspot islands. We do not attempt to model melt migration from the mantle to the ridge and islands, but instead, we assume that all melt generated closest to the ridge

axis accretes at the Galápagos Spreading Center and all melt generated closest to the plume source accretes at the Galápagos Islands. Crustal thickness along the ridge and at the hotspot therefore change with time as a direct result of the position of the ridge and plume source. For this reason we compare not only predicted and observed anomalies at the Galápagos Spreading Center but also crustal production rates of the Galápagos Archipelago.

When considering melting, it is important also to account for its effects on the mantle [*Ito et al.* 1996]. Melting reduces mantle temperature due to latent heat loss, which increases both mantle density and viscosity; but at the same time, melting reduces mantle density by preferential extraction of iron with respect to magnesium [*Oxburgh and Parmentier*, 1977]. Latent heat loss is incorporated by introducing a source term - $(T\Delta S/c_p)\,\dot{M}$ in the energy equation (Eq. 3). The compositional effect on mantle density is incorporated by the equation

$$\Delta\rho = \rho_o(\alpha T + \beta X), \tag{17}$$

where X is the extent of melt depletion and $\beta = 0.24$ is a coefficient of depletion density reduction [*Oxburgh and Parmentier*, 1977]. The equilibrium equation for the depletion field is

$$\frac{\partial X}{\partial t} = -u \bullet \nabla X + \dot{M}, \tag{18}$$

in which the advection term is solved using the same tensor diffusion method as that used to solve for temperature field, and the source term $\dot{M}$ is solved as describe above. The above melting effects do not modify significantly the broad scale flow of the plume [*Ito et al.* 1996]; however, they contribute substantially to the mantle contributions to bathymetric and gravity anomalies.

To calculate isostatic topography of the seafloor, we consider contributions from both the crust and mantle. In calculating crustal topography, we assume Airy-type compensation of the crust assuming a normal crustal density of 2700 kg/m^3 that increases linearly along axis to ρ_{max} within 500 km of the point closest to the hotspot (~91°W). Values of ρ_{max} considered are 2900 and 3000 kg/m^3. In calculating topography due to the mantle, we assume Pratt-type compensation with a compensation depth of 200 km and include both thermal and compositional density effects as defined in Eq. 17.

Mantle-Bouguer gravity anomaly (MBA) is the free-air gravity minus the attraction due to topography of the seafloor and crust-mantle interface assuming a reference crust of

uniform density (e.g., 2700 kg/m^3) and thickness (e.g., 6.5 km) [e.g. *Kuo and Forsyth*, 1988; *Lin et al.*, 1990]. MBA therefore reflects crustal thickness structure that differs from this reference crust as well as variations in mantle density. To calculate MBA, we again include the contribution of along-axis crustal thickness variations, and thermal and compositional mantle density variations [*Ito et al.* 1996].

We investigate two radii and temperature anomalies for the Galápagos plume source: one has a radius of 100 km and temperature anomaly ΔT_p of 80°C, and the other has a radius of 80 km and ΔT_p of 120°C. Both plume source models predict comparable volume fluxes of 4.5x10^{6}km^3/m.y.—a value slightly greater, but comparable to the prediction of 2.6-3.6 km^3/m.y. by *Schilling* [1991] and the 2.2x10^6 km^3/m.y. lower-bound prediction of *Ito and Lin* [1995b]. Values for T_o of 1300 °C and η_o of 3 x 10^{19} Pa s yield a Rayleigh number of 3.05 x 10^6. We began model calculations began with a steady-state condition of the plume beneath Plate 1 (Cocos Plate). We then activated ridge migration and tracked crustal production and mantle evolution as the ridge migrated over the plume source. Calculations finished with Plate 2 (the Nazca Plate) over the plume source and when the ridge was 200 km from the plume source. This distance is the average distance between Fernadina Island and the two ridge segments east and west of the transform fault at 91°W (Fig 11).

Predicted and observed bathymetric and gravity anomalies

Model predictions of bathymetry and MBA are compared with five along-isochron profiles investigated by *Ito and Lin* [1995a]: the present-day ridge axis and isochrons at crustal ages of 2.6, 3.6, 6.0, 6.6, and 7.7 m.y. *Hey* [1977] suggested that the Galápagos Spreading Center was centered over the plume ~10 Ma. Therefore, we associated model crustal profiles with isochrons by taking the crustal profiles generated with x_p values that were the same fractions of 200 km as each isochron was of 10 m.y. For example the 3.6 Ma isochron was assumed to have formed when the plume was 36% closer to the ridge than it is today, i.e., x_p = 128 km. Mantle bathymetric and gravity profiles were extracted at x-positions on Plate 1 (Cocos Plate) corresponding directly to the isochron ages. The total predicted bathymetric and MBA anomaly profiles are the sum of the crustal and mantle contributions.

The comparisons between model and observed profiles in bathymetry are shown in Fig. 12 for ρ_{max} = 2900 kg/m^3. Along the present day ridge axis and isochrons younger than 6 m.y., both models predict reasonably well the amplitudes and wavelengths of the

105

observations. Along isochrons older than 6 m.y., the cooler plume source of model 1 also yields predictions consistent with the observations but the hotter plume source of model 2 over-predicts the bathymetric anomalies.

The similar anomaly amplitudes predicted by the two models at the youngest isochrons (i.e., 200 km $\geq x_p \geq$ 128 km) reflects the similarity between the amount of melt partitioned to the axial crust despite the differences in plume source properties. Although the cooler plume source of model 1 is predicted to generate less total melt than the hotter source of model 2, the greater radius of the model 1 plume source causes more melting to occur near the ridge axis, thus, a larger percentage of the total melt liberated is partitioned to the ridge. On the other hand, the narrower source of model 2 predicts melting to be more localized to the center of the plume source, therefore, a smaller percentage of the total melt generated is partitioned to the ridge axis. This trade-off between source radius and temperature explains why at the younger isochrons, the two different plume sources yield similar crustal thicknesses at the ridge axis. Along the oldest three isochrons (i.e., 128 km > $x_p \geq$ 40 km), however, the differences between the bathymetric predictions of models 1 and 2 are greatest because the amount of melt partitioned to the ridge crust reflects a larger percentage of the total melt produced. Consequently, the hotter source model (model 2) over predicts the crustal thickness at the ridge axis.

While the difference between the two source temperature anomalies is but slight, the differences between predicted crustal thickness anomalies at the three oldest isochrons is substantial: model 2 predicts crustal thickness anomalies of 11-15 km, about twice as large as the 6-8 km-anomalies predicted by model 1. These large differences in predicted crustal thickness anomalies reflects the high sensitivity of upwelling thus melting rate to plume temperature anomaly due to the combined effects of reduced viscosity and enhanced thermal and depletion buoyancy. Directly above the plume source, model 2 predicts a maximum upwelling rate 250 km/m.y. This rate is nearly twice as high as that predicted by model 1 of 140 km/m.y., thus explaining the factor of two difference between the model 2 and model 1 crustal thickness anomalies at the three oldest isochrons.

Directly beneath the plume-affected portion of the present-day ridge axis (i.e. directly north of the plume), however, both models 1 and 2 predict a ~30% reduction of upwelling/melting rate relative to that beneath the unaffected portions of the ridge; the reason being, is that upwelling that normally accommodates plate spreading is replaced by lateral flow supplied by the plume. A significant proportion the melting that contributes to ridge axis crust at the present-day, is therefore predicted to occur near the midpoint between

the plume source and the Galápagos Spreading Center. The maximum extent of melting predicted at present-day is 23% for model 1 and 26% for model 2.

Because crustal thickness at the ridge is predicted to increase with isochron age, the contribution to bathymetry of the crust relative to that of the mantle also is predicted to increase. Model 1, for example, predicts a crustal uplift at the present-day ridge axis of 0.6 km, which is 60% of the predicted total anomaly of 1.0 km. In contrast, along the 7.7-m.y. isochron, model 1 predicts a crustal uplift of 1.2 km, which is 80% of the predicted total bathymetric anomaly of ~1.5 km. Likewise, model 2 predicts a crustal uplift along the present-day ridge of 0.6 km, which is 50% of the total anomaly of 1.2 km, and a crustal uplift along the 7.7-m.y. isochron of 2.4 km, which is 80% of the total predicted anomaly of ~3.1 km. These predictions are consistent with the gravity and bathymetry analyses of *Ito and Lin* [1995a] which suggested that the depth of compensation shallows with increasing isochron age.

Comparisons between predicted and observe MBA profiles are shown in Fig 13. Similar to the results of the bathymetry comparisons, both models 1 and 2 yield MBA amplitudes and widths consistent with the observations for the three youngest isochrons, but model 2 over-predict the amplitudes of the MBA at the three oldest isochrons. In model 1, the crustal component of MBA is predicted to be 65% of the total predicted anomaly of -80 mGal at the present-day ridge axis and ~82% of the -140-mGal anomaly predicted along the 7.7-m.y. isochron. Lateral density variations in the mantle supply the remaining proportions of the anomalies. In model 2, the crustal contribution to MBA is predicted to be 55% of the total predicted anomaly of -94 mGal along present-day ridge axis and 80% of the total predicted anomaly of -261 mGal along the 7.7-m.y. isochron. Thus, for both along-isochron MBA and bathymetric anomalies, the relative contribution of the crust is predicted to be 50-80% of the total anomalies—a range slightly greater than the estimates of *Ito and Lin* [1995a] who used a passive mantle upwelling model.

The predicted and observed amplitudes of along-isochron MBA and bathymetric anomalies for both ρ_{max} = 2900 and 3000 kg/m^3 are plotted versus isochron age in Fig 14 (a) and (b). For the youngest isochrons, the observed amplitudes appear to be matched best by predictions of the hotter source of model 2 with the upper-bound ρ_{max} of 3000 kg/m^3. For the oldest isochrons, the observed anomaly amplitudes are best matched by the cooler source of model 1, but again with ρ_{max} of 3000 kg/m^3. Model 2 yields upper-bound predictions for the oldest isochrons. In general, the observed anomaly amplitudes

are bracketed by the predictions resulting from the range of ρ_{max} as well as source radii and temperatures considered.

Galápagos Archipelago crustal volume flux

As discussed above, because of the large uncertainty in evaluating how melt is partitioned between the ridge crust and hotspot islands we must consider also the crustal production rate at the Galápagos Archipelago. We first estimate the total volume of the Galápagos Archipelago by assuming the observed bathymetry is supported by Airy isostasy of the crust. We consider the bathymetry in the white box in Fig. 11, the longitudinal extent of which corresponds to ~10 m.y. of island accretion [*Sinton et al.*, 1996]. Lithospheric flexure [*Feighner and Richards*, 1994] is neglected here because flexure acts to only smooth topography of the crust-mantle interface but does not affect the total volume of the compensating crustal root. To correct for the long wavelength swell topography, which is unlikely to reflect island volcanism, we subtract a reference depth plane with the box's average bathymetric slope in both longitudinal and latitudinal directions. From this residual bathymetric map, we calculate the isostatic thickness of the Galápagos Archipelago and then integrate along latitudinal profiles to derive excess crustal volume as a function of longitude across the box (the mean thickness of a normal oceanic crust of 6.5 km is excluded). Each longitude is then assigned an age assuming a constant eastward migration rate of the Nazca Plate relative to the plume. Finally, we estimate crustal volume flux as a function of age by dividing the estimated volumes by the time spans represented by their spacing in longitude. To be consistent with the assumed values of ρ_{max} along the ridge axis, we consider island crustal densities of 2900 and 3000 kg/m^3.

Fig. 14c shows the estimated island fluxes through time which yield averages of 1.2 x 10^5 and 1.6 x 10^5 km^3/m.y. over the past 7.7 m.y. for crustal densities of 2900 and 3000 kg/m^3 respectively. Similar to the comparisons of the isochron anomalies, the hotter plume source in model 2 predicts an island crustal flux most consistent with the calculated fluxes over the most recent 4 m.y. and an upper-bound for the island flux at times > 4 Ma. The cooler plume source of model 1, on the other hand, predicts lower-bound island fluxes over the most recent 4 Ma and fluxes that are more consistent with the estimated fluxes at times > 4 Ma. In general, the range of source temperatures and radii considered by our two models yield island fluxes consistent with those estimated from the bathymetry of the Galápagos Archipelago .

It is possible that the Galápagos plume source may have changed through time in temperature anomaly, radius, or both as hinted by the closer match of the hotter source model to observations associated with crustal ages < 4 Ma and closer match of the cooler source model to observations associated with crustal ages > 4 Ma. However, given the range of uncertanties in our models it is impossible to resolve such changes in source properties. The conclusions we make are that our numerical plume-ridge models are capable of explaining the first order variations in ridge-axis anomalies and island flux estimates at present-day, as well as explaining the apparent evolution over the past ~8 m.y.

A potentially important test of our models would be a mantle teleseismic study of the Galápagos plume-ridge system, which would test directly our predictions of source dimension and temperature anomaly. Beneath the Galápagos Archipelago, we predict a P-wave velocity reduction of 0.5-0.7% due to the excess temperature of the plume and up to 2% in the melting region if there is up to 3% of melt present in the mantle [*Ito et al.*, 1996]. This prediction is based on a 6.25×10^{-3}% reduction of P-wave velocity for each 1°C temperature anomaly and a 1.25% decrease in velocity for each 1% porosity of melt in the mantle [*Humphreys and Dueker*, 1994]. Such velocity anomalies are predicted to result in a 0.3-0.4 s delay over the center of the hotspot for P-waves passing vertically through the upper 400 km of mantle we have modeled. Along the Galápagos Spreading Center, however, we predict mantle P-wave velocities to actually increase by up to 0.5% in the melting zone relative to normal ridge mantle. The reason for this velocity increase is that the plume material feeding the ridge has already experienced melting at the hotspot; consequently, the velocity enhancing effects of melt depletion (0.1% velocity increase for each 1% degree of depletion [*Humphreys and Dueker*, 1994]) dominate over the velocity reducing effects of temperature and melt retention directly beneath the ridge. Another valuable study would be to obtain seismic constraints on crustal thickness variations along the ridge axis and along the seafloor isochrons. This study would test directly our predictions of along-isochron crustal thickness variations and place hard constraints for geodynamic models such as these.

Geochemical implications

Much of the original observations that led to the concept that plumes feed nearby ridges comes from systematic variations in basalt chemistry. Schilling and co-workers noted that Galápagos ridge axis basalts erupted nearest the Galápagos hotspot have compositional affinities to ocean island basalts (OIB)—being enriched relative to midocean ridge basalts

(MORB) in radiogenic isotopes [*Verma and Schilling*, 1982; *Verma et al.*, 1983] and incompatible rare-earth and major elements [*Schilling et al.*, 1976; *Schilling et al.*, 1982]. They showed that the OIB signatures decrease along the ridge axis with increasing distance from the hotspot. An example of this behavior is revealed in La/Sm ratios as shown in Fig. 15. Such a systematic decrease in the OIB signature is interpreted to reflect mixing between the OIB plume source with the MORB upper mantle source material.

To investigate the processes of plume and ambient mantle mixing, we calculate the amount of plume tracer P composing the model crust along the ridge. After *Ito et al.* [1996], the average plume tracer concentration in accumulated melts as a function of along-axis coordinate is

$$\overline{P}(y) = \frac{\int P(x,y,z)\dot{M}(x,y,z)\mathrm{d}x\mathrm{d}z}{\int \dot{M}(x,y,z)\mathrm{d}x\mathrm{d}z}. \tag{19}$$

By the definition, $\overline{P} = 1.0$ indicates that all melts generated in a plane perpendicular to that point of the ridge is entirely plume-source derived. Likewise, $\overline{P} = 0.0$ indicates that none of the melts are plume derived, and $0.0 < \overline{P} < 1.0$ indicates some of the melts are derived from the plume and some are derived from the ambient mantle material.

As shown in Fig. 15, both models 1 and 2 predict geochemical plume widths consistent with the ~1000-km width inferred from the La/Sm anomaly. The largest difference between predicted and observed profiles is that the predicted profiles indicate very little mixing between the plume-derived and ambient mantle-derived melts over most of the plume-affected portions of the ridge axis. Only at the outermost ~200 km within the edges of the plume is there evidence for plume-ambient source mixing in our models. Similar to *Ito et al.*'s [1996] conclusions for Iceland, we suggest that mixing does not occur in the shallow mantle or in the crust but most likely deeper in the mantle than we have considered in our models. Such a deep mixing process may be entrainment of the ambient mantle material by the plume as it ascends through the isotopically depleted region of the mantle [e.g., *Geist et al.*, 1988; *Graham et al.*, 1993].

DISCUSSION

The above comparisons of predictions and observations at the Galápagos system as well as the scaling laws for W and x_{max} assume that the along-axis bathymetric, MBA, and

geochemical anomalies reflect directly the width of the plume in the mantle. This is likely the case if melt migration along the ridge axis is small or non-existent. If, however, along-axis melt migration is significant as suggested by *Ito et al.* [1996] for the Iceland-Mid-Atlantic Ridge system, then plume widths defined from geophysical or geochemical observations—which reflect largely the properties of the accumulated crust—are likely to be broader than the width of the plume in the mantle. If this is the case, then the same values of W and possibly x_{max} as examined here may require smaller values of Q than suggested by our scaling laws. The implication for the Galápagos system is that the Galápagos plume source may be hotter and narrower than what our models imply.

Additional complexities that may affect the systematics of along-axis plume width and x_{max} at plume-migrating ridge systems are ridge jumps and asymmetric plate spreading. Episodes in which the ridge jumps toward the neighboring plume has been documented for the Galápagos system [*Wilson and Hey*, 1995] as well as other systems in the southern ocean [*Small*, 1995]. Such episodes may result directly from plume-ridge interaction as the plume weakens the overlying plate near the ridge [*Small*, 1995]. Asymmetrically spreading ridges, which may also result directly from plume weakening of the lithosphere, are also common to plume-ridge systems [*Small*, 1995]. Factors such as these that affect the relative motion of the ridge are likely to have little affect on x_{max} when the ridge migrates toward the hotspot because in this case x_{max} is controlled by the stagnation point of the plume rather than motion of the ridge. On the other hand, ridge jumps and asymmetric spreading may increase x_{max} significantly when a ridge migrates away from the hotspot because in this case x_{max} is determined by the point at which the migrating ridge outruns the ridgeward spreading plume.

Regardless of how plume material is sampled by midocean ridges, our numerically derived scaling laws suggest that plumes affect broad regions of oceanic plates. In general, Eq. 14 and 15 suggest that the maximum along-axis width of a plume is 125-200% as broad as the maximum plume-ridge interaction distance. The major implication is that—as in the Atlantic and southern oceans with documented plume signatures at ridges located as far as 1400 km away—individual plumes may spread over distances of up to 2500 km perpendicular to the direction of plate motion. Such ridge-perpendicular spreading may generate broad bands of plume-affected lithosphere, which may alter otherwise normal lithosphere and contribute to characteristic properties of "tectonic corridors" such as those identified by *Kane and Hayes* [1992] and *Hayes and Kane* [1994]. Among the most prominent examples of plume affected lithosphere are the broad regions of anomalously

shallow seafloor associated with the Galápagos system as discussed in this study, the Iceland and Azores plumes in the North Atlantic, and the Tristan plume in the south Atlantic. Such a scenario implies that plumes are a major source of lithospheric accretion as proposed by *Morgan and Smith* [1992] and *Morgan et al.* [1995].

CONCLUSIONS

In our numerical investigations of steady-state stationary ridges, we have derived scaling laws consistent with those of [*Ribe*, 1996], indicating that they are insensitive to differences in numerical method or model boundary conditions. Plume width W and maximum plume ridge communication distance increase with the plume width scale $(Q/U)^{1/2}$ and modified plume buoyancy number $\Pi_b \gamma$. In the case of a migrating ridge, the distance of plume-ridge interaction is reduced when the ridge migrates toward the plume due to the excess drag of the leading plate. After the ridge passes over and migrates away from plume, the distance of plume-ridge interaction is enhanced due primarily to the reduced drag of the slower-moving trailing plate, and secondarily to the pattern of thermal erosion of the lithosphere.

To test our plume-ridge models we compare model predictions of along-isochron mantle-Bouguer and bathymetric anomalies with observations of the Galápagos plume-migrating ridge system. The models predict the amplitudes and widths of the observed anomalies with a plume source temperature anomaly of 80-120°C, radius of 80-100 km, and volume flux of 4.5×10^6 km^3/m.y. The models also predict the approximate increase in anomaly amplitudes with isochron age which reflects increased crustal production in the past when the ridge was closer to the Galápagos plume. Crustal production rates of the Galápagos Islands, as estimated from the observed island topography, are also matched reasonably well by model predictions. Predictions of the geochemical signature of the plume along the present-day ridge suggest that mixing between the plume OIB and ambient MORB source does not occur in the asthenosphere but instead most likely occurs deeper, possibly by entrainment of the depleted mantle as the plume ascends from its deep source region. These numerical models suggest that plumes may spread perpendicular to the direction of plate motion over distances 125-200% broader than the maximum distance to which they interact with ridges. Plumes may therefore comprise a significant percentage of the oceanic lithosphere.

REFERENCES

Christensen, U., Convection with pressure- and temperature-dependent non-Newtonian rheology, *Geophys. J. R. Astr. Soc, 77*, 343-384, 1984.

DeMets, C., R. G. Gordon, D. F. Argus, and S. Stein, Effect of recent revisions to the geomagnetic reversal time scale on estimates of current plate motions, *Geophys. Res. Lett., 21*, 2191-2194, 1994.

Feighner, M. A., L. H. Kellogg, and B. J. Travis, Numerical modeling of chemically buoyant mantle plumes at spreading ridges, *Geophys. Res. Lett., 22*, 715-718, 1995.

Feighner, M. A., and M. A. Richards, Lithospheric structure and compensation mechanisms of the Galápagos Archipelago, *J. Geophys. Res., 99*, 6711-6729, 1994.

Feighner, M. A., and M. A. Richards, The fluid dynamics of plume-ridge and plume-plate interactions: an experimental investigation, *Earth Planet. Sci. Lett., 129*, 171-182, 1995.

Gable, C. W., Numerical models of plate tectonics and mantle convection in three dimensions, *Ph.D. thesis*, Harvard University, Cambridge MA, 1989.

Gable, C. W., R. J. O'Connel, and B. J. Travis, Convection in three dimensions with surface plates: Generation of toroidal flow, *J. Geophys. Res., 96*, 8391-8405, 1991.

Geist, D. J., W. M. White, and A. R. McBirney, Plume-asthenosphere mixing beneath the Galapagos archipelago, *Nature, 333*, 657-660, 1988.

Graham, D. W., D. M. Christie, K. S. Harpp, and J. E. Lupton, Mantle plume Helium in submarine basalts from the Galápagos platform, *Science, 262*, 2023-2026, 1993.

Gripp, A. E., and R. G. Gordon, Current plate velocities relative to the hotspots incorporating the NUVEL-1 global plate motion model, *Geophys. Res. Lett., 17*, 1109-1112, 1990.

Hayes, D. E., and K. A. Kane, Long-lived mid-ocean ridge segmentation of the Pacific-Antarctic ridge and the Southeast Indian ridge, *J. Geophys. Res., 99*, 19,679-19,692, 1994.

Hey, R., Tectonic evolution of the Cocos-Nazca spreading center, *Geol. Soc. Am.Bull., 88*, 1404-1420, 1977.

Humphreys, E. D., and K. G. Dueker, Physical state of the western U.S. upper mantle, *J. Geophys. Res., 99*, 9635-9650, 1994.

Ito, G., and J. Lin, Mantle temperature anomalies along the present and paleoaxes of the Galápagos Spreading Center as inferred from gravity analyses, *J. Geophys. Res.*, *100*, 3733-3745, 1995a.

Ito, G., and J. Lin, Oceanic spreading center-hotspot interactions: Constraints from along-isochron bathymetric and gravity anomalies, *Geology*, *23*, 657-660, 1995b.

Ito, G., J. Lin, and C. W. Gable, Dynamics of mantle flow and melting at a ridge-centered hotspot: Iceland and the Mid-Atlantic Ridge, *Earth Planet. Sci. Lett.*, in press, 1996.

Kane, K. A., and D. E. Hayes, Tectonic corridors in the South Atlantic: Evidence for long-lived mid-ocean ridge segmentation, *J. Geophys. Res.*, *97*, 17,317-17,330, 1992.

Kincaid, C., G. Ito, and C. Gable, Laboratory investigation of the interaction of off-axis mantle plumes and spreading centres, *Nature*, *376*, 758-761, 1995a.

Kincaid, C., J.-G. Schilling, and C. Gable, The dynamics of off-axis plume-ridge interaction in the uppermost mantle, *Earth Planet. Sci. Lett.*, *137*, 29-43, 1995b.

Kuo, B.-Y., and D. W. Forsyth, Gravity anomalies of the ridge-transform system in the South Atlantic between 31° and 34.5°S: Upwelling centers and variations in crustal thickness, *Mar. Geophys. Res.*, *10*, 205-232, 1988.

Lin, J., G. M. Purdy, H. Schouten, J.-C. Sempéré, and C. Zervas, Evidence from gravity data for focused magmatic accretion along the Mid-Atlantic Ridge, *Nature*, *344*, 627-632, 1990.

McKenzie, D., and M. J. Bickle, The volume and composition of melt generated by extension of the lithosphere, *J. Petrol.*, *29*, 625-679, 1988.

Morgan, W. J., Rodriguez, Darwin, Amsterdam,..., A second type of hotspot island, *J. Geophys. Res.*, *83*, 5355-5360, 1978.

Oxburgh, E. R., and E. M. Parmentier, Compositional and density stratification in oceanic lithosphere—causes and consequences, *Geol. Soc. Lond.*, *133*, 343-355, 1977.

Phipps Morgan, J., W. J. Morgan, Y.-S. Zhang, and W. H. F. Smith, Observational hints for a plume-fed, suboceanic asthenosphere and its role in mantle convection, *J. Geophys. Res.*, *100*, 12753-12767, 1995.

Phipps Morgan, J., and W. H. F. Smith, Flattening of the sea-floor depth-age curve as a response to asthenospheric flow, *Nature*, *359*, 524-527, 1992.

Ribe, N., The dynamics of plume-ridge interaction 2. Off-ridge plumes, *J. Geophys. Res.*, *101*, 16,195-16,204, 1996.

Ribe, N., U. R. Christensen, and J. Theissing, The dynamics of plume-ridge interaction, 1: Ridge-centered plumes, *Earth Planet. Sci. Lett.*, *134*, 155-168, 1995.

Ribe, N. M., and U. R. Christensen, Three-dimensional modeling of plume-lithosphere interaction, *J. Geophys. Res.*, *99*, 669-682, 1994.

Schilling, J.-G., Iceland mantle plume: Geochemical study of Reykjanes Ridge, *Nature*, *242*, 565-571, 1973.

Schilling, J.-G., Upper mantle heterogeneities and dynamics, *Nature*, *314*, 62-67, 1985.

Schilling, J.-G., Fluxes and excess temperatures of mantle plumes inferred from their interaction with migrating mid-ocean ridges, *Nature*, *352*, 397-403, 1991.

Schilling, J.-G., R. N. Anderson, and P. Vogt, Rare earth, Fe and Ti variations along the Galapagos spreading centre, and their relationship to the Galapagos mantle plume, *Nature*, *261*, 108-113, 1976.

Schilling, J.-G., R. H. Kingsley, and J. D. Devine, Galapagos hot spot-spreading center system 1. Spatial petrological and geochemical variations (83°W-101°Wa), *J. Geophys. Res.*, *87*, 5593-5610, 1982.

Schilling, J.-G., G. Thompson, R. Kingsley, and S. Humphris, Hotspot-migrating ridge interaction in the South Atlantic, *Nature*, *313*, 187-191, 1985.

Sinton, C. W., D. M. Christie, and R. A. Duncan, Geochronology of the Galápagos seamounts, *J. Geophys. Res.*, *101*, 13,689-13,700, 1996.

Sleep, N. H., Lithospheric heating by mantle plumes, *Geophys. J. R. astr. Soc.*, *91*, 1-11, 1987.

Small, C., Observations of ridge-hotspot interactions in the Southern Ocean, *J. Geophys. Res.*, *100*, 17931-17946, 1995.

Travis, B., P. Olson, and G. Schubert, The transition from two-dimensional to three-dimensional planforms in infinite Prandtl number thermal convection, *J. Fluid Mech.*, *216*, 71-91, 1990.

Verma, S. P., and J.-G. Schilling, Galapagos hot spot-spreading center system 2. $^{87}Sr/^{86}Sr$ and large ion lithophile element variations (85°W-101°W), *J. Geophys. Res.*, *87*, 10,838-10,356, 1982.

Verma, S. P., J.-G. Schilling, and D. G. Waggoner, Neodymium isotopic evidence for Galapagos hotspot-spreading centre system evolution, *Nature*, *306*, 654-657, 1983.

Vogt, P. R., Asthenosphere motion recorded by the by the ocean floor south of Iceland, *Earth Planet. Sci. Lett.*, *13*, 153-160, 1971.

Wilson, D. S., and R. N. Hey, History of rift propagation and magnetization intensity for the Cocos-Nazca spreading center, *J. Geophys. Res.*, *100*, 10,041-10,056, 1995.

Wolfe, C., I. T. Bjarnason, J. C. VanDecar, and S. C. Solomon, The anatomy of a mantle plume: Seismic structure of the Iceland hotspot, *Nature* (submitted), 1996.

Table 1. Notation

Variable	Meaning	Value	Units
c_p	specific heat	1000	J kg^{-1} °C^{-1}
D	fluid depth	400	km
E	activation energy	1.9×10^5	J
g	acceleration of gravity	9.8	m/s^2
M	melt fraction		wt%
p	pressure		Pa
P	plume tracer concentration		
Q	volumetric plume flux		km^3/m.y.
Q_r	fraction of plume flux crossing the ridge		
R	gas constant	8.314	J K^{-1} mol^{-1}
S_o	characteristic plume thickness	$(48Q\eta_o/g\Delta\rho)^{1/4}$	km
ΔS	entropy change on melting	400	J kg^{-1} °C
T	mantle potential temperature		°C
T_R	mantle real temperature		K
ΔT_p	plume temperature anomaly		°C
$u\ (u,v,w)$	mantle flow rate vector		km/m.y.
U	ridge full spreading rate		km/m.y.
V	activation volume	4×10^{-6}	m^3
W	along-axis plume width		km
W_o	characteristic plume width	$(Q/U)^{1/2}$	km
x_p	plume-ridge distance		km
x_{max}	maximum distance of plume-ridge interaction		km
X	melt depletion		wt%
α	coefficient of thermal expansion	3.4×10^{-5}	K^{-1}
β	coefficient of depletion density reduction	0.024	
γ	η_o/η_p		
κ	thermal diffusivity	31	km^2/m.y.
η	viscosity		Pa s
η_o	reference viscosity		Pa s
η_p	plume viscosity at $0.5D$		Pa s
Π_b	buoyancy number	$Q\sigma/U^2$	
Π_u	upslope number	$Q^{1/8}\sigma^{3/8}\kappa^{1/2}/U$	
ρ	mantle density		kg/m^3
ρ_{max}	ridge crustal density closest to the plume	2900, 3000	kg/m^3
ρ_m	melt density	2900	kg/m^3
ρ_o	mantle reference density	3300	kg/m^3
σ	buoyancy scaling parameter	$g\Delta\rho/48\eta_o$	1/ms

118

Table 2. Experimental parameters and scaling quantities

Run	U'/U (km/my)	ΔT_p (°C)	γ	Π_b	Q'/Q (10^6 km^3/my)	W_o'/W_o (km)	$W'(x_p=0)/W(x_p=0)$ (km)
1	516 / 40	100	1.0	0.61	55 / 0.68	0.33 / 131	0.63 / 250
2	774 / 60	100	1.0	0.29	58 / 0.72	0.27 / 110	0.56 / 225
3	1290 / 100	100	1.0	0.12	64 / 0.79	0.22 / 89	0.50 / 200
4	386 / 30	200	1.0	3.97	100 / 1.24	0.51 / 203	1.00 / 400
5	744 / 60	200	1.0	1.04	105 / 1.30	0.37 / 147	0.75 / 300
6	1290 / 100	200	1.0	0.40	112 / 1.39	0.29 / 118	0.63 / 250
7	516 / 40	100	2.352	0.60	54 / 0.67	0.32 / 129	0.69 / 275
8	774 / 60	100	2.352	0.28	57 / 0.70	0.27 / 108	0.63 / 250
9	1290 / 100	100	2.352	0.11	61 / 0.75	0.22 / 87	0.50 / 200
10	386 / 30	200	5.053	3.13	157 / 1.95	0.64 / 255	1.65 / 660
11	774 / 60	200	5.053	1.25	126 / 1.56	0.40 / 161	0.94 / 375
12	1290 / 100	200	5.053	0.46	130 / 1.61	0.32 / 127	0.75 / 300

Primes denote dimensionless quantities and are listed adjacent to their scaled quantities. Input parameters are U, ΔT_p, and rheology law, which controlled γ. The remaining quantities are model output. Runs 4 and 10 had numerical box dimensions 3.2 D x 2.0 D x 1.0 D with 128 x 64 x 50 grids in x, y, and z respectively. The other runs had box dimensions 3.2 D x 1.0 D x 1.0 D with 128 x 32 x 50 grids in x, y, and z respectively. Rayleigh number was 1.83 x 10^6 based on T_o = 1300 °C and η_o = 5 x 10^{19} Pa s.

Figure 1. Perspective diagram illustrating steady-state flow (small arrows) and potential temperature fields (contoured at 50°C-intervals for $T > 1300$°C and 100°C intervals for $T < 1300$ °C) of an example calculation with $\Delta T_p = 100$°C and $U = 60$ km/m.y. (experiment 7, Table 2). The ridge axis is located at $x = 320$ km, the plume source is centered at $x = 450$ km. The maximum vertical velocity is 115 km/my. Both top ($z = 0$) and bottom ($z = D$) boundaries are isothermal planes with the bottom, a free slip boundary and the top, fixed at a horizontal velocity of $U/2$ (large horizontal arrow) at $x > 320$ km and $-U/2$ at $x < 320$ km. All boundaries are closed to flow both in and out of the numerical box, thus material flows downward at the ends of the box and recirculates toward the ridge axis along the base of the box. The effect of this recirculation on the interaction between plume and ridge are insignificant. Note the cooling lithosphere which slopes towards the ridge axis.
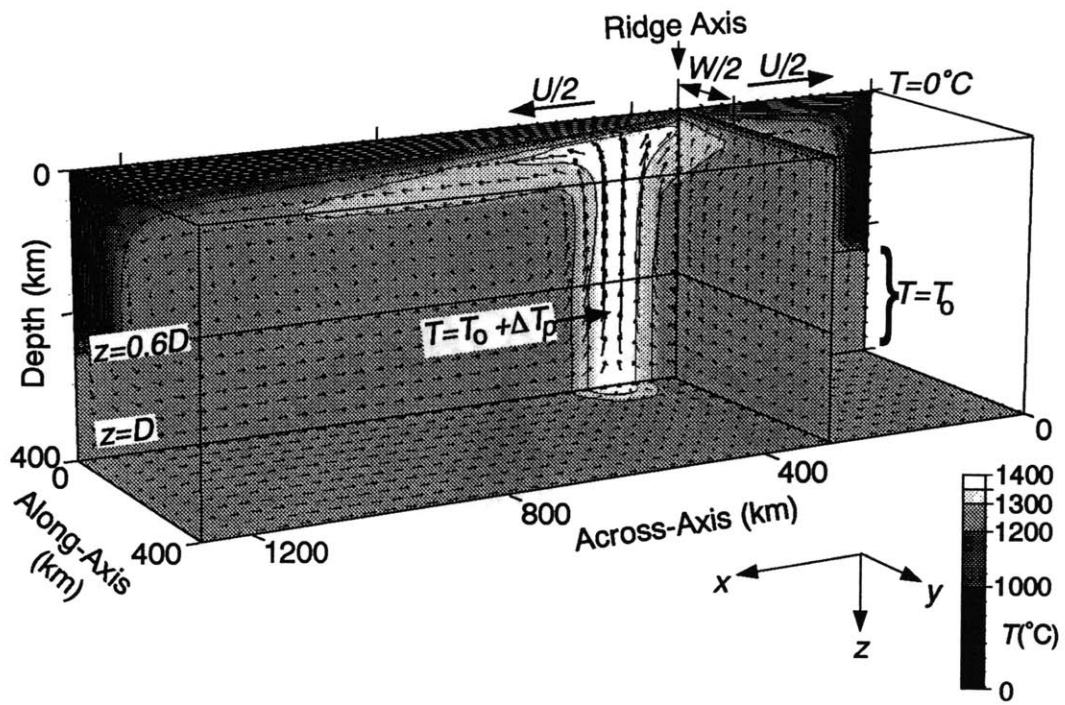
Figure 1

Figure 2. Model predictions of scaled along-axis width versus modified buoyancy number $\Pi_b\gamma$. Open circles are for runs with $\gamma = 1.0$ and temperature anomalies 100 and 200°C. Gray circles are for fully pressure- and temperature-dependent plume viscosity calculations with $\gamma = 2.35$ and $\Delta T_p = 100$°C, and black circles are for temperature-dependent plume viscosity calculations with $\gamma = 5.05$ and $\Delta T_p = 200$°C. The curve is the best fitting scaling law described by Eq. 6.
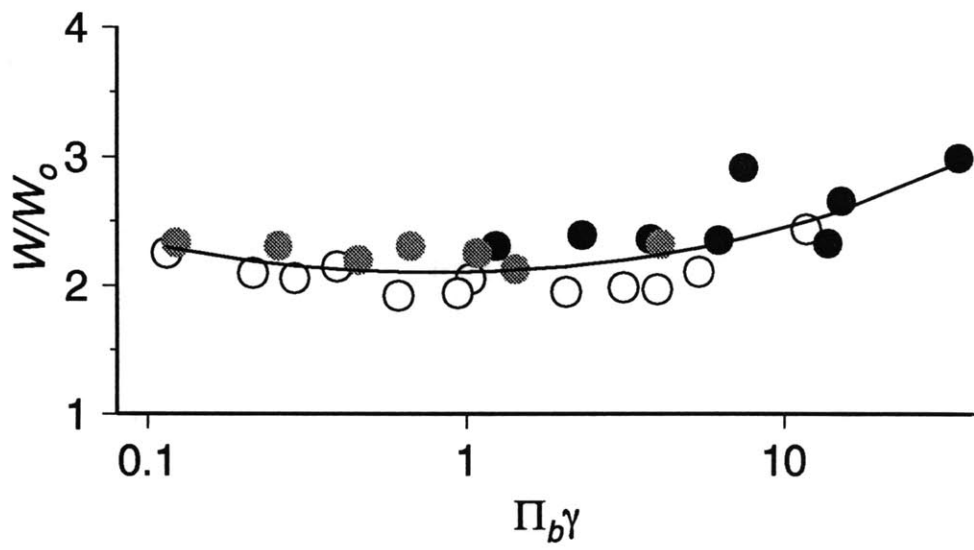
Figure 2

Figure 3. Steady state isosurface of plume tracer, $P = 0.4$, as viewed from the bottom of the box looking upward (shading denotes illumination from the right of the figure). Small arrows illustrate horizontal velocities in the horizontal plane at $z = 64$ km. The ridge axis is marked by the bold line. Experimental conditions are those of experiment 7, the same as in Fig. 1. a) $x_p = 0$, b) $x_p = 100$, c) $x_p = 150$. Note that the width of the plume at the ridge axis decreases with increasing x_p. The maximum distance to which the plume reaches the ridge is $x_p = 150$.
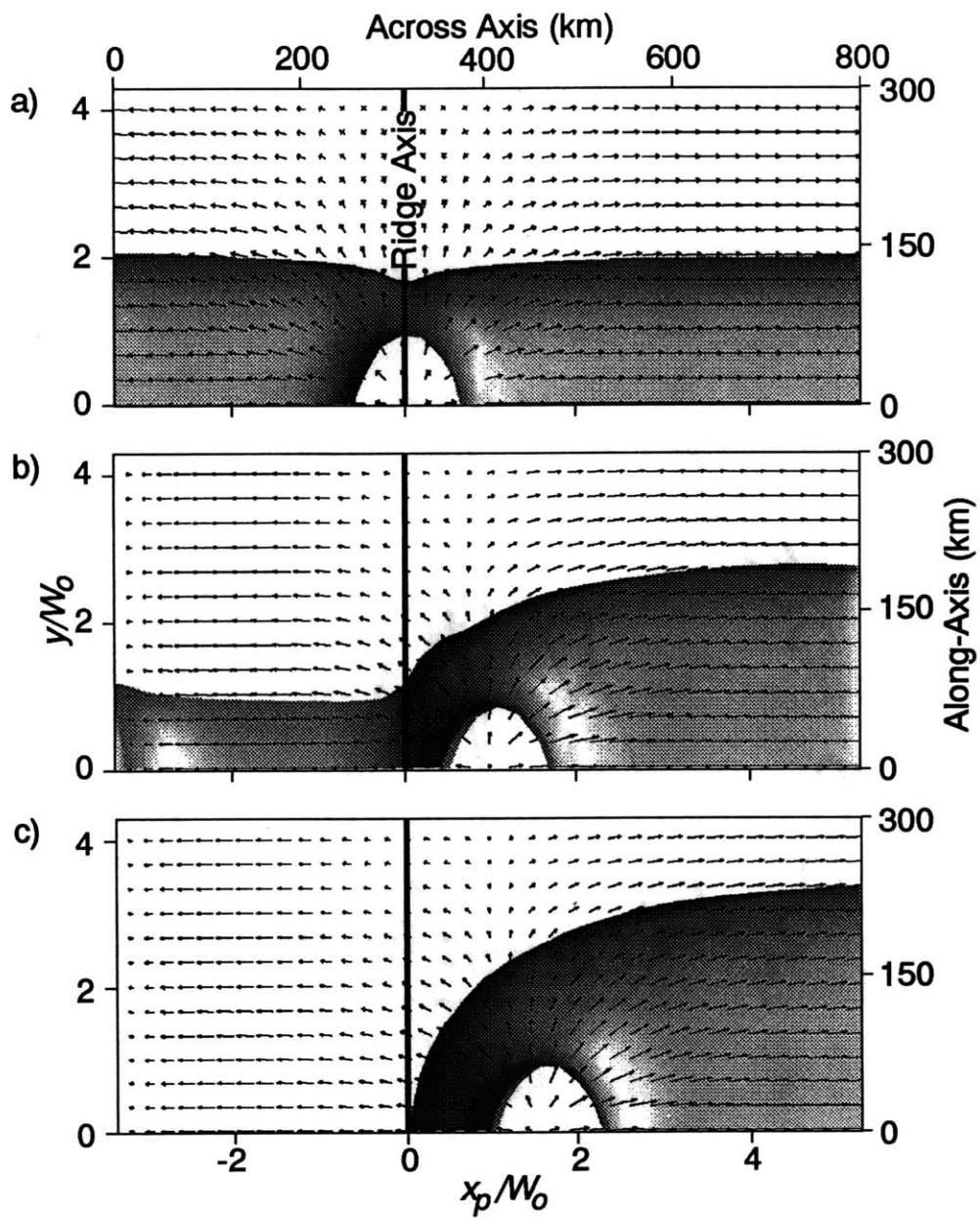
Figure 3

Figure 4. Numerical results of along-axis plume width (scaled by width for $x_p = 0$) versus scaled plume-ridge distance. As in Fig. 2 open circles are for runs with $\gamma = 1.0$, gray circles are for $\gamma = 2.35$, black circles are for $\gamma = 5.05$. (a) The best fitting polynomials of the form given in Eq. 7 are shown for $\gamma = 1.0$ (solid), $\gamma = 2.35$ (dashed), and $\gamma = 5.05$ (dotted). The different widths of the curves illustrate the dependence of F_2 on γ. (b) Same as in (a) but including F_2 (Eq. 8) which collapses the points onto to a single curve. The standard deviation misfit of Eq 8 to the numerical results is 0.13. The mismatch to the numerical points for $x_p/(W_o F_2) \leq {\sim} 1.0$ may suggest a dependence on higher order terms of x_p which we chose not attempt to resolve.
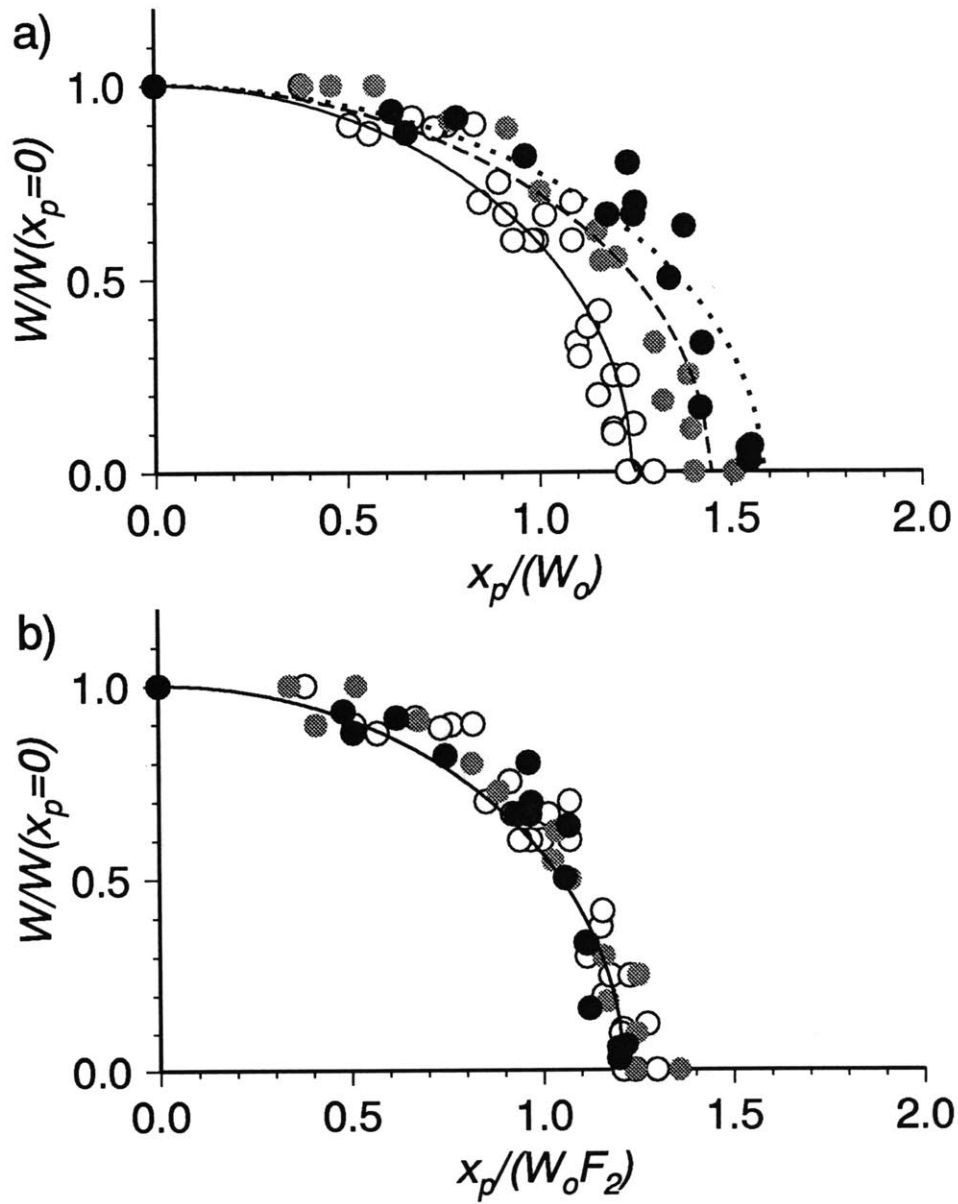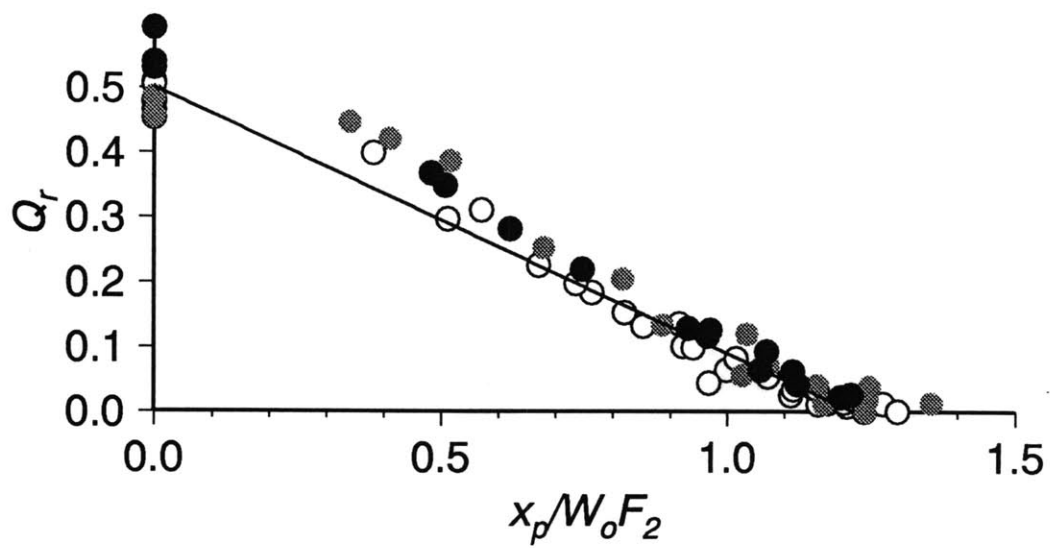
Figure 4

Figure 5. Dependence of the ratio of plume volume flux crossing the ridge Q_r versus scaled plume ridge distance divided by stretching function F_2. Symbols are the same as in Fig. 2. The solid line is the best fitting line of Eq. 9 with a standard deviation misfit of 0.08. The mismatch to the numerical points for $x_p/(W_oF_2) \leq \sim 0.7$ may suggest a dependence on higher order terms of x_p which we chose not attempt to resolve.

Figure 5

Figure 6. Contours of lithospheric erosional thickness are normalized by characteristic plume thickness $S_o \gamma^{-1/4} = 128$ km for experiment 7 (same as Fig 3c). The ridge axis is marked by the shaded vertical line and the plume source is shown as the gray semicircle at $x_p = 150$. The thickness of the lithospheric rheological boundary layer is defined as the depths over which $\eta/\eta_o \geq 10$. Erosional thickness is the difference between the boundary-layer thickness above the plume and that of normal lithosphere as defined along the ridge-perpendicular profile at $y = 1.0D$.

Figure 6

131
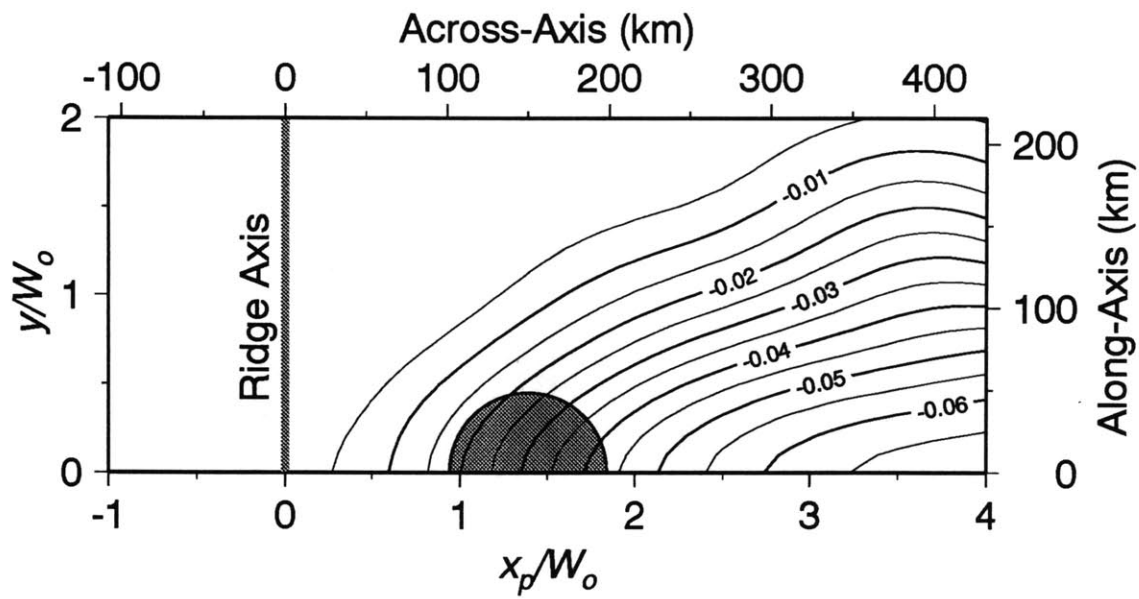
Figure 7. Temperature fields (contoured at 50 °C intervals in the plume and at 100°C intervals in the lithosphere) and velocities (arrows) in across-axis, depth cross-sections through the center of the plume source ($y = 0$). Experimental parameters are the same as in Fig 1. (experiment 7) but the ridge is migrating in the positive x_p-direction at the half spreading rate of 30 km/m.y. (a) Ridge is migrating toward the plume therefore the plume is beneath the faster moving Plate 1. (b) Ridge is migrating away from the plume therefore the plume is beneath the stationary Plate 2.
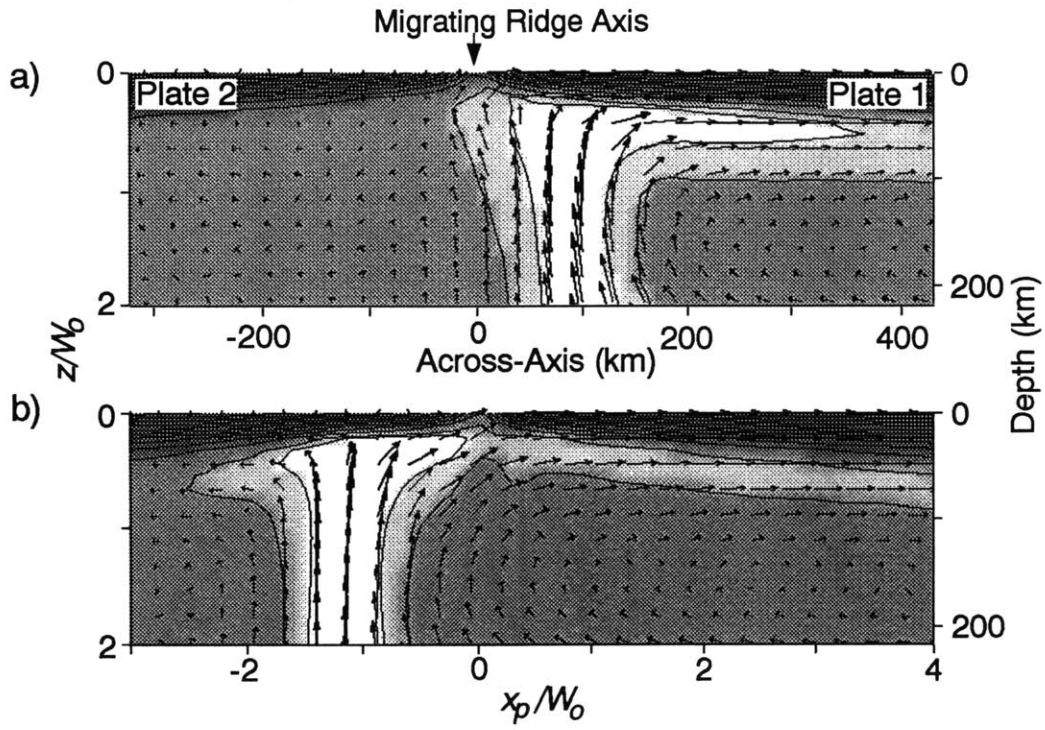
Figure 7

Figure 8. Numerical results of scaled along-axis width versus scaled plume-ridge distance for migrating ridge cases of experiment 7 with $U/2=$ 30 km/m.y. The bold curve as defined in Eq. 7 is that predicted for steady state conditions with a stationary ridge. Open triangles are for $V_r =$ 10 km/m.y. shown with best fitting (solid) curve of the form in Eq. 11; gray triangles are for $V_r =$ 20 km/m.y. shown with best fitting (dotted) curve; solid triangles are for $V_r =$ 30 km/m.y. shown with best fitting (dashed) curve. Mismatches are largest near the apexes of the curves and are due in part to difficulty in resolving curvature where slope in W is small, and to a possible dependence on higher order terms of x_p which we chose not consider.
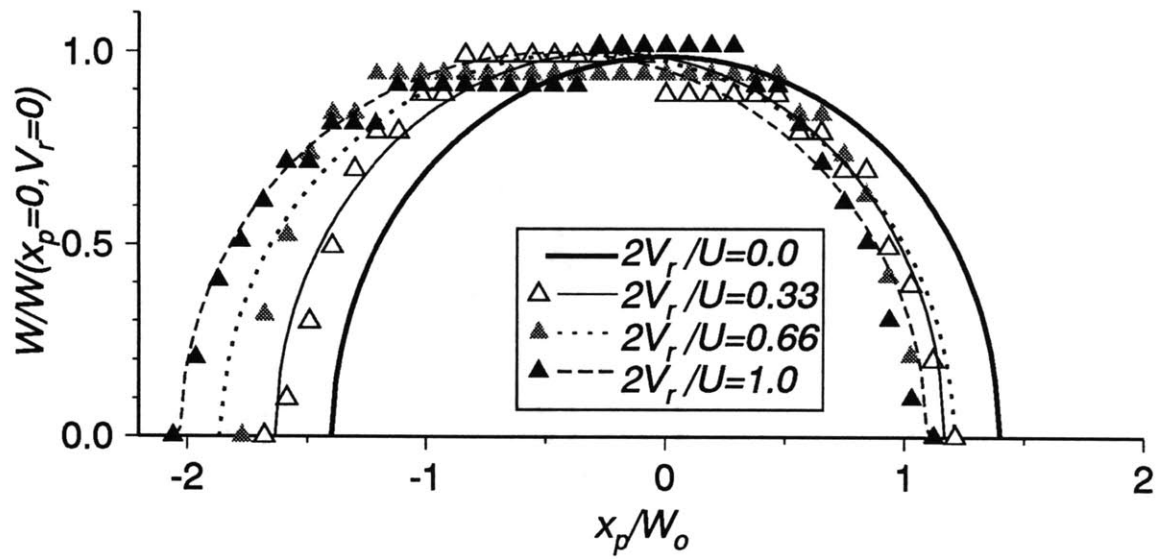
Figure 8

Figure 9. (a) Numerical results showing the dependence of F_5 on $\Pi_b\gamma$ and scaled ridge migration rate. Open circles are for runs with $\gamma = 1.0$, gray circles are for $\gamma = 2.35$, black circles are for $\gamma = 5.05$. The line is the best fitting function of Eq. 12. (b) Numerical results showing the dependence of F_6 on $\Pi_b\gamma$ and scaled ridge migration rate. Circles are patterned as in (a). The curve is the best fitting function of Eq. 13.
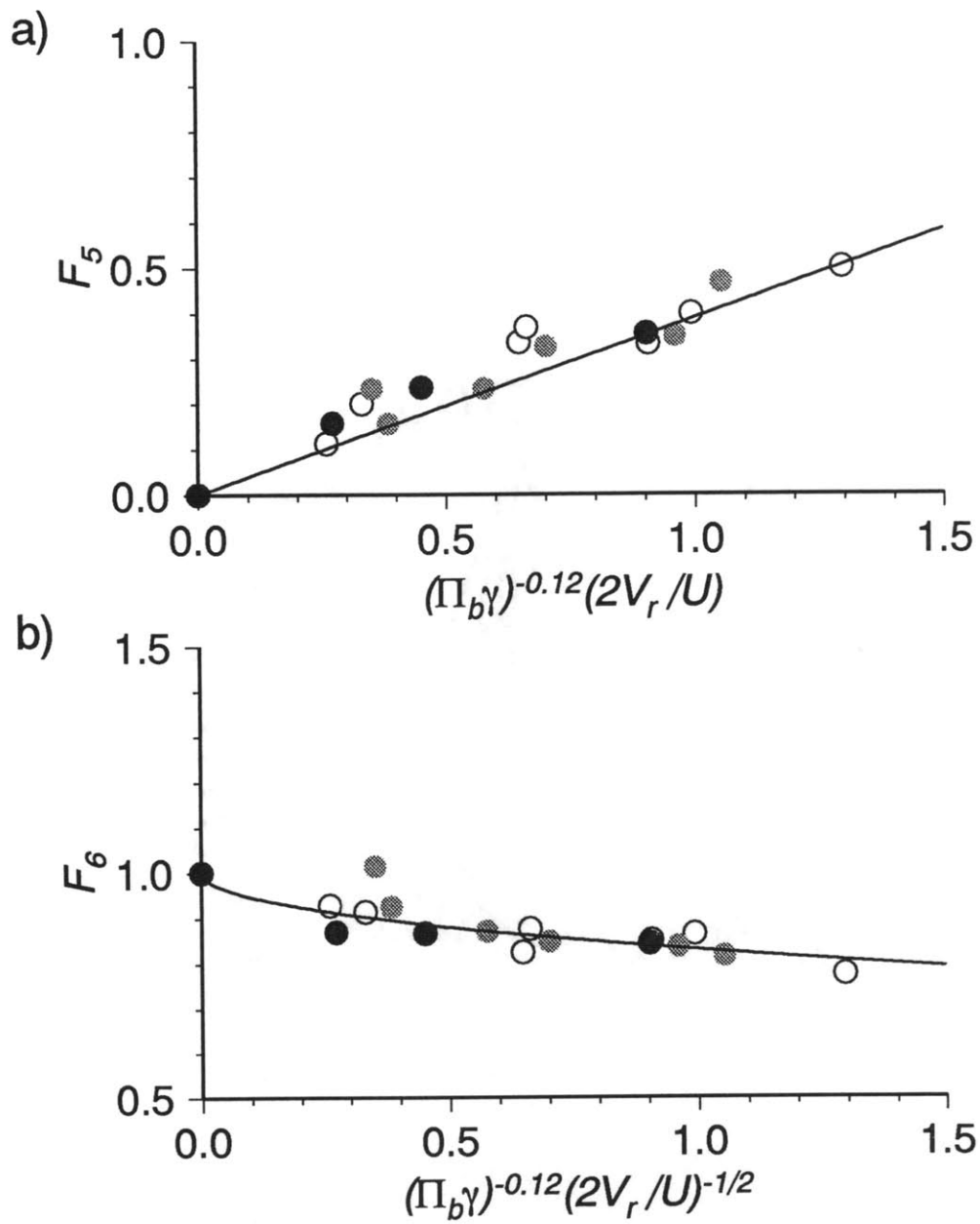
a) with vertical axis F_5 from 0.0 to 1.0, horizontal axis $(\Pi_b\gamma)^{-0.12}(2V_r/U)$ from 0.0 to 1.5

b) with vertical axis F_6 from 0.5 to 1.5, horizontal axis $(\Pi_b\gamma)^{-0.12}(2V_r/U)^{-1/2}$ from 0.0 to 1.5

Figure 9

Figure 10. Contours of lithospheric erosion thickness normalized by characteristic plume thickness $S_o\gamma^{-1/4} = 120$ km for the migrating ridge cases of experiment 7 with $U = 30$ km/m.y. The plume source (shaded) is now at $x_p = -170$ km beneath the slower moving Plate 2. (a) The region of erosion is broadest for the case where $V_r = 10$ km/m.y. The area of erosion becomes more confined to the plume source with increasing ridge migration rates (b) $V_r = 20$ km/m.y. and (c) $V_r = 30$ km/m.y.
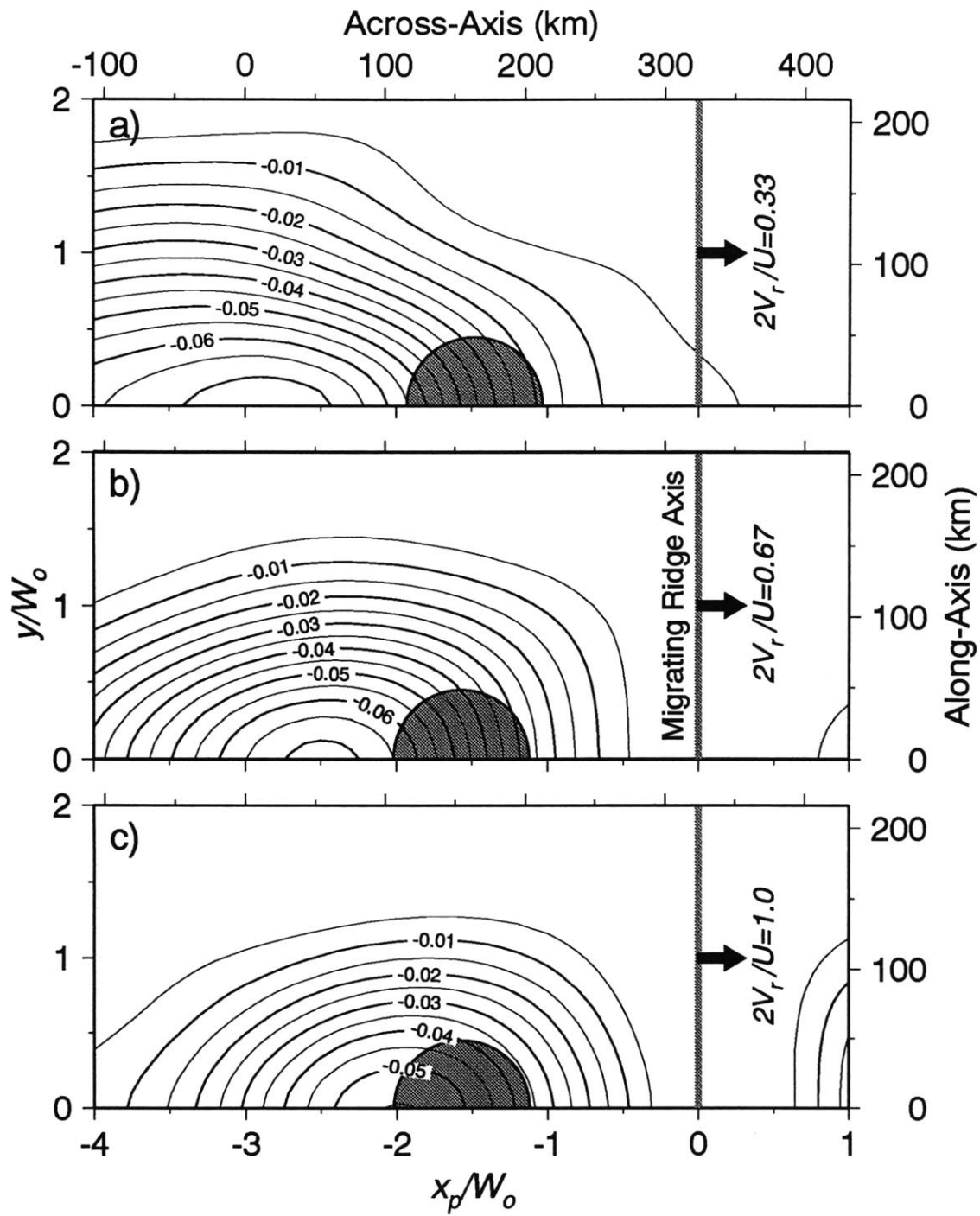
Figure 10

Figure 11. Map of the regional bathymetry of the Galápagos plume-ridge system (shipboard and Etopo5 bathymetry from *Ito and Lin* [1995a]). The present-day ridge axis is the southern-most set of white lines, and the isochrons of *Ito and Lin* [1995a] (taken from *Wilson and Hey* [1995]) are shown to the north on the Cocos Plate. The plume center is taken to be the eastern-most island Fernandina as shown by the circle of radius 100 km. The dashed box shows the region of bathymetry used to calculate the crustal volume flux of the archipelago.
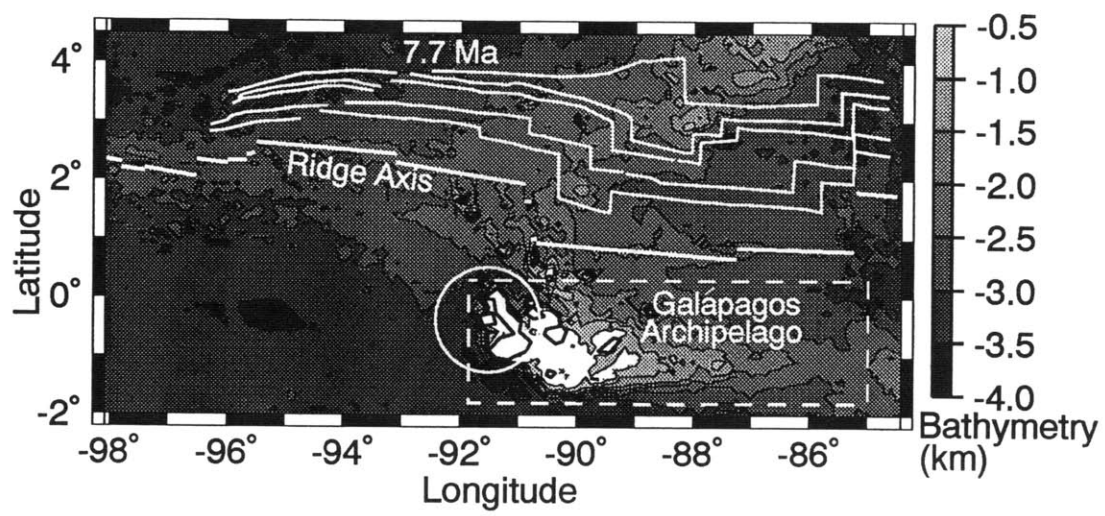
Figure 11

Figure 12. Comparisons between observed (thick gray) and predicted along-isochron, bathymetric profiles from model 1 (solid) and model 2 (dashed). Model profiles are the combined isostatic topography of axial crustal thickness and mantle density variations. Maximum values of crustal thickness predicted by models 1 and 2 are labeled as $\Delta Cr_{1,2}$.
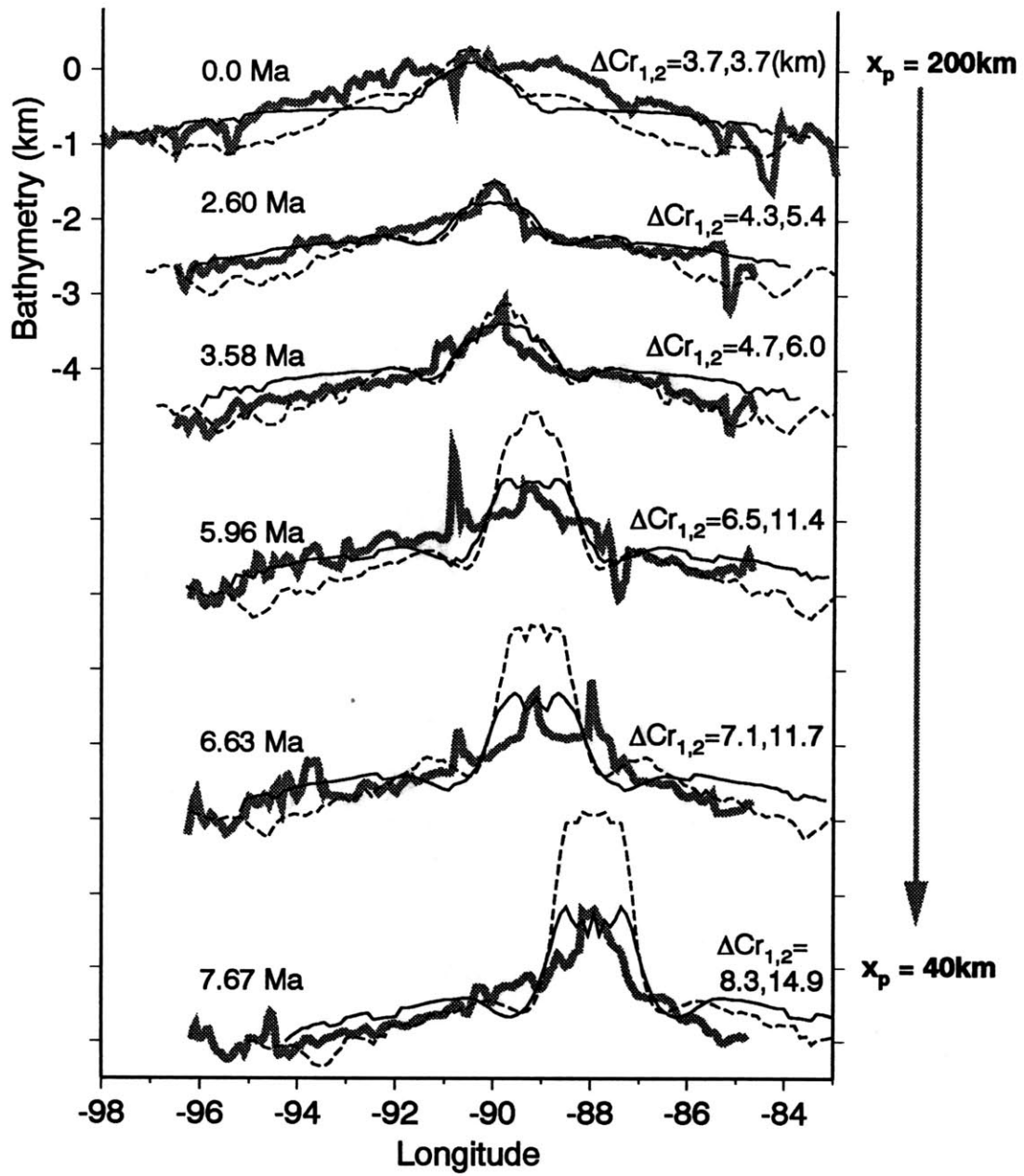
Figure 12

Figure 13. Comparisons between observed (thick gray) and predicted along-isochron, MBA profiles from model 1 (solid) and model 2 (dashed).
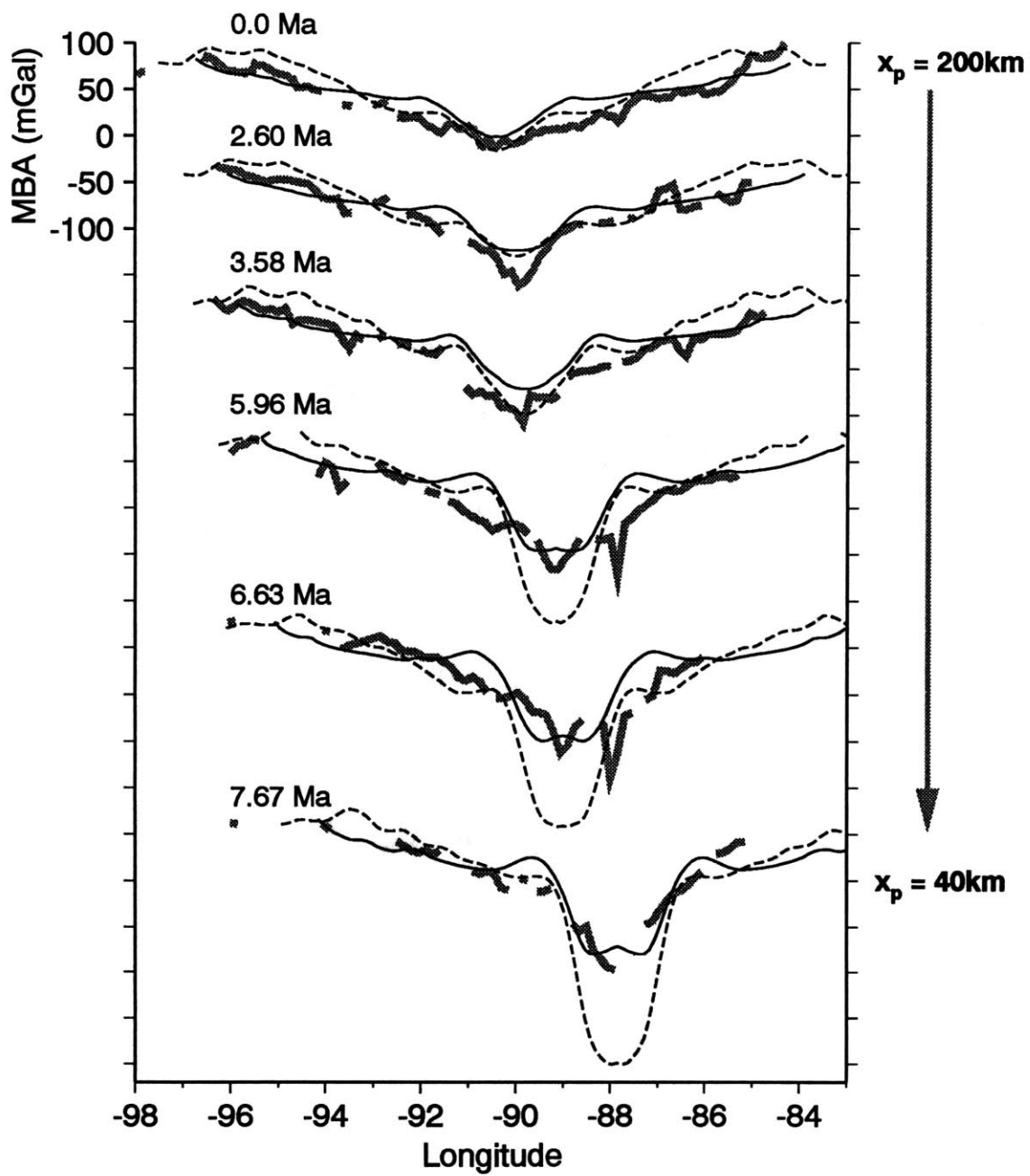
Figure 13

145

Figure 14. Total amplitude of along-isochron (a) bathymetry and (b) MBA variations are plotted versus isochron age. Thick gray lines are observed variations, solid lines are variations predicted by model 1, and dashed lines are variations predicted by model 2. The pairs of model curves are those assuming a crustal density of 2900 kg/m^3 (upper-bound) and 3000 kg/m^3 (lower-bound) at the point of the ridge closest to the plume (91°W). (c) Crustal volume flux of the Galápagos Archipelago versus age as predicted from model 1 (solid) and model 2 (dashed) is compared with crustal volume fluxes calculated by assuming isostatic compensation of the island topography (solid gray) (see text). The upper-bound gray curve is that assuming a crustal density of 3000 kg/m^3 and the lower-bound curve is that assuming a crustal density of 2900 kg/m^3.
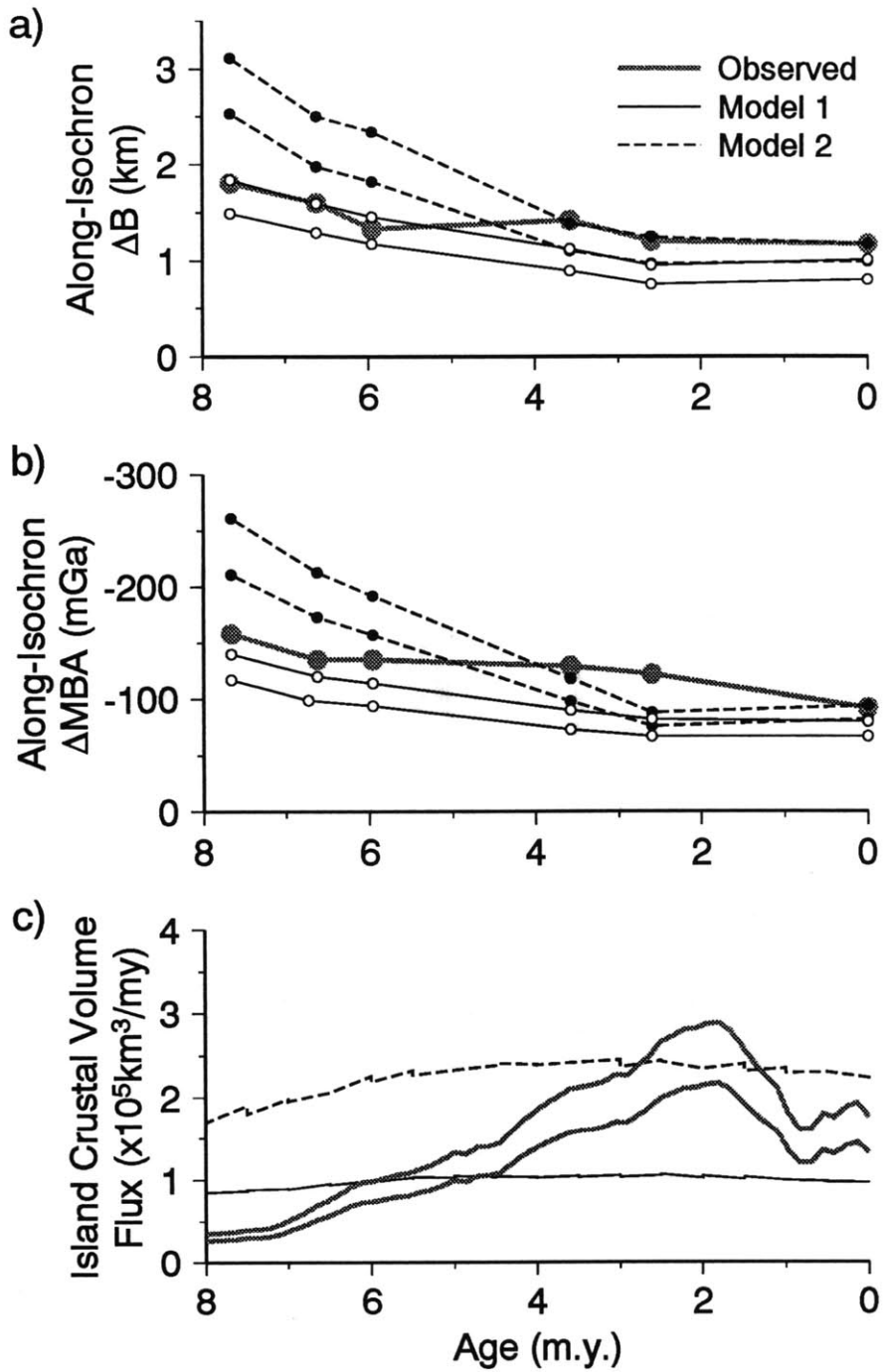
Figure 14

Figure 15. Observed variations (dots) in $[La/Sm]_{ef}$ from *Schilling et al.* [1982] is compared with accumulated concentration of plume tracer along the ridge (Eq. 19) for model 1 (solid) and model 2 (gray).
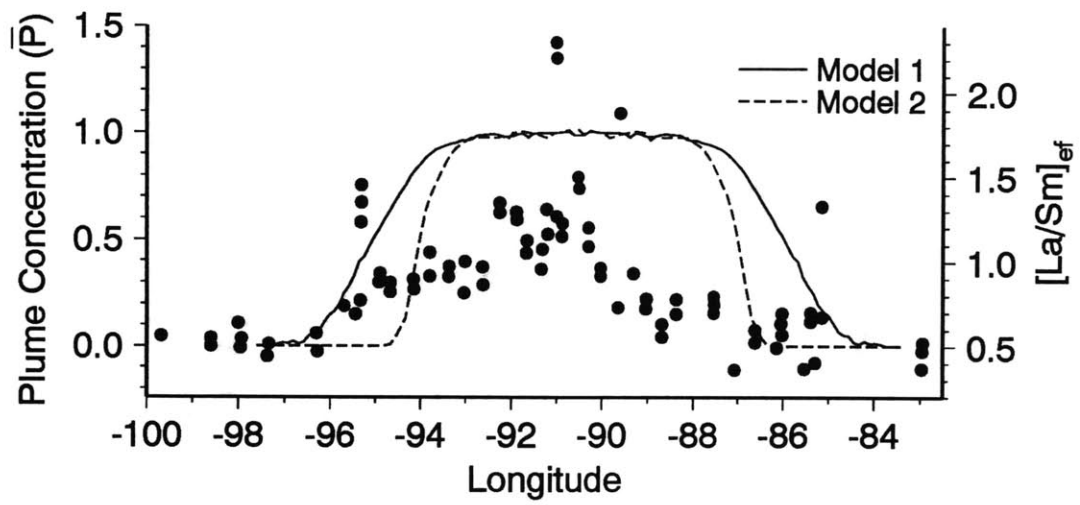
Figure 15

CONCLUSIONS

Bathymetric and gravity observations at five prominent plume-ridge systems reveal broad wavelength anomalies that reflect anomalously low density subsurface structure imposed by the near-ridge plumes. Along-axis bathymetry shallows by as much as 4.5 km toward the plumes while along-axis mantle-Bouguer anomalies become increasingly negative by as much as -300 mGal toward the plumes. We estimate that ~70% of the anomaly amplitudes are due to thickened axial crust with the remaining ~30% due to anomalously low density mantle, both of which are caused by anomalously hot mantle temperatures imposed by the near-ridge plumes.

The amplitudes of along-isochron MBA and bathymetric anomalies are largest at the ridge-centered Iceland-Mid-Atlantic Ridge (MAR) system and at the ridge-centered cases of the Tristan-MAR system. The anomaly amplitudes decrease with increasing plume-ridge distance most likely reflecting reduced crustal production as the ridges migrated away from the plumes. At a plume-ridge distance of ~500 km the available data at the Tristan-MAR system show no discernable anomalies suggesting a maximum distance that these plumes affect ridge structure significantly. Residual bathymetric anomaly widths along the isochrons, however, appear to be most sensitive to spreading rate and decrease with increasing spreading rate from 2700 km at the slow spreading Iceland-MAR system, to < 500 km at the fast spreading Easter-EPR system.

While the above studies place constraints on the amplitude and extent of plume-imposed subsurface density anomalies, our numerical modeling studies examine the possible causes of such anomalies. Numerical models of ridge-centered plumes indicate that along-axis plume width W scales with plume volume flux Q, ridge full spreading rate U, ambient/plume viscosity ratio γ, and buoyancy number Π_b according to $W = 2.37(Q/U)^{1/2}(\Pi_b \gamma)^{0.04}$. Thermal buoyancy is the most important driving force while melting effects of latent heat loss, depletion buoyancy, and melt-retention buoyancy yield competing effects which do not change the above scaling argument. Numerical simulations of the Iceland-MAR system suggest two end-member source models. The first model has a source radius of 300 km, temperature anomaly of 75°C, and volume flux of 1.2×10^7 km^3/m.y., while the second has a source radius of 60 km, temperature anomaly of 170°C, and volume flux of 2.1×10^6 km^3/m.y. The first model explains well the observed crustal thickness, bathymetric, and MBA variations along the MAR and Iceland, but the second model requires substantial along-axis melt transport in order to explain the observations.

This second model may be more representative of the Iceland plume based on similarities between predicted and observed mantle P-wave anomalies.

For off-axis plumes, along-axis width scales again with $(Q/U)^{1/2}$ and $\Pi_b\,\gamma$, in a similar manner to the ridge-centered plume case. For steady-state plumes near stationary midocean ridges W decreases with increasing plume-ridge distance and becomes zero at a maximum plume-ridge interaction distance x_{max}, which increases with $(Q/U)^{1/2}$ and $\Pi_b\,\gamma$. When ridges migrate toward plumes, however, predicted values of W and x_{max} are reduced relative to the case of a stationary ridge by as ~24% due to the enhanced drag of the overlying plate that leads the migrating ridge. On the other hand, when ridges migrate away from plumes, W and x_{max} are predicted to increase by ~36% due to reduced drag of the trailing plate; enhanced erosion of the lithosphere also enhances W and x_{max} but to a degree that is secondary to the effects of reduced plate shearing. Numerical models of the Galápagos plume-ridge system predict MBA and bathymetric anomalies that match successfully the amplitudes and widths of the observed anomalies, as well as the increase in anomaly amplitude with isochron age. The implied Galápagos plume source has of radius 80-100 km and temperature anomaly of 80–120°C. In addition, predicted chemical signatures of the plume along the model ridge suggest that mixing between the plume and ambient mantle occurs deeper than the asthenosphere, most likely due to entrainment of the ambient mantle as the plume ascends from its deep source reservoir.

Thus for a few prominent plume-ridge systems, we have begun to quantify the influence of near-ridge plumes on ridge crustal and mantle density structure. The suggestion that subsurface structure along seafloor isochrons reflects past interaction between plumes and ridges warrants further investigations to test, in the form of land-based data analyses as well as sea going geophysical and geochemical surveys. In addition, we have learned a great deal about how mantle flow might behave at plume-ridge systems. Our models also require further studies to test, most likely with mantle seismological studies. Finally, as we have discussed for the Iceland-MAR system, along-axis melt transport may be a first-order process for this and possibly other plume-ridge systems. If this is the case, it may be time to re-examine our established ideas of plume-ridge interaction and possibly crustal accretionary processes at ridges in general.

APPENDIX

LABORATORY INVESTIGATION OF THE INTERACTION OF OFF-AXIS MANTLE PLUMES AND SPREADING CENTRES

Laboratory investigation of the interaction of off-axis mantle plumes and spreading centres

C. Kincaid*, G. Ito† & C. Gable‡

* Graduate School of Oceanography, University of Rhode Island, Narragansett, Rhode Island 02882, USA
† MIT/WHOI Joint Program in Oceanography, Woods Hole Oceanographic Institution, Woods Hole, Massachusetts 02543, USA
‡ Earth and Environmental Sciences, Los Alamos National Laboratory, Los Alamos, New Mexico 87545, USA

MANTLE plumes and mid-ocean ridge spreading centres are the dominant phenomena through which mass and heat are transported from the mantle to the Earth's surface. It now seems that the dispersion of near-ridge plumes beneath the lithosphere is modulated strongly by mid-ocean ridges; in particular, geochemical and geophysical observations have suggested that rising plumes are diverted towards and feed nearby ridges[1-7]. Here we confirm the feasibility of this model with laboratory experiments that incorpor-
ate the essential physical and fluid dynamic aspects of a plume–ridge upper mantle system. Our results indicate that an off-axis plume may communicate thermally and chemically with a spreading ridge through a narrow, sub-horizontal conduit instead of a broader, radially spreading plume head. A necessary condition for this communication is the presence of a lithospheric or rheological boundary layer that thickens away from the ridge axis owing to conductive cooling. Interestingly, we find that for high plume temperatures, increasing the plume thermal buoyancy may inhibit rather than enhance plume–ridge interaction, as a result of increased erosion of the overlying lithosphere.

Recent laboratory[8] and numerical experiments[9] have considered the dynamics of plume–ridge interaction for the ridge-centred case; however, the difficult question remains as to how a plume and a ridge interact thermally, chemically and dynamically when the plume is located off axis. A model of sub-horizontal pipe-like flow from the off-axis plumes to a ridge axis along the base of the rigid lithosphere has been suggested[2] (Fig. 1a). Geochemical studies[10-16] and two-dimensional numerical experiments[17-19] support this channel-flow model and suggest that geochemical communication may persist over long periods of time and plume–ridge separation distances as high as 1,200 km (ref. 16). This laboratory experimental project is the first fully three-
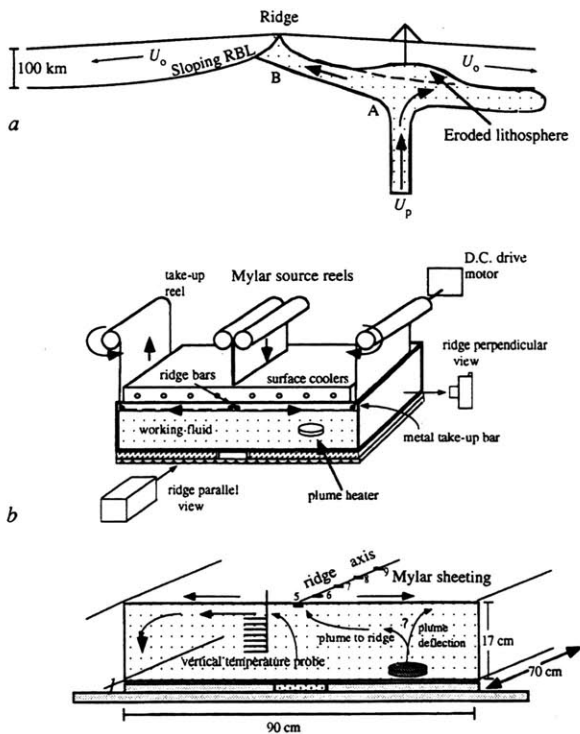

FIG. 1 a, This diagram illustrates the conceptual model that near-ridge plumes rise and then flow toward ridges along the base of the RBL from A to B (ref. 16). U_p is vertical velocity within the plume conduit. b, Diagram of experimental apparatus. Mylar sheeting is pulled along the fluid surface to simulate plate spreading. From source reels, the Mylar is threaded through two bars at the spreading axis and at the tank edges (take-up bars) to ensure contact between sheeting and working fluid. Mylar is then pulled around take-up bars by a synchronous high-torque d.c. motor. The fluid surface is cooled by circulating fluid from a refrigerated cold bath through a series of (70 cm × 10 cm × 2 cm) metal jackets suspended 2 mm above the fluid. Tank sidewalls and fluid surface are insulated. Plume flow is monitored with shadowgraph and time-lapse laser photographs from ridge-perpendicular and ridge-parallel viewpoints. Working fluid viscosity follows an Arrhenius-type law of the form $\mu = \exp[(1,888/(T+93.3))-11.48]$, where T is temperature in °C and μ is viscosity (in Pa s). c, This close-up slice through the tank centre illustrates the configuration of the ridge axis and plume source. Arrows illustrate hypothetical fluid flow. Nine RTDs are positioned at 5-cm intervals along the ridge axis to monitor axial temperature variability (note that ridge RTD 5 lies on an orthogonal line from the plume source). Before running experiments, we allow the fluid to equilibrate for several days at room temperature, ~20 °C. We then establish large-scale plate-driven flow by running the Mylar drives for 60 min before heating the plume source. In experiments 2 and 4, surface coolers are maintained at 10 °C for 60 min to produce an RBL before activating the Mylar; in experiment 3, coolers are maintained at 0 °C for 120 min before activating the Mylar. Experiments run for 150–280 min, depending on whether or not there is surface cooling.

Ridge Parallel   Ridge Perpendicular

FIG. 2 Shadowgraph photographs at three instants during experiment 1. Variations in fluid-temperature gradients focus the illuminating light to yield a bright halo at the top of the plume head (beneath black curves). a, 31 min after turning on the disc heater, the plume has separated from the source at the base of the tank, generating a single plume' characterized by a broad leading head (~6 cm across) and a narrow trailing conduit (~1.8 cm wide). b, At 41 min, the plume begins impinging upon the fluid surface. The maximum ridgeward deflection due to the plate-driven return flow is ~2.2 cm, or roughly a conduit width. The ascent rate of the plume head is ~0.8 cm min^{-1}, or close to twice the plate speed. Fluid velocity in the conduit exceeds 3 cm min^{-1} as measured by tracking neutrally buoyant Delrin beads (not shown) released periodically at the plume source. c, At 72 min, the plume head has stalled and flattened; head and conduit are being sheared away from the ridge near the fluid surface.
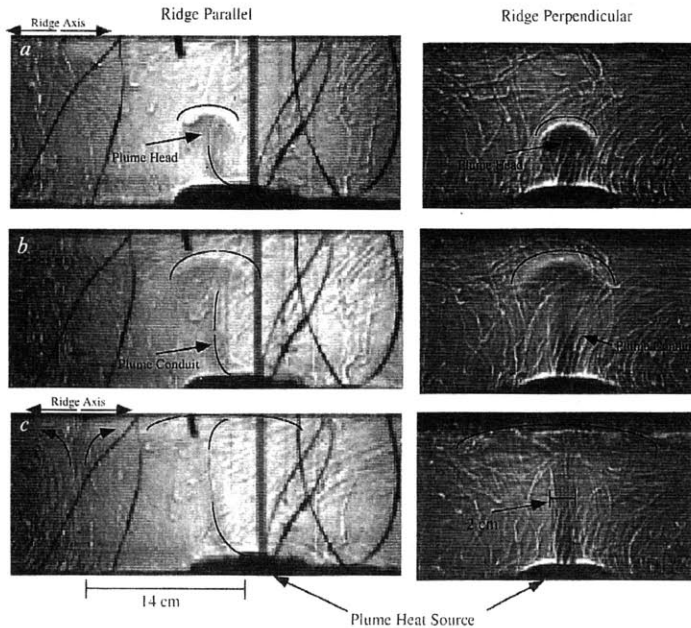
dimensional variable-viscosity study of this problem, and it exposes the mechanisms by which an off-axis plume overcomes the lithospheric drag that draws material away from a ridge, to successfully feed the nearby spreading centre.

To test the conceptual model of plume–ridge channelling (Fig. 1a), we simulate a plume–ridge, upper mantle system with a tank of a concentrated sucrose solution which, like the Earth's mantle, is strongly temperature dependent (Fig. 1b). Plate-driven mantle flow is simulated by dragging two Mylar sheets in opposite directions on the surface of the fluid at a constant rate of 0.35 cm min^{-1} (U_o, half-spreading rate). Buoyantly driven flow is produced through a supply of thermal energy from a disc-shaped resistance heater (that is, the plume source) positioned at the base of the tank. The two parameters we vary are the

surface temperature, thus the thickness/age of the upper rheological boundary layer (RBL), and the plume source temperature, controlling the strength of the rising plume. Fluid temperature is continuously monitored at the disc heater, at the surface of the Mylar, along a vertical profile within the fluid, and along the ridge axis with resistance temperature detectors (RTDs) (Fig. 1c).

Plume buoyancy is caused by density reduction of the plume fluid due to thermal expansion according to

$$\Delta\rho = (\rho_o - \rho_p) = \alpha\rho_o(T_p - T_o) \qquad (1)$$

where α is the expansion coefficient (4.6×10^{-4}), and ρ_o, T_o and ρ_p, T_p are reference and plume densities and temperatures,

TABLE 1   Plume–ridge experiments

(a) Parameters

Exp. no.	Surface temp. contrast from ambient of 20 °C (°C)	RBL slope (deg)	Plume source temp. contrast from ambient (°C)	Plume density contrast, $\Delta\rho/\rho_o$ (%)	Mean plume conduit viscosity, μ_p (Pa s)	Plume buoyancy number, B_n	Plume buoy. flux to ridge*, B_r/B_s (%)
1	0	**0**	40	1.8	4.9	52	0
2	−6	**1**	**40**	1.8	4.9	52	3
3	−10	**3**	40	1.8	4.9	52	10
4	−6	1	**48**	2.2	2.5	60	0

(b) Comparison of laboratory and expected mantle parameter ranges

	μ_L/μ_o	μ_o/μ_p	$\Delta\rho/\rho_o$ (%)	B_n	Pe_p	Pe_p/Pe
Laboratory	10	50–100	1.8–2.2	50–60	1,750–2,500	10
Mantle	>10⁴	~100	~0.5–1.5	5–60	10³–10⁴	1–100

* Calculated as a ratio of plume buoyancy flux at the ridge, $B_r = \rho_o\alpha U_o D_{rbl} \int (T(x) - T_o)\,dx$, where the x axis is along the ridge, D_{rbl} is mean RBL thickness and $T(x)$ is along-axis temperature, and plume source buoyancy flux[22], $B_s = \rho_o\alpha\Delta T U_p\pi(d/2)^2$, where U_p is bead velocity within the plume conduit and d is conduit diameter (1.5–1.8 cm). B_s ranges between 0.003–0.004 g s^{-1}. Reference density, ρ_o, at ambient temperature (20 °C) is 1.4 g cm^{-3}. Important parameters for comparing results on B_r/B_s are highlighted in bold. Comparisons are also made using plume Peclet number, $Pe_p = U_pD/\kappa$, and the ratio Pe_p/Pe. Mantle Pe_p is calculated from Whitehead and Luther's[22] equation for U_p. B_n, Pe_p and Pe_p/Pe, which best represent the vigour of plume convection relative to plate-driven flow, and μ_o/μ_p scale well with expected mantle values. μ_L/μ_o and $\Delta\rho/\rho_o$ reflect differences in laboratory and mantle material properties.
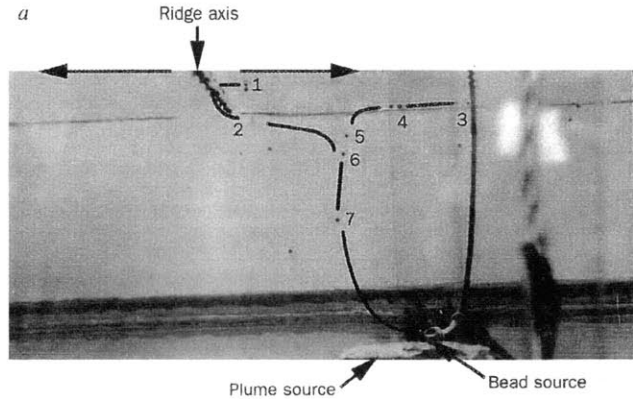
156

FIG. 3 *a*, Photograph of the tank fluid during experiment 2 showing locations of 7 Delrin beads (trajectories sketched in black). Bead no. 1 reached the high-viscosity upper boundary layer then travelled along a sub-horizontal path to the ridge axis similar to the depiction in Fig. 1a. This photograph was taken 65 min after plume initiation, 50 min after the plume–RBL impact, and 15 min after bead no. 1 hit the ridge. The bead is now frozen into the migrating plate. The photograph is taken from a mid-depth fluid level, and the dark sloping line is the ridge axis (line of RTDs) as viewed from below, through the fluid. The bead below and to the left of no. 7 was introduced while setting the bead source and is not part of the experiment. *b*, Fluid temperatures measured by eight RTDs along the ridge axis at different times during experiment 2, showing evolution of a narrow axial anomaly. Temperatures increase with time primarily at RTD 5, peaking at ~3 °C above ambient temperature. Temperatures are still increasing at 95 min, or 45 min beyond bead no. 1's arrival. *c*, Fluid temperatures along the ridge axis at the conclusions of the four experiments. Without the RBL (experiment 1) or if the plume is too hot (experiment 4), the plume fails to reach the ridge and enhance ridge temperatures. Note the broader axial anomaly for the case with a larger (3°) RBL slope (experiment 3).
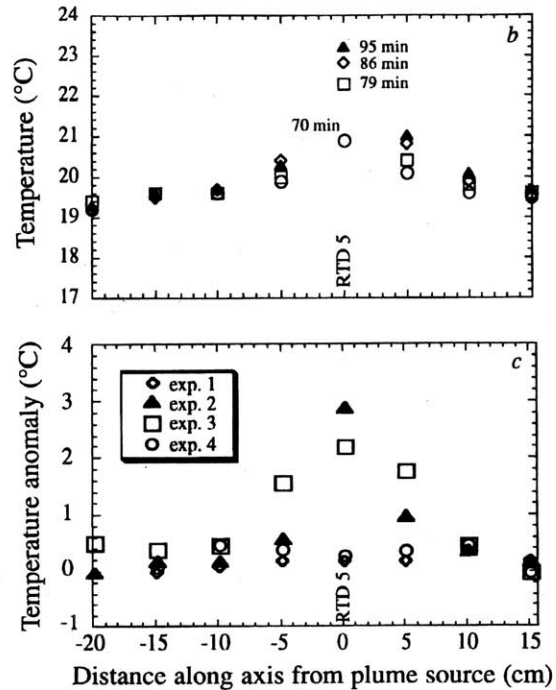
respectively. We characterize the strength of the plume by the dimensionless buoyancy number[8], B_n, defined as

$$B_n = \left(\frac{\Delta\rho g Q}{\mu_o U_o^2}\right) \qquad (2)$$

where g is the acceleration due to gravity, μ_o is reference dynamic viscosity and Q is the volumetric plume flux[20], which is a constant $0.14\,\mathrm{cm}^3\,\mathrm{s}^{-1}$ between experiments. Characterizing plumes in this manner enables us to compare plumes quantitatively between experiments (see Table 1) and provides a measure of how well our laboratory plumes represent Earth examples. Our laboratory B_n are near the upper limit of the expected range for the Earth of 7–59 (ref. 8).

Length and time scales in the laboratory models are related to the mantle through the Peclet number,

$$Pe = U_o D / \kappa \qquad (3)$$

Thermal diffusivity, κ, of the laboratory fluid is $0.001\,\mathrm{cm}^2\,\mathrm{s}^{-1}$ and the corresponding mantle value is $0.01\,\mathrm{cm}^2\,\mathrm{s}^{-1}$. We define the length scale, D, as the thickness of the laboratory fluid (17 cm) corresponding to 600 km of the upper mantle. Thus, our $0.35\,\mathrm{cm}\,\mathrm{min}^{-1}$ Mylar speed yields $Pe = 100$ and scales to a slow mantle full-spreading rate of ~1 cm yr^{-1}. Likewise, our laboratory plume–ridge separation distance of 14 cm scales to a mantle distance of ~500 km.

The four experiments we present here are selected from a total of nine to highlight the relative roles of surface cooling (compare experiment 1 with 2, and 2 with 3) and plume source temperature

(compare experiments 2 and 4) on plume-ridge communication (see Table 1). In experiment 1 (Fig. 2), the fluid surface is not cooled, but rather maintained at room temperature; therefore no sloping RBL is present. As the rising plume reaches the surface, the plume head flattens and widens (10–12 cm wide), but we see that without a sloping RBL the plume is strongly deflected away from the spreading axis such that no plume material reaches the ridge (Fig. 2c).

Experiment 2 is performed with the same plume source temperature but with surface cooling, which, combined with plate spreading, produces a characteristic upper thermal/rheological boundary layer that slopes towards the spreading axis. If we arbitrarily define the RBL as the isosurface along which viscosity is twice that of the ambient fluid ($175_vPa\,s^{-1}$) then the RBL thickness above the plume source is 0.25 cm (that is, 350 Pa s^{-1} at 15.5 °C) after the plate-driven flow has been established. The initial RBL slope in this experiment is then 1°, assuming zero RBL thickness at the ridge axis 14 cm away.

The role of the RBL on plume-ridge interaction is apparent in the paths of neutrally buoyant tracer beads (Fig. 3a). Most beads are deflected by the plate flow, but two (1 and 2 in Fig. 3a) migrate toward the ridge, indicating successful plume-ridge communication. The bead source is positioned on the side of the plume heater, away from the ridge axis. Because of this, and the fact that only a percentage of the plume is channelled to the ridge, a large number of beads (3–7) track the fraction of plume being deflected from the ridge. Long-term sampling of plume material by the ridge is more clearly recorded by the axial temperatures, which increase steadily with time as hotter plume material reaches the ridge (Fig. 3b). This plot shows axial temperatures still increasing at 95 min, which is 45 min (or 55 Myr) beyond the arrival of bead 1 at the ridge. Spatially, the temperature anomaly is centred on RTD 5 with an axial width of roughly 10 cm (350 km). This narrow, confined axial anomaly indicates that rather than spreading radially along the RBL, the off-axis plume is channelled ridgeward through a narrow conduit as predicted from constructional volcanism[2] and geochemical studies[11]. The scaled anomaly width of roughly 350 km is the approximate width of geochemical anomalies along the Mid-Atlantic Ridge (MAR)[11] associated with the Ascension and Tristan hotspots, both of which are ~400 km from the MAR, similar to scaled laboratory plume-ridge offsets of 500 km.

Also consistent with the behaviour of the Tristan system is the substantial cooling of the laboratory plume as it migrates from the source to the ridge. The laboratory plume source temperature is 35–40 °C higher than the ambient temperature. The equivalent mantle plume temperature excess is ~500 °C using a mantle α value of 3×10^{-5}, but at the ridge the temperature anomaly is only ~3 °C, or a mantle equivalent of 45 °C, indicating that substantial conductive cooling of plume material occurs between the source and ridge axis. Most cooling probably occurs along the sub-horizontal plume conduit (path A–B in Fig. 1a) where bead velocities drop to 0.5–1 cm min^{-1} and where the plume is in direct contact with the cold upper boundary layer.

Analogously, the Tristan plume is expected to have cooled by as much as 200 °C along its migration path to the MAR[7].

In experiment 3, the surface is cooled even further to yield an initial RBL slope of ~3° between the plume and ridge. Here the resulting axial temperature anomaly is broader (~20 cm or 700 km) than with the 1° slope (Fig 3c) Assuming that the axial anomaly reflects directly the plume flux to the ridge, we estimate that the ridgeward plume buoyancy flux (see Table 1) is ~10% of the entire source flux, or ~3 times that estimated for experiment 2, where RBL slope was a third as large. These results suggest that the proportion of a plume that feeds a nearby ridge depends directly on the amplitude of the RBL slope, which is consistent with results from two-dimensional numerical experiments[18]. Because the lithosphere probably slopes by 3–10°, even larger proportions of plumes may feed ridges in the mantle.

Finally, experiment 4 is identical to experiment 2, except with a 20% higher plume-ambient-temperature contrast. Although intuitively it might seem that increasing plume buoyancy should increase plume flow along the sloping RBL to the ridge, the absence of any plume signal at the ridge for this stronger plume case (Fig. 3c) indicates that this relationship does not necessarily hold. Instead, the hotter plume erodes a pocket in the RBL (Fig. 1a) which traps the plume head in the translating viscous plate, a result consistent with two-dimensional numerical experiments (C.K., J.-G. Schilling and C.G., manuscript submitted). The trailing conduit is tilted away from the ridge, thereby prohibiting further ridgeward flow. Such behaviour may, in part, explain why only the weakest plumes discussed by Sleep[21] have recognizable signatures at nearby ridges[16] The most robust present-day plume is Hawaii, but it is located >5,000 km from the nearest ridge. The prediction from these experimental results is that lithospheric erosion may have prohibited communication of the Hawaiian plume with the East Pacific Rise throughout its existence, even during 50–70 Myr ago when it was closer to the ridge than it is today.

Our fully three-dimensional variable-viscosity laboratory experiments indicate that the preservation of an upper rheological boundary that thins toward the ridge axis is the primary requirement for communication between an off-axis mantle plume and a nearby spreading centre. The greater the RBL slope, the more effectively it diverts the buoyant low-viscosity plume material to the ridge. But extremely hot plumes may erode the RBL, thus precluding the plume from feeding the ridge. Our laboratory results show that the plume signal at the ridge is narrow, indicating that communication could be through a confined conduit such as has been proposed as a result of previous observations[2,11]. Continuing laboratory experiments are investigating the effects of larger RBL slopes and wider ranges in plume buoyancies and plate velocities on plume-ridge dynamics. It is important to note that in cases where ridges have migrated away from ridge-centred plumes, the dynamics of interaction may be affected by the track of thin lithosphere (e.g. thermal groove[16]) that is left behind. To address this issue, the laboratory apparatus is also being employed in a study of stationary plumes interacting with migrating ridges and plumes beneath ridge-transform offsets. □

1. Vogt, P R Earth planet Sci. Lett 13, 155–160 (1971).
2 Morgan, W. J. J. geophys Res. 83, 5355–5360 (1978)
3. Schilling, J -G Nature 242, 565–571 (1973).
4. Hart, S. R., Schilling, J.-G. & Powell, J L Nature 246, 104–107 (1973)
5. Sun, S -S, Tatsumoto, M & Schilling, J -G Science 190, 143–147 (1975).
6 Poreda, R J., Schilling, J.-G. & Craig, H Earth planet. Sci Lett 119, 319–329 (1993)
7. Ito, G & Lin, J. Geology 23, 657–660 (1995).
8. Feighner, M. A. & Richards, M A Earth planet. Sci. Lett 129, 171–182 (1995).
9 Ribe, N. M., Christensen, U R & Theibing, J Earth planet. Sci Lett (in the press)
10. Schilling, J.-G, Kingsley, R & Devine, J. D J geophys. Res 87, 5593–5610 (1982)
11. Schilling, J -G Nature 314, 62–67 (1985)
12 Schilling, J -G Thompson, G, Kingsley, R & Humphris, S. Nature 313, 187–191 (1985).
13. Hanan, B B, Kingsley, R H & Schilling, J.-G. Nature 322, 137–144 (1986).

14 Hanan, B B & Schilling, J -G. J geophys Res 94, 7432–7448 (1989)
15 Fontignie, D & Schilling, J.-G Chem. Geol 89, 209–241 (1991).
16 Schilling, J -G Nature 352, 397–403 (1991)
17 Kincaid, C & Gable, C W EOS 73, 582 (1992)
18 Kincaid, C, Schilling, J -G. & Gable, C W EOS 74, 673 (1993)
19. Rowley, C, Gable, C & Kincaid, C EOS 73, 582 (1992)
20 Prandtl, L. Essentials of Fluid Dynamics (Hafner, New York, 1952)
21. Sleep, N. J geophys Res 95, 6715–6736 (1990)
22 Whitehead, J. A & Luther, D S J geophys Res 80, 705–717 (1975)

158